1996

Band-structure calculations for point and two-dimensional defects in zinc-blende III-V nitrides

E. A. Pentaleri
San Jose State University

INFORMATION TO USERS

This manuscript has been reproduced from the microfilm master. UMI films the text directly from the original or copy submitted. Thus, some thesis and dissertation copies are in typewriter face, while others may be from any type of computer printer.

The quality of this reproduction is dependent upon the quality of the copy submitted. Broken or indistinct print, colored or poor quality illustrations and photographs, print bleedthrough, substandard margins, and improper alignment can adversely affect reproduction.

In the unlikely event that the author did not send UMI a complete manuscript and there are missing pages, these will be noted. Also, if unauthorized copyright material had to be removed, a note will indicate the deletion.

Oversize materials (e.g., maps, drawings, charts) are reproduced by sectioning the original, beginning at the upper left-hand corner and continuing from left to right in equal sections with small overlaps. Each original is also photographed in one exposure and is included in reduced form at the back of the book.

Photographs included in the original manuscript have been reproduced xerographically in this copy. Higher quality 6" x 9" black and white photographic prints are available for any photographs or illustrations appearing in this copy for an additional charge. Contact UMI directly to order.

UMI

A Bell & Howell Information Company
300 North Zeeb Road, Ann Arbor MI 48106-1346 USA
313/761-4700 800/521-0600

BAND-STRUCTURE CALCULATIONS FOR POINT AND TWO-DIMENSIONAL DEFECTS IN ZINC-BLENDE III-V NITRIDES

A Thesis Presented to

The Faculty of the Physics Department

San Jose State University

In Partial Fulfillment of the Requrements for the Degree

Master of Science

by

E.A. Pentaleri

May 1996

APPROVED FOR THE PHYSICS DEPARTMENT

V. Gubanov

Dr. Vladimir Gubanov

Dr. Carolus Boekema

Dr. Karamjeet Arya

Dr. Joseph Becker

APPROVED FOR THE UNIVERSITY

Serena M. Stanford

ABSTRACT

BAND-STRUCTURE CALCULATIONS FOR ONE- AND TWO-DIMENSIONAL DEFECTS IN ZINC-BLENDE III-V NITRIDES

by E.A. Pentaleri

Linearized Muffin-Tin Orbital (LMTO) calculations were performed to study the electronic structure and bonding of point defects in cubic (zinc-blende) BN (c-BN), AlN (c-AlN), and GaN (c-GaN), and for a highly strained AlN/BN superlattice. Anion and cation vacancies were studied in c-BN and c-GaN, as were various anion and cation substitutional impurities: Be and Mg in c-BN, Mg in c-AlN, and O, Zn and Cd in c-GaN.

Benchmark calculations were performed to verify the accuracy and optimize the efficiency of the calculations. Large outward relaxation was predicted for atoms neighboring vacancies and impurities in c-BN. Small outward relaxation was predicted near Mg impurities in c-AlN. Except for the Zn impurity in c-GaN, donor and acceptor bands tended to be moderately to highly localized near defect sites. Type II alignment was predicted for the relaxed [001] AlN/BN superlattice. AlN layers bore the greatest strain and exhibited the greatest band bending.

BAND-STRUCTURE CALCULATIONS FOR POINT AND TWO-DIMENSIONAL DEFECTS IN ZINC-BLENDE III-V NITRIDES

List of Tables

List of Figures

Chapter II

Chapter III

Chapter IV

Chapter V

Chapter VI

I. INTRODUCTION

A. Motivation for the research

Wide-bandgap compound semiconductors have been studied for more than thirty years. The successes during the past five years in the production of commercial-grade optoelectronic devices,[1-5] however, has stimulated a greatly increasing interest in these materials and their heterostructures. In addition to compact, efficient, short-wavelength lasers and LEDs, other important applications include detectors with sensitivity at ultraviolet wavelengths, electronic devices resistant to damage by ionizing radiation, and devices able to operate at elevated temperatures for a range of military, industrial, and space-borne applications.[6] As is true for electrical and optical materials generally, understanding and developing means of tailoring defects and impurities, and for fabricating heterostructures from these materials will play a central role in realizing the full potential of these systems.

Despite the recent successes and the many useful applications that are anticipated, important characteristics of electronic structure, chemical bonding, and the behavior of defects and impurities cannot be experimentally isolated for many of the wide-bandgap systems of interest. Nor have certain important aspects of many of these systems been studied in systematic detail by means of theoretical computations.

Of the wide-bandgap semiconductors, the III-V nitrides are in many regards among the most intriguing, both on purely physical and on technological grounds. From a physical standpoint, they are the most ionic of the III-V compound semiconductors, they have very short bond lengths, low compressibility, and high thermal conductivity. Beyond their demonstrated uses for high-brightness blue LEDs and their potential applications at even shorter wavelengths, these physical properties may also permit the development of electronic devices able to operate reliably at elevated temperatures (e.g., $\geq 600°$ C). Unlike wide-gap II-VI semiconductors such as ZnSe and ZnS, which tend to degrade over time, the high defect-formation energy of III-V nitrides may permit longer, more stable operation under both "normal" and extreme environmental conditions.[2,6]

The objectives of the research presented here are to investigate the electronic and bonding properties of point and two-dimensional "defects" in the cubic phases of several III-V nitrides: BN, AlN, and GaN. The point defects considered include anion and cation vacancies and substitutional impurities. The two-dimensional "defect" considered here is the highly strained coherent interface that occurs in a thin AlN/BN superlattice.

The high vapor pressure and low solubility of N at the high-temperatures typically required to grow the cubic phase of the III-V nitrides usually result in the formation of non-stoichiometric crystals that have high densities of N vacancies. These vacancies are widely assumed to be responsible for the fact that III-V nitrides typically have strongly *n*-

type characteristic conductivity, and for the corresponding difficulties in achieving *p*-type conductivity by means of conventional doping techniques.[2,6-8] This set of circumstances motivates the investigation of anion vacancies and the investigation of both substitutional impurities and cation vacancies that may be useful either for compensating *n*-type conductivity or for creating materials with *p*-type majority carriers.

Practical electronic and optoelectronic applications of wide-gap materials have been and will probably continue to be largely centered around the fabrication of heterostructure devices. To date, this interest has focused mainly in the development of heterostructures formed from nearly lattice-matched alloys of Al, Ga, and In nitrides. Such alloys are attractive because their near lattice matching to one another is conducive to the fabrication of high-quality structures, and because the range of band gaps spanned by the alloy constituents readily facilitates broad degrees of freedom for tailoring electronic properties. While the fabrication of strained heterostructures certainly involves new challenges, the strain itself introduces new degrees of freedom for tailoring electronic structure. The AlN/BN thin superlattice considered here includes coherent interfaces between two high-bandgap materials, each of which exhibits a band gap in excess of 6 eV in ideal bulk crystals. While the practical realization of such heterostructures is at this point highly speculative, they nevertheless present unique possibilities in terms of operation at short wavelengths, high frequency,[9] and under environmental extremes of both temperature and exposure to ionizing radiation.

B. Research scope

The effort reported here is a systematic study of defects and impurities in zinc-blende III-V nitrides. The electronic structure and bonding characteristics of the defects and impurities were studied by performing band-structure calculations based on the Linear Combination of Muffin-Tin Orbitals model in the Atomic Sphere Approximation (LMTO-ASA).[10] The host lattices considered were the cubic (zinc-blende) phases of boron nitride, aluminum nitride, and gallium nitride (c-BN, c-AlN, and c-GaN, respectively). Table I lists the defects and impurities that were considered. Point defects (anion or cation vacancies) and substitutional impurities in the host lattice were represented by a 64-atom supercell centered on the defect or impurity site.

Table I. Defects and impurities considered within the scope of the present research.

	c-BN	c-AlN	c-GaN
Anion Vacancy	●		●
Anion Substitutions:			
O			●
Cation Vacancy	●		●
Cation Substitutions:			
Be	●		
Mg	●	●	
Zn			●
Cd			●

Calculations for the ideal cubic systems were performed with a simple two-atom basis that was translated through all space by the vectors describing a face-centered cubic (fcc) lattice. As will be described in the next chapter, the model used for the c-GaN was considerably more complicated than that used for the c-BN calculations, while an intermediate level of complexity was required for the treatment of c-AlN. In particular, calculations for c-GaN required the use of two empty

muffin-tin spheres to improve the representation of the self-consistent potential and wave functions in interstitial regions. They also required the treatment of semi-core $3d$ electrons as valence states rather than as frozen core states. Although each supercell used for the c-GaN defect and impurity calculations included 64 atoms, these supercells included a total of 128 sites, and many more valence electrons than were represented in either the c-BN or the c-AlN models. For the c-BN and c-AlN host lattices, the radial relaxation of atoms nearest the defect or impurity was determined by minimizing total energy of the supercell versus the radial coordinate of atoms in the first coordinational sphere. This relaxation was possible because benchmark calculations showed that accurate results could be obtained for c-BN without the use of empty spheres. While such calculations showed good accuracy only in the valence bands of c-AlN, these occupied states participate most directly in bonding and electronic structure in acceptor-type impurities, making limited use of this model possible. The complexity of the GaN model did not permit such relaxation however.

The final element of the research reported here is a series of calculations that were performed with a supercell representing a thin, highly strained, coherent superlattice. This superlattice was formed from alternating layers of c-BN and c-AlN stacked along the [001] axis. Relaxation of the AlN/BN superlattice was again performed by minimizing total energy, although in this instance the minimization was performed with respect to three lattice parameters: the lattice constant "a" describing atomic positions in planes

parallel to the interface, and the *c*-axis lattice parameters representing atomic positions normal to the interface in both the c-BN and the c-AlN layers.

In each series of calculations, results for the ideal cubic nitride crystals provide a basis for judging the accuracy and validity of the computational models, and for identifying electronic-structure perturbations introduced by vacancies, substitutional impurities, and strain. Defect and impurity bonding characteristics are revealed by taking appropriate projections of the density of states (DOS) over the orbital and atomic basis sets, and by comparing these with corresponding projections for the ideal crystals. The qualitative features of impurity bonding are further revealed by charge-density maps. In analyzing the superlattice calculations, the DOS projections over different atomic layers reveal both band offsets at the interface, as well as the differences in electronic structure between interface and bulk-like atoms. Charge-density maps clearly show the effect that strain has upon the orbital alignment and bonding in atomic layers on both sides of the interface.

The discussion is organized as follows. The LMTO-ASA model is described in Chapter II, as is a more detailed discussion of its implementation for the defect, impurity, and interface calculations that were performed here. Each of the subsequent three chapters focuses on defects and impurities in a different host lattice. Chapter III deals with c-BN, Chapter IV with c-AlN, and Chapter V presents the results of c-GaN calculations. Each of these chapters presents a detailed discussion of the calculation results, and the

implications of these results for tailoring electronic structure and for applications. The AlN/BN superlattice calculations are discussed in Chapter VI, which includes a detailed discussion of the lattice relaxation, a comparison of each strained layer's electronic structure with its corresponding bulk electronic structure, and an analysis of the band offsets predicted by this model. In Chapter VII, the results are summarized and general conclusions are presented.

Before proceeding to the detailed technical discussion, it is worthwhile to note that the results presented here represent an intermediate stage of a "work in progress." At this writing, additional calculations are being performed for C, O, Si, Be, and Zn substitutions in c-AlN. Preliminary calculations have also been completed for AlN/BN with heavy delta doping of Mg on each side of the anion interface layer. Most of the results of the c-BN calculations have been reported previously,[11,12] while the complete set of results for point defects in c-AlN and c-GaN will be presented very soon.[13]

II. COMPUTATIONAL MODELS AND TECHNIQUES

A. The LMTO-ASA model

All of the calculations to be discussed were performed with the Linearized Muffin-Tin Orbital (LMTO) technique,[10] as implemented in the computer code written by van Schilfgaarde, *et al.*[14] The computations were performed in the tight-binding (TB) and atomic-sphere approximations (ASA), and include the Hedin-Lundqvist[15] corrections for exchange and correlation based on the local-density approximation (LDA).

The LMTO technique is one of a class of so-called self-consistent techniques for describing the band structure of electrons in a periodic potential. In these techniques, both the wavefunction and potential are described in terms of an appropriate set of basis functions. The appropriateness of a particular basis set is determined largely by the compactness with which it is able to represent the physical system. Thus while plane waves constitute an appropriate basis for describing weakly bound free-electron-like conduction electrons of metals such as Na, atomic orbitals are appropriate for systems in which atomic orbital configurations are weakly to moderately perturbed from those of isolated atoms.

In the self-consistent formalism, a trial wavefunction is constructed from the chosen basis to represent the configuration of electrons for the specified crystal structure. The description of the wavefunctions and potentials are iteratively perturbed until they

become mutually self-consistent to within a specified set of convergence criteria for the change in total energy and the redistribution of charges.

Although many techniques have been advanced and successfully implemented for solving band-structure problems, they can generally be differentiated from one another in terms of (a) the choice of basis functions used to formulate the Bloch-expansion representation of the wavefunction and the periodic potential, (b) the form (integral or differential) of the Schrödinger wave equation (SWE) used in the solutions, and (c) the analytical and numerical techniques used to efficiently solve the resulting secular determinants. The LMTO technique derives most directly from the Green-function integral solution of Korringa, Kohn, and Rostoker (KKR),[16] in which the wavefunctions and potentials are expanded over a basis of so-called muffin-tin orbitals. The conventional muffin-tin-orbital basis used in the KKR technique consists of spherical harmonics and solutions to the radial SWE at points contained within non-overlapping spheres whose maximum radius inscribes them within the Wigner-Seitz polyhedron. Outside the "muffin-tin radius," the potential is assumed constant. The spherical symmetry of the muffin-tin orbitals simplifies the representation of the potential, the wavefunctions, and the boundary conditions specified at the surface of the muffin-tin spheres. Unfortunately, the dependence of the muffin-tin orbital basis upon the energy eigenvalues causes the secular equations to be non-linear in energy.

The LMTO technique overcomes the latter difficulty by constructing the muffin-tin orbital basis from linear combinations of atomic-orbital basis functions $\phi_l(E_\nu, r)$ and their energy derivatives $\dot{\phi}_l(E_\nu, r)$, which are evaluated at the fixed, but arbitrary energy E_ν:

$$\Phi_{lm} = i^l Y_{lm}(\hat{r})\left[\phi(E_\nu, r) + \omega(D)\dot{\phi}(E_\nu, r)\right]$$

where D is logarithmic derivative

$$D_\nu \equiv S\frac{\phi_\nu'(S)}{\phi_\nu(S)},$$

which is evaluated at the muffin-tin radius S.

In the interstitial region, the energy-independent muffin-tin orbitals have tails proportional to $r^{-l-1}i^l Y_{lm}(\hat{r})$. Individually, these tails are solutions to the Laplace equation, as is the interstitial potential formed by the superposition of these tails. The orbital basis is usually truncated at orbital angular momentum quantum numbers of l=2 or 3. The periodic potential of a crystal system is represented in this basis by specifying the crystal structure and constructing a trial wavefunction from an appropriate linear combination of muffin-tin orbitals on the defined crystal structure.

The basis that results from this construction is everywhere continuous and differentiable, and facilitates the formulation of the self-consistent problem in terms of the differential form of the Schrödinger equation rather than the equivalent integral formulation used in

the KKR technique. The main consequence of using the energy-independent muffin-tin-orbital basis however is the linearization of the secular equations in energy.

Given that the orbital basis is constructed from solutions to the radial SWE at the arbitrary energy E_ν, the solutions obtained from the LMTO technique are in general not exact. In elucidating the LMTO formalism however, Andersen showed that the errors introduced by this choice of basis are of fourth order in the difference $E_j^k - E_\nu$ with respect to the predicted energies, while errors in the wave functions can be reduced in practice to third-order in this difference.[10]

The atomic-sphere approximation (ASA) referred to earlier is introduced as a simplified technique for evaluating the integrals in the interstitial regions between the muffin-tin spheres. Here instead of performing the exact numerical integration over the complicated volumes bounded between the muffin-tin spheres and the Wigner-Seitz atomic polyhedra, the integrations are performed over the much simpler volumes bounded between muffin-tin spheres and Wigner-Seitz atomic spheres. The latter are constructed to enclose a volume equivalent to that of the corresponding Wigner-Seitz unit cells. This is a computationally expedient approximation to the exact band-structure solutions for the periodic potential, with the approximation introducing small overlap volumes between adjacent atomic spheres. The existence of these overlapping regions is corrected by appropriate subtractions from the Hamiltonian and overlap matrices.

In the LMTO-ASA calculations performed here, electrons occupying closed atomic shells are treated as "frozen core states." That is to say that the configurations of these electrons are assumed to be identical to the corresponding core-state configurations of isolated atoms, and are not perturbed in the course of the self-consistent iterations. The description of valence electrons however is subject to perturbation at each iteration of the atomic potential. While the use of the muffin-tin orbital basis provides a compact representation of the periodic potential and electronic wavefunctions, further computational efficiency is provided by the LMTO technique due to the use of an energy-independent basis and the atomic-sphere approximation. These approximations do introduce computational errors, but these errors are typically small and are justified by the superior efficiency of the technique for completing band-structure calculations.

B. Construction of the zinc-blende supercells

For each calculation it is necessary to define the real-space configuration of atoms to be modeled. For ideal-crystal calculations, this description is particularly straightforward, involving only the description of the two-atom basis and the set of symmetry operators that maps this basis into the zinc-blende lattice throughout all space. Figure 1 is a schematic representation of a portion of the zinc-blende lattice that shows the essential symmetries of the structure. In particular, this figure shows the tetrahedral coordination of bonding that exists among nearest-neighbor atoms. At each atomic site, an atom of one type is bound to four nearest neighbors, each of which is of the other type and is located at the vertex of a tetrahedron. In the cubic zinc-blende structure, tetrahedra centered on adjacent atoms are rotated relative to one another by 60° about the axis that

connects their central atoms. In the closely related wurtzite structure by contrast, the adjacent tetrahedral groups are aligned with one another. This alignment gives wurtzite symmetry that is hexagonal rather than cubic.

To predict the electronic structure associated with defects and impurities using the LMTO technique, it is necessary to construct atomic "supercells." These supercells describe the defect or impurity site within an otherwise ideal lattice configuration. This supercell structure is effectively translated throughout all space in the band-structure calculations, with the model therefore representing a uniformly doped infinite crystal. In constructing the defect or impurity supercell, the extent of the ideal lattice structure is generally chosen in a manner such that adjacent defect or impurity structures will be non-interacting.

In the defect and impurity calculations that were performed here, cation substitutional impurities and vacancies were represented by constructing 64-atom supercells centered on a cation site. In each case, the central cation was either removed or replaced, and the calculation permitted to proceed to self-consistency. Anion vacancies and substitutional impurities were similarly represented, but

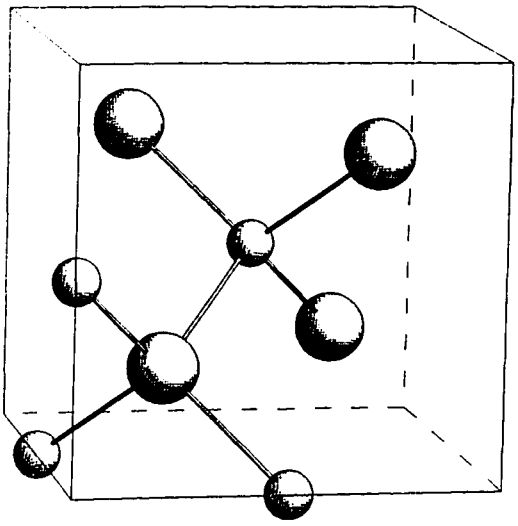

Figure 1. Schematic representation of a portion of the zinc-blende lattice showing the tetrahedral coordination of nearest neighbors and the relative orientation of tetrahedral groups centered or adjacent atomic sites.

with the 64-atom supercell constructed around an anion site. The stoichiometry of the crystals represented by this model was therefore as follows: (a) $X_{0.984}N_{1.000}$ for cation vacancies, (b) $X_{1.000}N_{0.984}$ for anion vacancies, (c) $X_{0.984}N_{1.000}$:$Y_{0.016}$ for cation substitutions, and (d) $X_{1.000}N_{0.984}$:$Y_{0.016}$ for anion substitutions, where X and Y represent cations and impurity atoms, respectively.

The 64-atom supercells can be decomposed into a series of concentric atomic shells surrounding the central lattice site. To facilitate the discussion that follows, the central atom in a cation-centered supercell is denoted as X_0, where X is to be replaced by the appropriate elemental symbol. The adjacent shell of four anions is denoted by N_1, and referred to as the first N shell. The next-outward atomic shell is denoted X_1, and so on to the fifth atomic shell. The subscripts are interchanged for the cation-centered supercells. For each type of supercell, the most distant atomic shell consists of the same type of atom as would be found at the central site in an ideal crystal.

The final set of calculations was performed for a highly strained superlattice formed by thin layers of coherently matched c-AlN and c-BN. In these calculations, the interface between layers is treated as a two-dimensional defect, and is isolated from adjacent interfaces by seven atomic planes. Unlike the impurity and vacancy calculations however, the atomic layers intervening between adjacent interfaces are not in the ideal bulk configuration, but rather are subject to biaxial strain. The structure of the supercells used to describe the AlN/BN superlattice is described in detail in Chapter VI.

C. Empty spheres

The zinc-blende structure is an "open" structure. The nearest neighbors to an atom located at the origin are located at the sites (1/4 1/4 1/4), (-1/4 -1/4 1/4), (-1/4 1/4 -1/4), and (1/4 -1/4 -1/4), while interstitial voids are located at the conjugate positions (-1/4 -1/4 -1/4), (1/4 1/4 -1/4), (1/4 -1/4 1/4), and (-1/4 1/4 1/4). To improve the description of the potential and wavefunctions in the interstitial voids of such open structures, "empty spheres" are frequently introduced to the real-space definition of the crystal structure.[17-20] Unlike the atomic muffin-tin spheres described previously, these empty spheres are assigned no core charges, but do provide a valence-like muffin-tin orbital basis with which to more accurately describe the wavefunction and potential in these relatively large interstitial void regions.

While the use of empty spheres generally improves the accuracy of calculations for open structures such as zinc-blende, they not only complicate the supercell representation of the crystal structure but in adding new basis functions cause a superlinear increase in the number of calculations that must be performed to achieve self consistency. It is therefore desirable to avoid the use of empty spheres to the extent that an adequate description of electronic dispersion can be obtained without them. To determine whether empty spheres are required, it is necessary to perform benchmark calculations for each material system both with and without empty spheres, and preferably using independent full-potential techniques.

As will be discussed in the next three chapters, such benchmark calculations showed the no-empty-spheres LMTO supercell to yield completely satisfactory results for c-BN, while a satisfactory description of c-AlN dispersion was obtained only for levels in the valence band. The poorer performance in the case of the c-AlN calculations is likely due mainly to the much higher ionicity and larger spacing of atoms in c-AlN, as compared to c-BN, each of which causes the interatomic potentials and wavefunctions to assume a more complicated form. Likewise, the ionicity of c-GaN is nearly as great as that of c-AlN, while the atomic separations are even greater. The large number of orbital electrons present in the Ga-atom valence configuration also complicates the representation of the potential and wavefunctions in the interstitial void regions. For the c-GaN calculations discussed in Chapter V, there was therefore never any question of the need to use empty spheres in the formulation of the vacancy and impurity supercells.

D. Computational platforms

The bulk of the calculations were performed on a Cray J90, though a few of the c-BN simulations were performed on the Cray C90 at the San Diego Supercomputing Center. The J90 was configured with 500 Mb of memory and four CPUs. Individual calculations were performed on a single CPU. A benchmark calculation was performed for the N-vacancy c-AlN supercell, completing its first iteration in 309 s of CPU time, vs. 92 s on the C90. The test case achieved an instruction rate of 83.5 MFLOPs, vs. the 200 MFLOP theoretical maximum claimed by the manufacturer.

III. DEFECTS AND IMPURITIES IN ZINC-BLENDE BORON NITRIDE

A. Introduction

Boron nitride occurs in four crystalline phases: hexagonal (referred to also as graphitic or h-BN), rhombohedral (r-BN), wurtzite (w-BN, or α-BN), and zinc-blende (cubic, c-BN, or β-BN). Each has rather remarkable mechanical, electronic, and optical properties, which are closely related in their origin. The properties of boron nitride are similar to those of corresponding carbon phases, with the mechanical properties of h-BN being analogous to those of graphite for example, and c-BN exhibiting strong similarities to the mechanical and electronic properties of diamond. Indeed, recent successes in the growth of diamond films have been partially responsible for increasing interests in the development of c-BN.[6] Like diamond, whose bond length is1.54 Å, c-BN has very short 1.56-Å bonds between atoms.[21] Likewise, each of these materials exhibits a very large, indirect band gap: 5.45 eV for diamond, and ~6.4 eV for c-BN.

In contrast to several other wide-bandgap semiconductors, including diamond, AlN, and GaN, both *p*- and *n*-type conductivity can be readily obtained by selective doping of c-BN. As is true for all of the material systems considered in the present study, nitrogen vacancies are quite common and play an important role in determining the electronic properties actually observed in samples, regardless of the growth techniques used.

Zinc-blende boron nitride is metastable, and can be formed only within rather narrow but extreme ranges of thermodynamic conditions. Typical techniques for growing c-BN thin films include various ion-assisted physical vapor deposition (PVD) techniques, and precipitation from a molten solvent under high pressure. In the latter, temperatures and pressures in the range of 1700 °C and 5.5 kPa, respectively, are required to support the growth of good-quality c-BN films.[6]

B. Ideal c-BN

To judge the influence of defects and impurities on the electronic structure of c-BN, it is necessary first to examine the electronic structure of the ideal crystal. Self-consistent calculaions were performed (Ref. 11) for ideal c-BN by using a simple two-atom basis that corresponds to the unit cell of the zinc-blende lattice. In Figure 1 is shown the band structure of c-BN, as calculated by the LMTO-ASA technique in the tight-

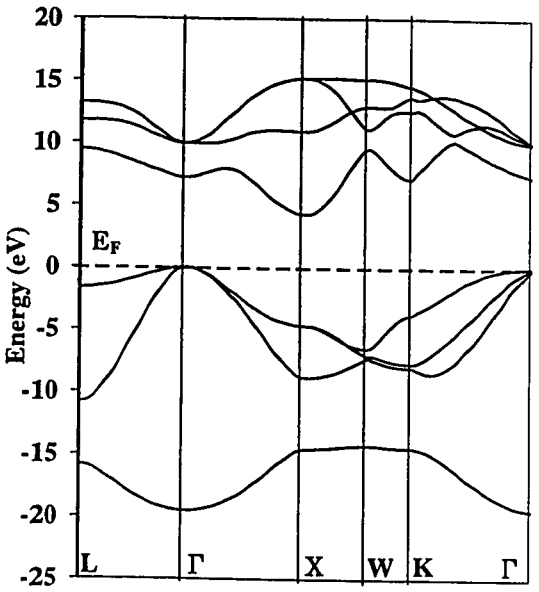

Figure 1. Band structure of c-BN, as predicted by LMTO-ASA-TB calculations without empty spheres. 534 non-equivalent *k*-space points were used in the integrations.

binding approximation, and without the use of empty spheres. Integrations were performed on a fine mesh of 534 non-equivalent *k*-space points in the irreducible Brillouin zone (IBZ) to obtain these dispersion results.

As was noted in Chapter II, both the qualitative and the quantitative features of these dispersion curves are in excellent agreement with results obtained by more rigorous and more computationally demanding full-potential techniques. As is typical for LDA calculations, these dispersion curves accurately represent the essential features of electronic structure that have been ascertained experimentally, with the exception that the energy gap predicted between occupied and unoccupied levels is substantially underestimated. While the band structure shown in Figure 1 suggests a bandgap value of about 4.4 eV, experimental values are typically quoted in the range of 6.0 to 6.4 eV. (The discrepancies among the reported experimental values are most likely attributable mainly to variation in the quality of samples used for the measurements.)

Table I. Comparison of gap and band widths for ideal c-BN, from experiment and from independent calculations. W_L, W_U, and W_T denote the widths of the lower valence band, the upper valence band, and the total valence band width, respectively.

Gap Widths	FP-LAPW[a]	FP-LMTO[a]	LMTO-ASA[a]	Other Works
Γ_v - Γ_c	7.2	8.6	8.2	8.9[b] 8.8[c] 8.6[d]
Γ_v - L_c	9.4	10.3	10.4	10.3[b]
Γ_v - X_c	4.3	4.4	4.3	4.4[b] 4.4[c] 4.2[d]
Γ_v - K_c	7.1	6.9	7.3	
W_v - W_C	16.1	16.1	16.0	
W_L	5.2	6.0	6.1	5.9[c] 5.2[e]
W_U	10.8	10.5	10.8	10.7[c] 13.5[e]
W_T	19.5	20.0	20.1	20.1[c] 22.0[f]

[a] Ref. 11
[b] LMTO-ASA, Ref. 17
[c] FP-LAPW, Ref. 22
[d] Pseudopotential, Ref. 23
[e] X-ray experiment, Ref. 24
[f] XPS experiment, Ref. 25

Table I provides a comparison at high-symmetry points in the IBZ between the band-structure predictions obtained by computationally efficient LMTO-ASA calculations, and the results of independent experiments and computations. The good correspondence between the results produced by each of the computational techniques is clear. Excepting the predicted bandgap value noted above, reasonable agreement is also evident between computed results and available experimental results. The quantitative prediction of the band gap itself is not as interesting for the present investigation, however, as are the features of electronic structure introduced by various defects and impurities.

Figure 2 shows the total density of states (DOS) for ideal c-BN, and for projections of the DOS taken over each atom, and over the *s*, *p*, and *d* orbitals of each atom. The projections show that the lower valence band (VB) is formed mainly by 2*s* states of N, with smaller contributions arising also from 2*p* and 2*s* states of B. The upper valence band is formed mostly from 2*p* states of N, but has smaller, yet significant contributions from B 2*s* and 2*p* states, which contribute in approximately equal measure. The top of the upper valence band, which plays the dominant role in bonding, is dominated by 2*p* states of N and B, though close examination reveals that B 3*d* states represent a significant fraction of the total DOS states at the VB edge itself. The states at the conduction-band (CB) edge are mainly associated with 2*s* and 2*p* states of N and B, which contribute in approximately equal proportion within the first several eV above the CB edge. In the ideal c-BN DOS, the Fermi energy coincides with the VB edge, causing

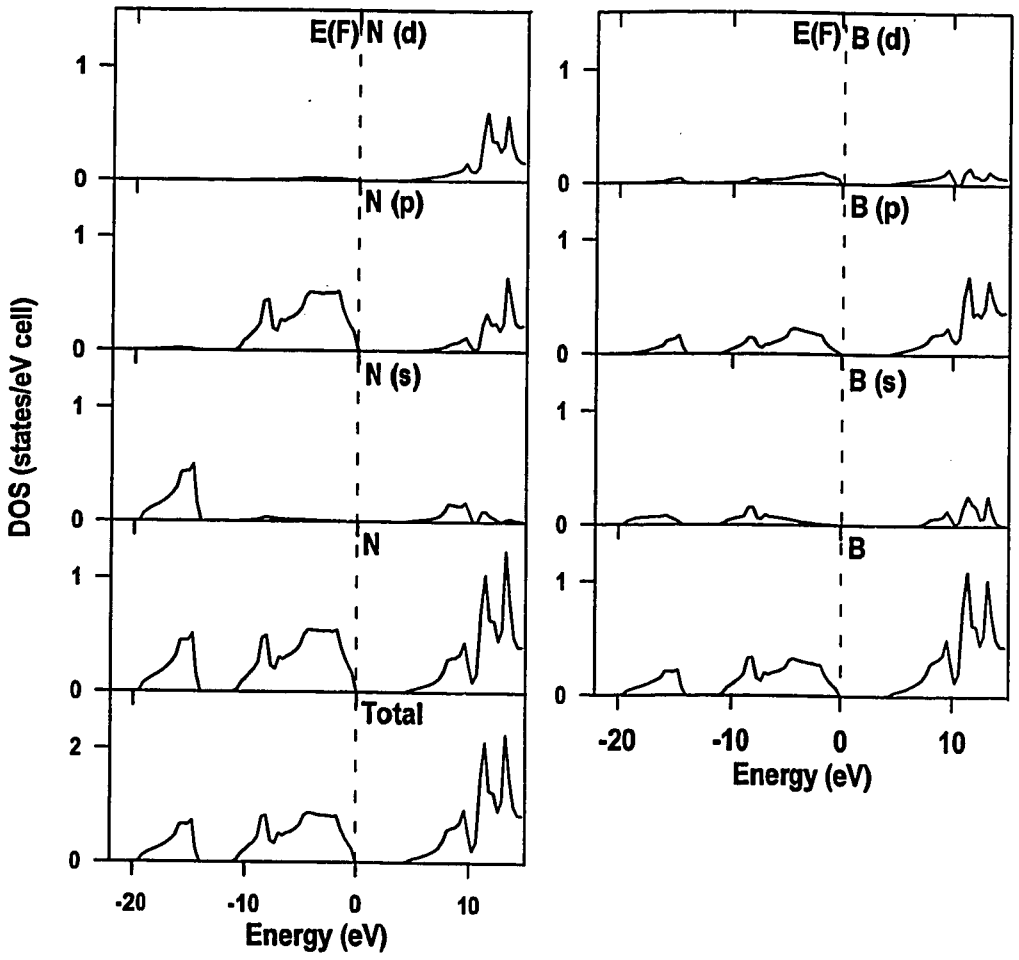

Figure 2. Total and partial DOS for ideal c-BN. Results were produced from LMTO-ASA calculations with integrations performed over 534 non-equivalent *k*-space points in the IBZ.

the pure, ideal crystal to be an effective electrical insulator for many applications. Figure 3 illustrates the highly ionic bonding between B and N atoms in ideal c-BN, with the net transfer of charge being from the B atoms and to the N atoms. This figure illustrates the charge density in the (110) plane, which includes chains of B and N atoms, and the bonding region between atoms.

The analysis presented in the next two sections examines changes introduced to this structure by different types of vacancies and substitutional impurities. Of particular interest for electronic and optical applications are new features that appear in or near the gap, since these may be useful in tailoring c-BN for specific types of applications. Conversely, by decomposing the atomic and orbital structure associated with vacancies and impurities, it will be possible to suggest physical bases for certain experimentally observed changes in the electronic behavior that have been attributed to vacancies and impurities.

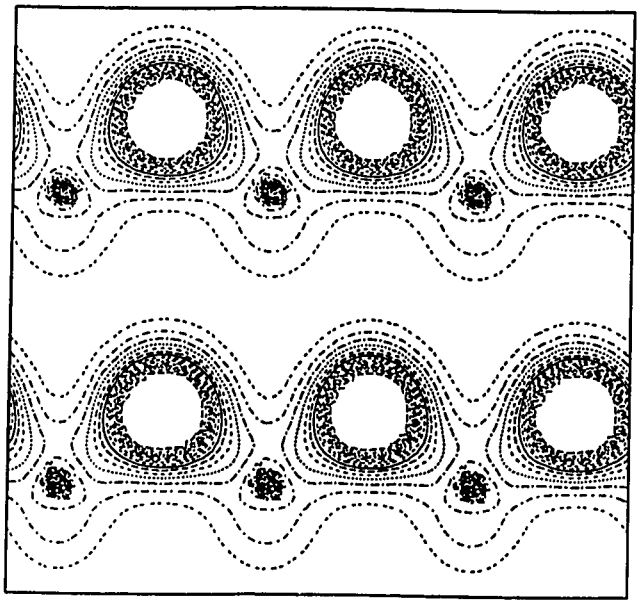

Figure 3. Charge-density distribution in the (110) plane of c-BN, showing chains of B and N atoms. The highly ionic nature of the bonding in these chains is clearly evident in these figures, which show a large accumulation of charge on N atoms.

C. Vacancies in c-BN

Anion and cation vacancies in c-BN were represented by supercells having 64 atomic sites, but with the central anion or cation replaced by a so-called "empty sphere." The potential and wavefunctions within the central empty sphere are constructed as linear combinations of the energy-independent atom-like orbital basis within the defined muffin-tin radius. In this sense, the empty sphere is analogous to an atom with no intrinsic charges of its own. The "valence" electrons for this charge-free "atom" are combinations of 1*s*-, 1*p*-, and 1*d*-type orbital basis functions, which are used to describe the electron wavefunctions and the potential in the vacancy region.

A series of calculations was performed to determine the equilibrium radial relaxation of the nearest atomic neighbors to boron and nitrogen vacancies in c-BN. This relaxation was calculated by minimizing supercell total energy as a function of the coordinate parameters of nearest neighbors. (See caption to Figure 4.) The B vacancy was expected to introduce acceptor-type features near the VB edge, and hence to interact with *p*-type states of N. The empty spheres used in these calculations therefore included both *s*- and *p*-type orbital basis functions. By contrast, N vacancies were expected to have their main influence near the CB edge, which is typically populated mainly by *s*-type states. The N-vacancy empty sphere therefore included only *s*-type orbital basis functions.

Figure 4 illustrates the variation of supercell total energy as a function of the nearest-neighbor radial coordinates. Large outward relaxation from the vacancy site is predicted in each case. For B vacancies, the neighboring shell of N atoms relaxes from 1.57 Å to 1.96 Å. B atoms nearest a N vacancy relax even further to a radius of 2.09 Å. Such large relaxation is not unexpected, given the strong, highly ionic bonds that exist in ideal c-BN.

It is apparent from the relaxation curves that the atoms near the B vacancy are held more rigidly in their equilibrium positions than are those near the N vacancy, at least in the radial dimension that has been explored in this series of calculations. This difference can be partly understood in terms of the number of bonds left "dangling" in each case. There are three fewer valence electrons near the center of the B-vacancy supercell than in the corresponding ideal c-BN structure, while there are five fewer valence electrons near the

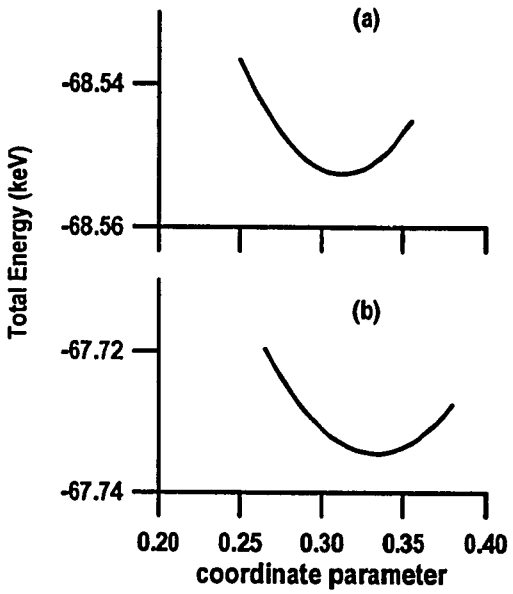

Figure 4. Total energy of 64-atom c-BN supercells with (a) central boron vacancy, and (b) central nitrogen vacancy. Energy is plotted as a function of the coordinate parameter. The coordinate parameter multiplies the lattice parameter to determine the magnitude of nearest-neighbor Cartesian coordinates. In ideal c-BN (a=3.615 Å), the nearest-neighbor coordinate parameter is 0.25, and the nominal separation of neighboring atoms is $\sqrt{3} \times 0.25a = 1.565$ Å.

center of the N-vacancy supercell. The tighter bonding of N atoms surrounding the B vacancy reflects the smaller number of dangling bonds (larger number of remaining bonds) in this case.

Figure 5 illustrates total and partial densities of states for the B-vacancy c-BN supercell. In comparing Figure 5 with Figure 2, the most remarkable feature introduced by the B

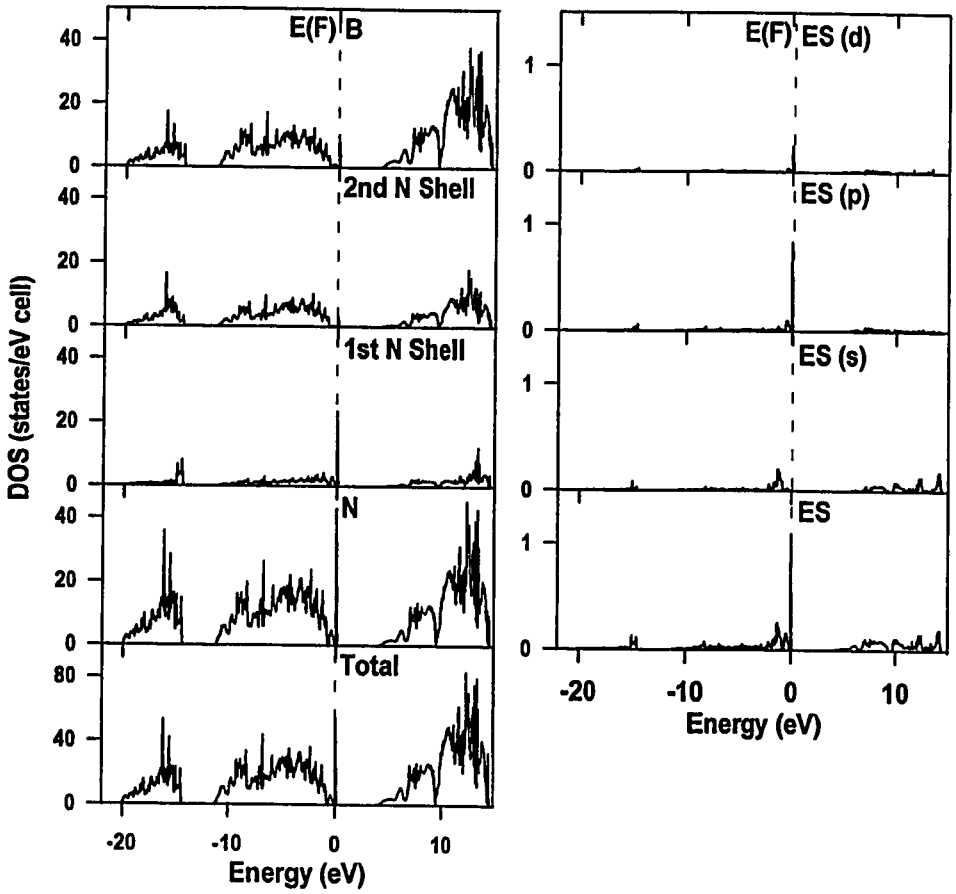

Figure 5. Total and partial DOS of c-BN supercell with B vacancy. The main perturbations to the electronic structure occur near the valence and conduction band edges. Projections over different atomic coordinational spheres shows the narrow resonance near the VB edge to be associated with the N atoms nearest the B vacancy site. Electronic states associated with the vacancy itself are labeled by the letters ES. They contribute only a small amount to the total DOS in the resonance, but have a *p*-like character, as expected.

vacancy is the narrow, intense peak located just above the VB edge. From the shell-projected densities of states shown in the figure, it is clear that the largest contribution to this peak is from the shell of N atoms nearest the vacancy, though there are less significant contributions from B and from more distant N shells. The partial densities of states labeled ES, ES(s), ES(p), and ES(d) are states associated with the vacancy ("empty sphere") itself. Although the vacancy makes only a small direct contribution to the B-vacancy band, the DOS projections show that the empty-sphere states do, in fact, have a *p*-like character. As in the ideal c-BN crystal, the CB edge consists mainly of *s*- and *p*-type states of B and N.

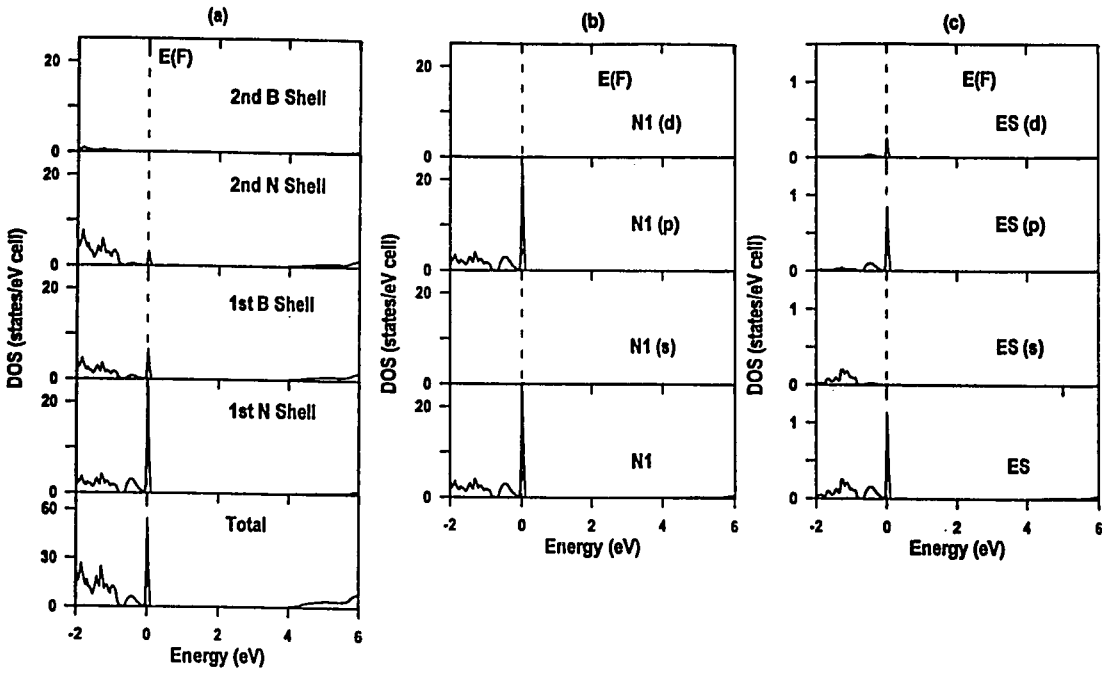

Figure 6. Total and shell-projected DOS in the energy region surrounding the band gap for the c-BN supercell with a central B vacancy. The localization of the vacancy state is shown in (a), while (b) demonstrates that the states are dominated mainly by *p*-type electrons. Electrons associated with the vacancy itself also have a *p*-type character, as shown in (c).

The detailed structure of the band-edge states is shown more clearly in Figure 6. Figure 6a shows very distinctly that both the sharp primary peak straddling the Fermi energy (E_F) as well as the broader secondary peak are quite localized to the vicinity of the vacancy. In addition, they show the vacancy band to be split off from the top of the VB edge, though with only a very small separation of ~0.1 eV at absolute zero temperature. Figures 6b and 6c show the *p*-type character of electrons associated with the vacancy and with the N_I shell.

The results of the calculations permit a convenient, though not a strictly rigorous, analysis of the redistribution of charges among each of the atomic shells in the model. Although the atomic shells are highly overlapping, and although "real" valence electrons cannot be assigned uniquely to one or another group of atoms, this semi-quantitative decomposition of charges is nevertheless useful for understanding the behavior of the system. In the case of the ideal c-BN crystal, there is a net transfer of charges from the B sublattice to the N sublattice, relative to the charges that would be exist on isolated ground-state atoms. This charge transfer amounts to an average of ~0.12 electrons per atom. In the B vacancy supercell, the charge distribution is significantly perturbed, with ~0.5 electrons being transferred mainly from the N_I shell, and leaving these N atoms in a nearly neutral charge configuration. As may be expected, this charge transfer involves mainly the most lightly bound N 2*p* electrons, and creates the *p*-type acceptor levels shown in the DOS projections above. The electrons drawn from the N atoms into the vacancy site assume a

p-type symmetry, in this sense mirroring the normal orbital composition of the cation site near the VB edge.

Figure 7, shows both the total and the band-edge charge distributions for the radially relaxed B-vacancy configuration. Figure 7a shows both the localization of the vacancy-band states to the N_1 shell, as well as the *p*-type character of the interaction between the N_1 shell and the vacancy. The large outward relaxation and the overall distortion of the N_1 atomic configuration is most evident in Figure 7b.

The DOS at E_F is 47.6 states/eV in the 64-atom unit cell. Because the DOS varies rapidly in the vicinity of this resonance, this result is extremely sensitive to the accuracy with which the Fermi energy is calculated. Likewise, the exact width of the vacancy band and the gap between this band and the valence band are susceptible to the choice of calculational parameters, such as the number and choice of points over which integrations in the IBZ are performed. If the resonance is indeed split off from the VB edge, it may be possible for electrons to be thermally ionized from the valence band into the partially occupied vacancy band. With a total width of ~0.7 eV, the vacancy band could act as an effective acceptor-type impurity, permitting *p*-type conductivity in c-BN, and effectively reducing the width of the band gap. Similar behavior could be expected even with little or no separation between the vacancy band and the VB edge since the vacancy band would in either case provide a "reservoir" of unoccupied acceptor-like states. To take advantage

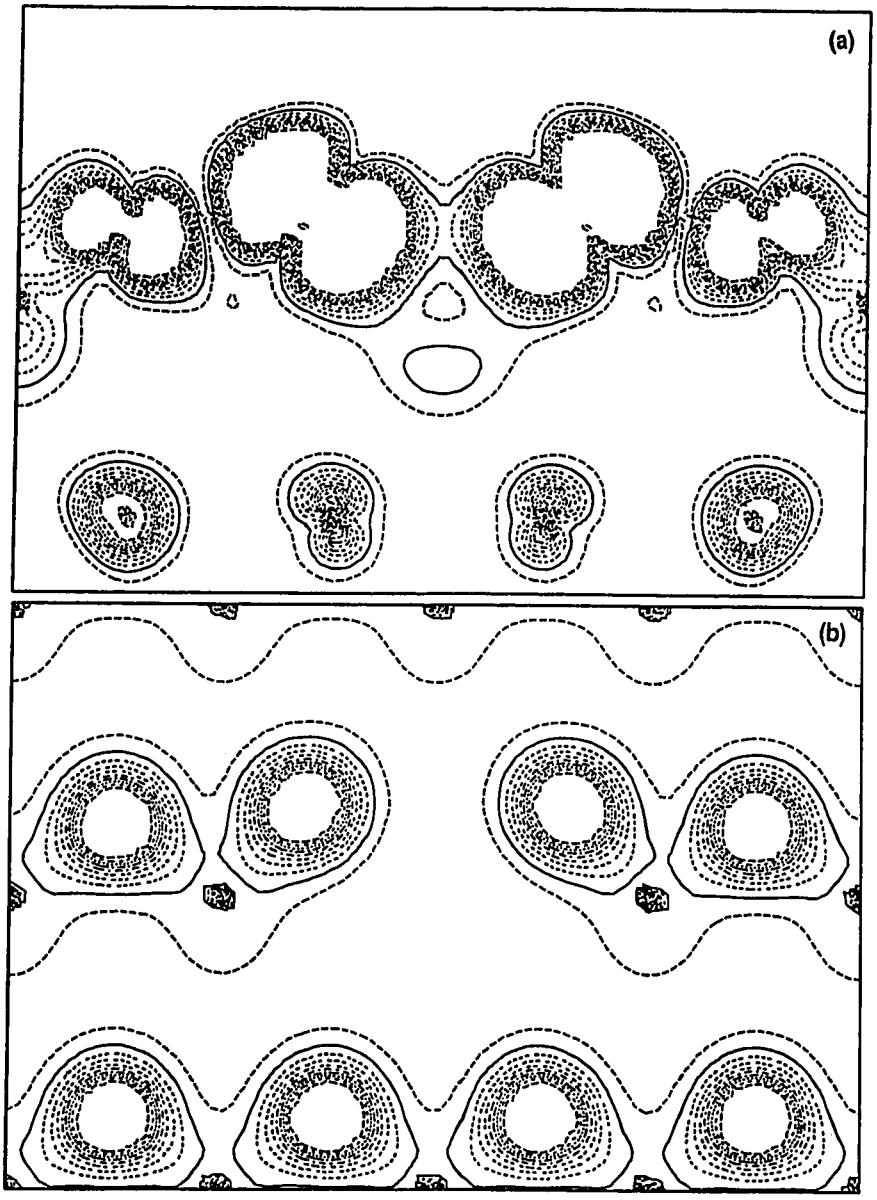

Figure 7. (a) Distribution of charges within the B-vacancy band. (b) Total charge-density distribution in the vicinity of the B vacancy.

of the *p*-type carriers associated with B vacancies, it will be essential to control the density of N vacancies first, since these will typically be responsible for the majority *n*-type carriers.

Figure 8 and Figure 9 illustrate total and partial densities of states for the N-vacancy c-BN supercell. Here the principal effect of the vacancy is quite different from that of the B vacancy. A low band of donor states is introduced into the band gap of the ideal crystal and is merged with the CB edge, while the Fermi level is simultaneously shifted to the position of the original CB edge in the ideal crystal. The low, gradually sloping shape of the vacancy band suggests that the *n*-type carriers associated with N vacancies should have a relatively high characteristic mobility, in the absence of other types of trapping centers.

The two valence bands are virtually unperturbed by the N vacancy, with the lower valence band being composed mainly of N 2*s* states, and the upper valence band consisting mainly of N 2*p* states. The main influence of the N vacancy on electronic structure is observed near the CB edge, with the structure at higher levels also being little perturbed from that of the ideal crystal. As was true for the B vacancy, the electronic states associated with the vacancy itself make only a very small contribution overall. In contrast to the N vacancy and as expected, however, the states associated with the vacancy itself have a mainly *s*-type character, and make their main contribution within the vacancy band near the CB edge.

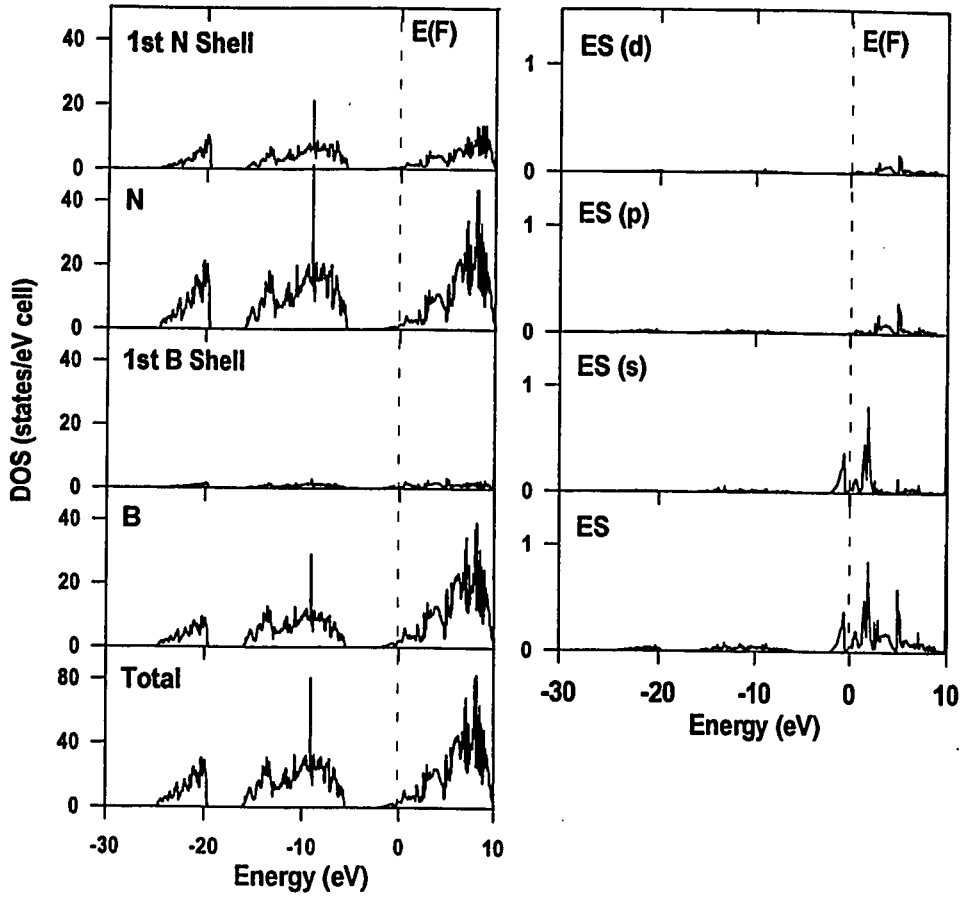

Figure 8. Total and partial DOS of c-BN supercell with N vacancy.

The N-vacancy band is not at all prominent, and its composition is more clearly revealed in Figure 10. The localization of the vacancy-band states is shown in Figure 10a, with the primary contribution being associated with the B atoms nearest the vacancy site. A smaller, but still significant contribution to the band is made by states associated with the N_1 shell, with only insignificant contributions being made by more distant coordinational shells.

In Figure 10b-d, the DOS is further decomposed to show the main orbital contributions to the vacancy band that arise from the B_1 and N_1 shells, and from states associated with the vacancy itself. Here the principal contribution to the vacancy band is clearly seen to be made by B_1 $2p$ states, with smaller admixtures being due to $2p$-type N_1 states and s-type states associated with the vacancy itself.

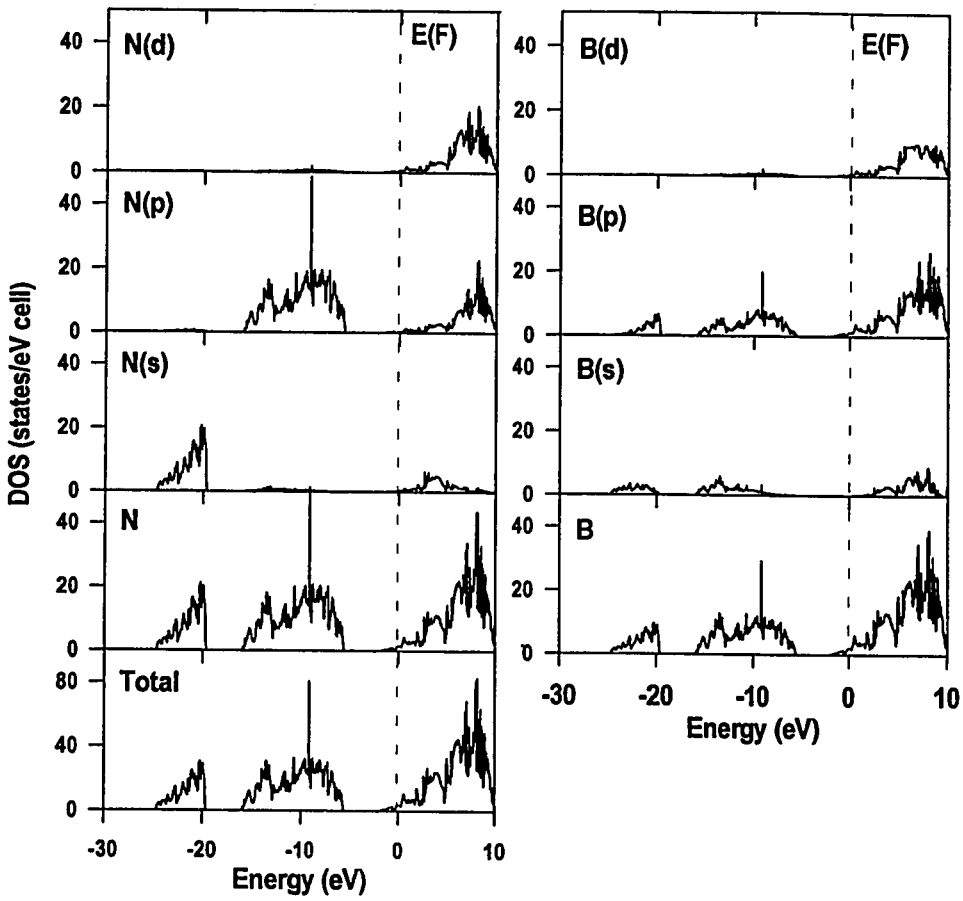

Figure 9. Total and partial densities of states for N-vacancy c-BN supercell.

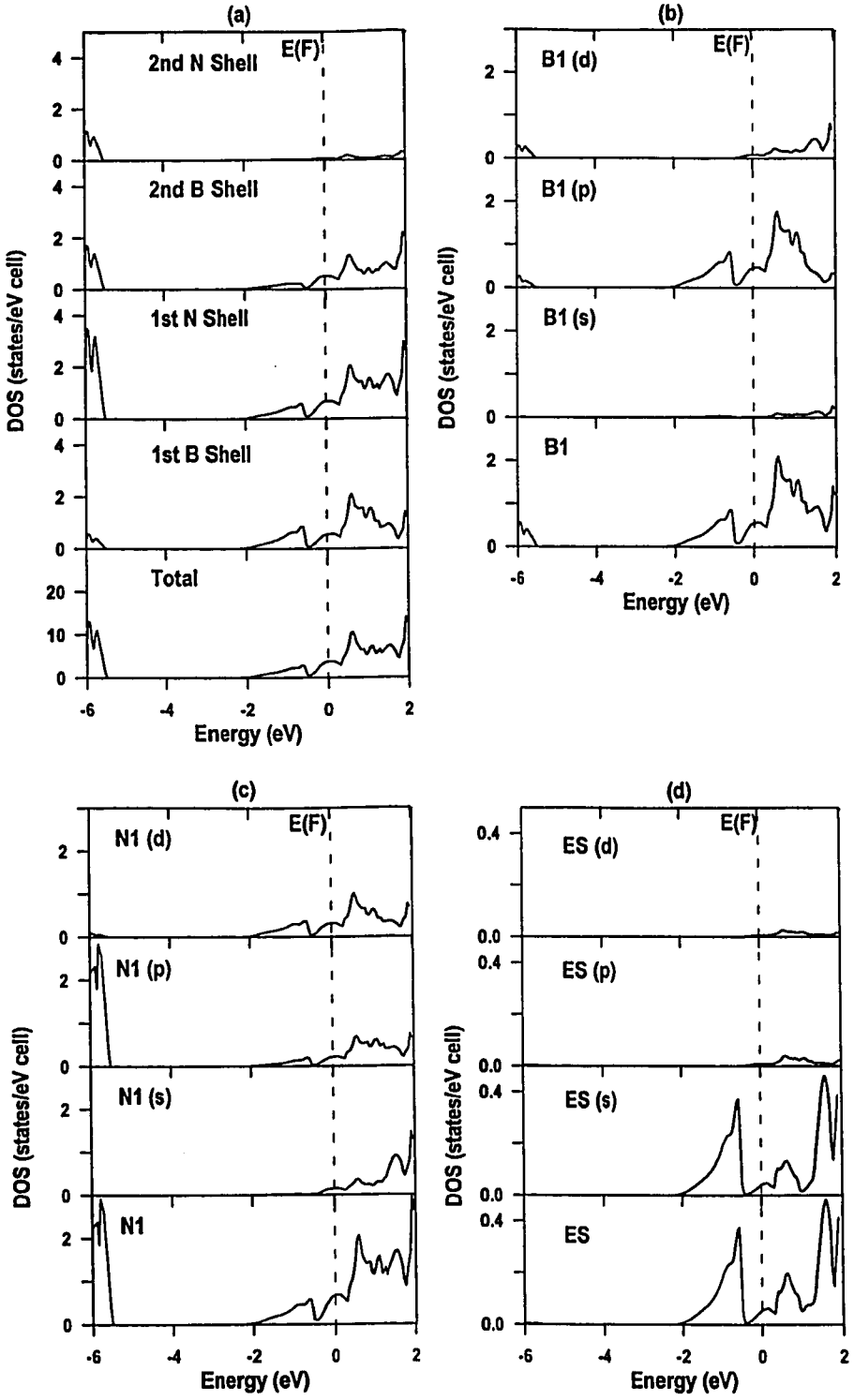

Figure 10. N-vacancy supercell DOS projected over (a) the first four coordinational shells, and (b) - (d) the orbital bases of the B_1, N_1, and vacancy states, respectively.

As was noted in the discussion of the B vacancy, there is a net transfer of charge from B to N in the ideal c-BN crystal of ~0.12 charges. The N vacancy site itself shows an even greater affinity for electrons of its neighboring B shell, with a transfer of nearly 0.6 charges from the four atoms of the B_1 shell. Beyond the second shell of B atoms, the distribution of charges is essentially unperturbed relative to that of the ideal crystal, a result that is consistent with the DOS projections discussed above.

These observations and previous observations regarding the behavior of the vacancy are clearly revealed in Figure 11. In Figure 11a, the role of *p*-type states of the neighboring B atoms is quite evident, as is the fact that these charges are strongly drawn toward the vacancy site. Though it is more evident in the DOS projections, the charges drawn into the vacancy region from the neighboring B atoms assume the lowest-energy 1*s*-type symmetry. The figure also shows the smaller contribution of $2p$ N_1 states to the vacancy band, with only minimal contributions arising from more distant atomic shells. The total charge density distribution in the (110) plane is illustrated in Figure 11b, where the large outward relaxation of B atoms from the vacancy site is clearly evident.

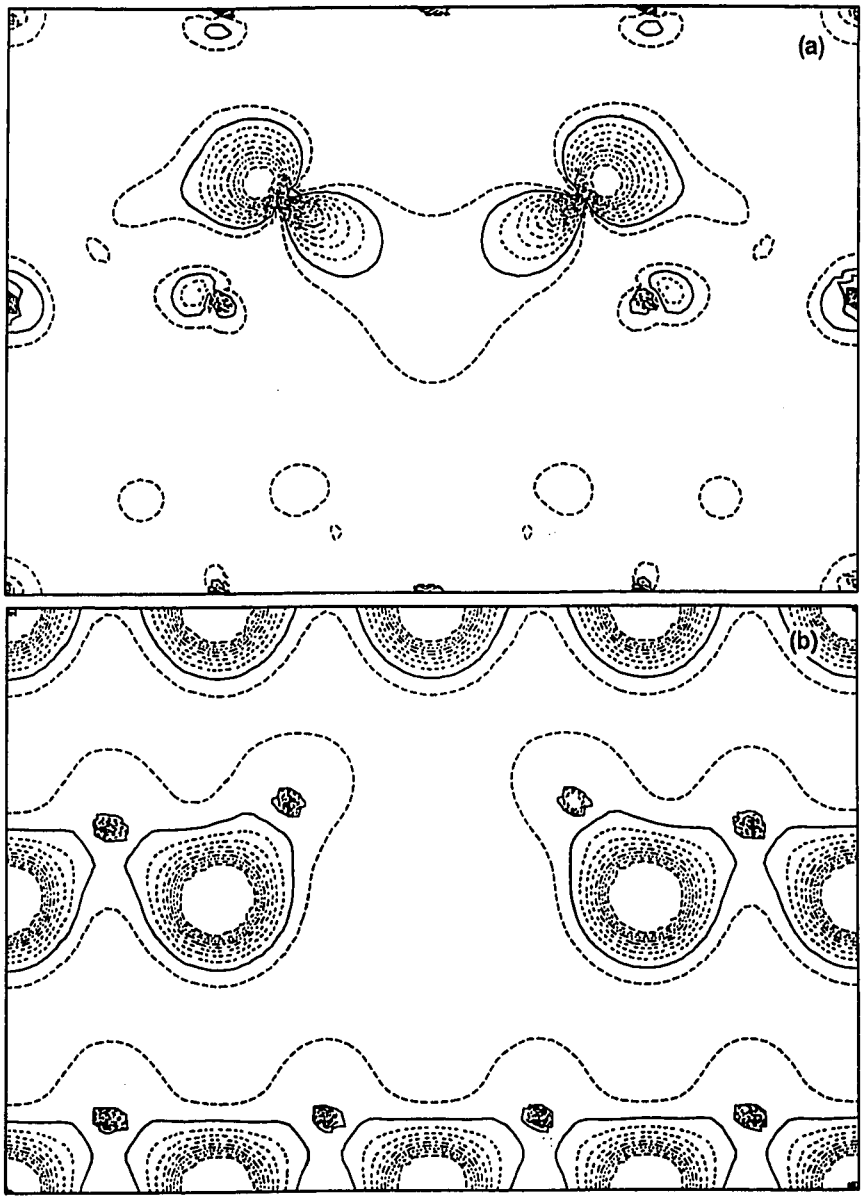

Figure 11. (110)-plane distribution of charges near the N vacancy in the c-BN supercell. (a) shows the distribution of charges within the vacancy band, while (b) shows the total charge-density distribution.

D. Impurities in c-BN

Isolated impurities in zinc-blende boron nitride were modeled in a manner similar to that used to investigate vacancies. In this case, the central B atom was replaced first with a Be impurity, then with a Mg impurity atom. In each case, the model represents an impurity concentration of 1.56%, distributed uniformly throughout an infinite crystal medium. In general, however, perturbations to the electronic structure are small or virtually non-existent beyond the first two coordinational spheres, and interaction between adjacent impurity supercells is minimal or nonexistent. To the extent that the impurity supercells are indeed effectively isolated, the features of electronic structure predicted by these calculations should also be evident at lower impurity concentrations as well. In this case, the main effect of concentration would be upon the amplitude of impurity-related features relative to the magnitude of host-crystal band structures.

As was done for the vacancy calculations, the radial relaxation of atoms in the coordinational shell adjacent to the impurity site was estimated by minimizing total energy versus nearest-neighbor coordinates. Figure 12 shows the variation in the total

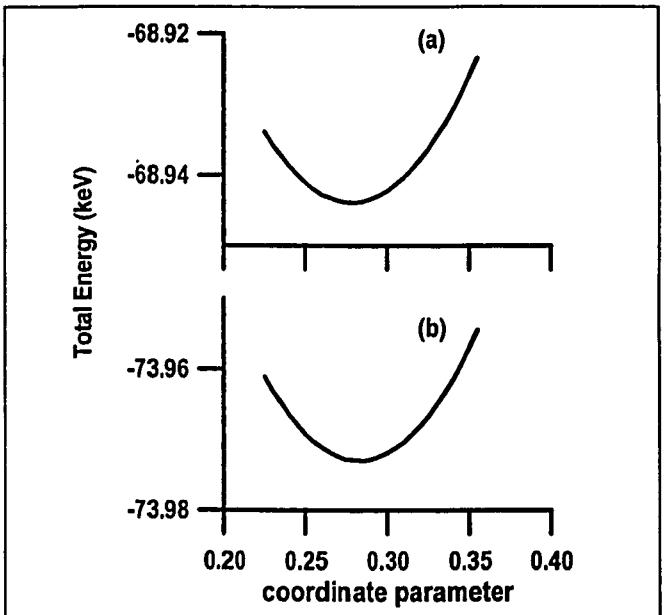

Figure 12. Total energy of 64-atom c-BN supercells with (a) Be, and (b) Mg impurities substituted for the central B atom.

energy of each impurity supercell versus the coordinate parameter of the N atoms nearest the impurity site. As in the case of the vacancy calculations, the relaxation is again outward. In this instance, the 1.74-Å outward relaxation predicted for N atoms nearest the Be impurity is essentially identical to the 1.78-Å outward relaxation predicted in the neighborhood of the Mg impurity. With only one fewer valence electron in the neighborhood of each impurity, the picture that emerges is consistent with the interpretation presented for the vacancy supercells. In this case, there is a stronger attraction between the atoms in the N_1 and B_1 shells than exists between the impurity and the neighboring N_1 shell. Though there remains an outward relaxation, the bonding between each impurity's two valence electrons and the neighboring N atoms resists the outward relaxation that was evident for the vacancy-supercell calculations. Given that the impurity atoms each have the same 2*s* valence configuration, and are each of only small-to-moderate size, it is also reasonable that the relaxation observed in the neighborhood of each impurity should be of very similar magnitude and stiffness, as is evident in the relaxation curves.

Both the total and the shell-projected DOS are shown in Figure 13 for the Be-impurity supercell configuration. With one fewer electron than the ideal c-BN system, the main effect of the Be impurity upon the host-lattice electronic structure (see Figure 2) is the creation of an acceptor-type resonance merged with the upper edge of the valence band. The Fermi level falls just above the resonance peak, leaving unoccupied valence states

that are consistent with the experimentally observed *p*-type conductivity reported for Be-doped c-BN.[26] Though its most significant contribution is near the VB edge, the direct contribution to the DOS is exceedingly small overall.

In Figure 14a-c, the composition of the VB edge states is revealed in greater detail. The small contribution at the VB edge of *p*- and *d*-type orbitals associated with the Be impurity itself is dwarfed by delocalized, mainly N 2*p* states. Such a degree of delocalization in the band-edge states suggests the possibility that *p*-type carriers produced by Be doping may have a high characteristic mobility. The DOS projections show the underlying bandstructure of the host lattice to

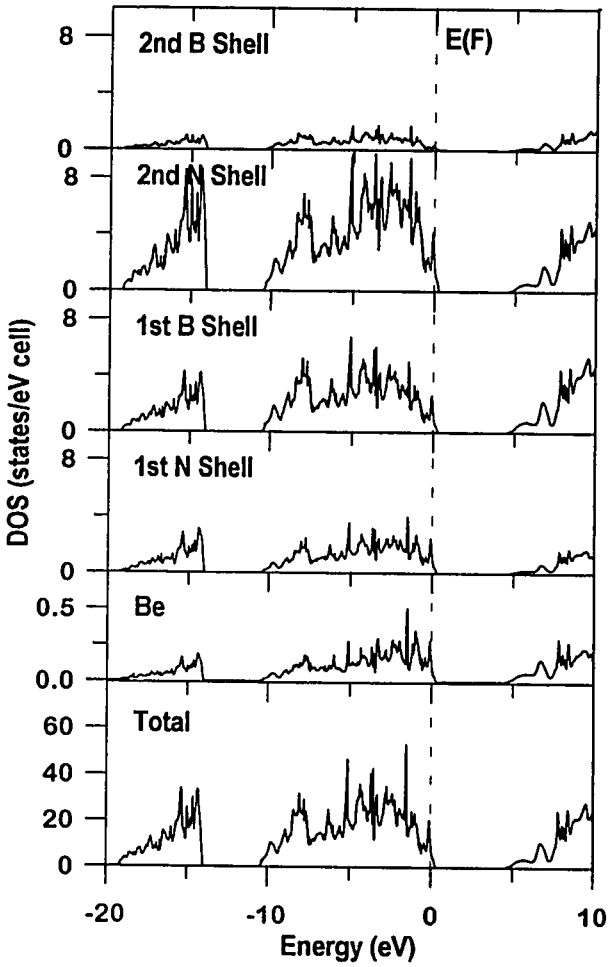

Figure 13. Shell-projected DOS for Be-doped c-BN.[12]

be perturbed very little except near the VB edge, where the formation of the impurity band and the shift in the Fermi energy from -2.54 eV in c-BN to -2.82 eV accounting for the principal electronic consequences.

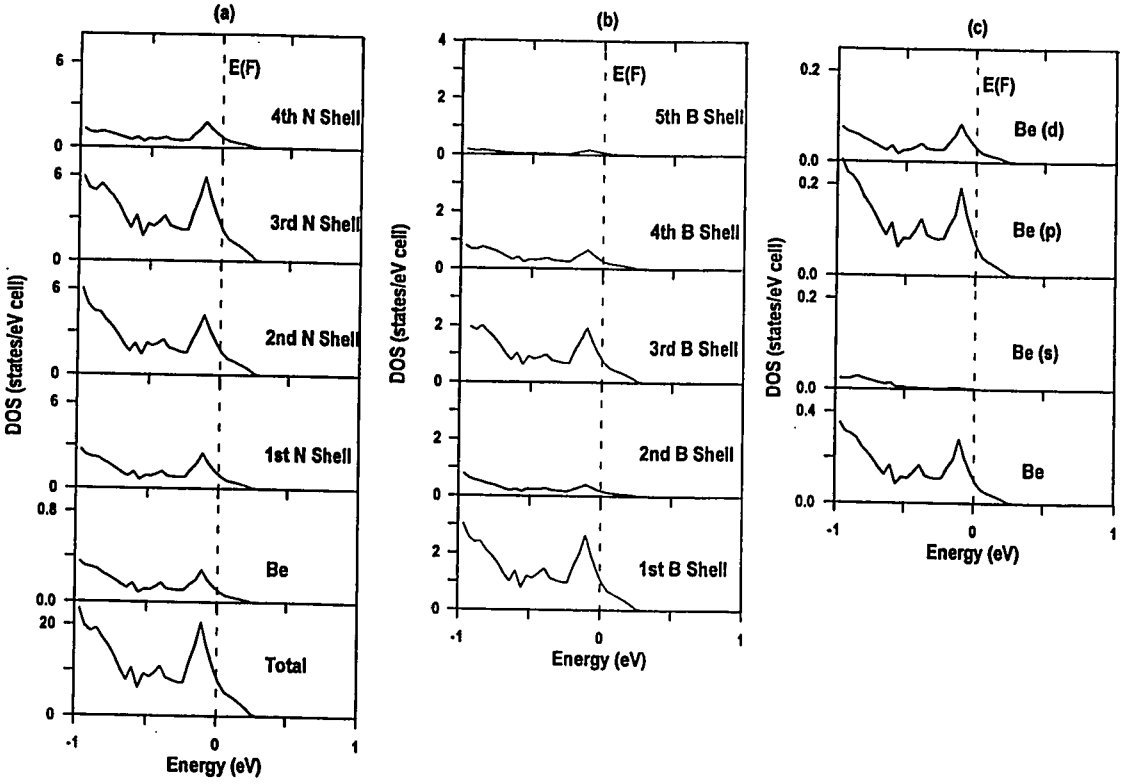

Figure 14. Total DOS and DOS projections over (a) the configurational coordinate spheres of N, (b) the B coordinational spheres surrounding the central impurity site, and (c) the orbital bases of the Be impurity.[12]

Figure 15a represents the distribution in the (110) plane of charges with energies near the Fermi energy, showing the shape of hole states associated with the VB edge. Further insight to the electronic structure is provided by the total charge-density distribution shown in Figure 15b. Here a greater transfer of charge is evident between the Be

impurity and the nearest N atoms than between B and N atoms. The high ionicity of the bonding between the impurity and its neighbors is largely responsible for the smaller relaxation of N atoms observed near the Be impurity.

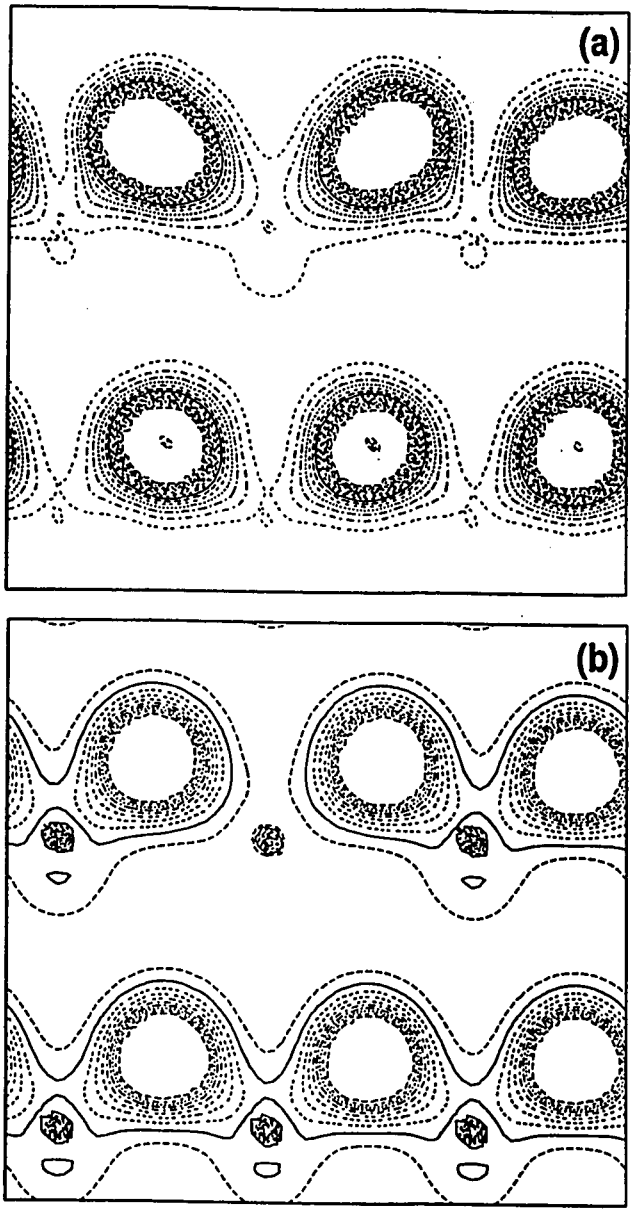

Figure 15. (110)-plane charge density distribution for (a) electrons with energies near the Fermi level, and (b) all valence-band electrons.[12]

The total and shell-projected DOS for the partially relaxed Mg-impurity supercell are shown in Figure 16. As may be expected from the similarity of these atoms' valence configurations and small-to-moderate size, the effects of the Mg and Be impurities upon the host-lattice electronic structure are quite similar in many respects. Again, the main effect of the impurity is the formation of an acceptor-type impurity resonance merged with the VB edge. The Fermi level of the Mg-doped c-BN supercell is almost identical to that of the

ideal c-BN configuration, however. A considerable though lesser delocalization of the VB states is also evident, mainly among 2*p* states of N. As was observed for the Be impurity, the contribution of the Mg impurity to the total DOS is greatest near the VB edge, although its direct influence upon electronic structure is everywhere virtually negligible in comparison with that of the perturbed host-lattice N and B atoms.

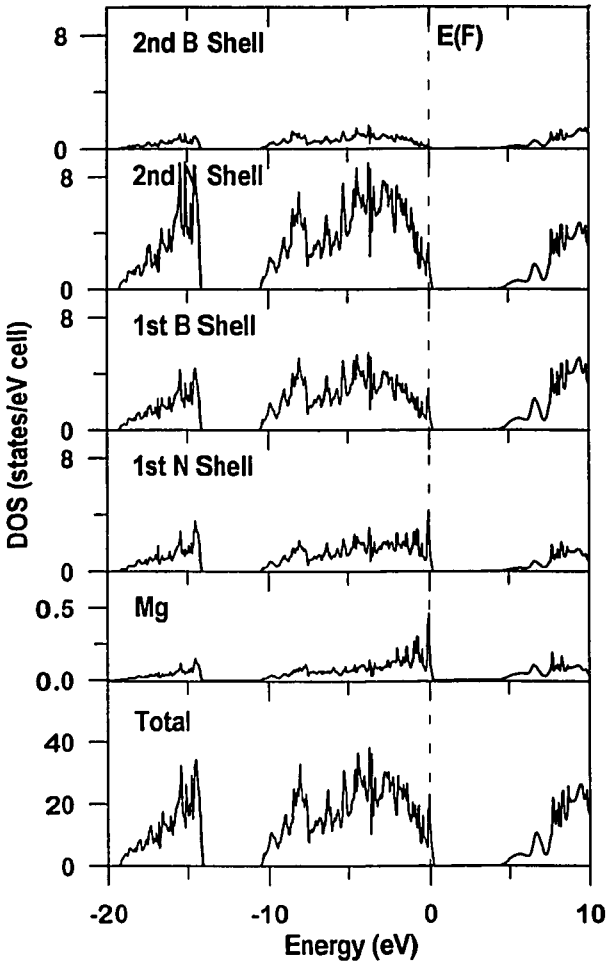

Figure 16. Total and shell-projected DOS for the Mg-impurity supercell of c-BN.[12]

Figure 17 shows the composition of the VB edge in greater detail. The relative contributions of B and N states to the band-edge DOS is overall very similar to that in the unperturbed crystal, while the direct contribution of the Mg impurity to the VB edge is through a hybridization of Mg 3*p* and 3*d* states with 2p states of the first N shell.

Figure 18a shows the distribution of charges in the vicinity of the VB edge in the (110) plane, showing both the relaxation of the band-edge charge configuration and the *p*-type character of the charges associated with N atoms of the first coordinational sphere. Also evident in this figure is the greater degree of localization that occurs for the charges in the vicinity of the VB edge, as compared with the corresponding band-edge distribution of charges for the Be impurity.

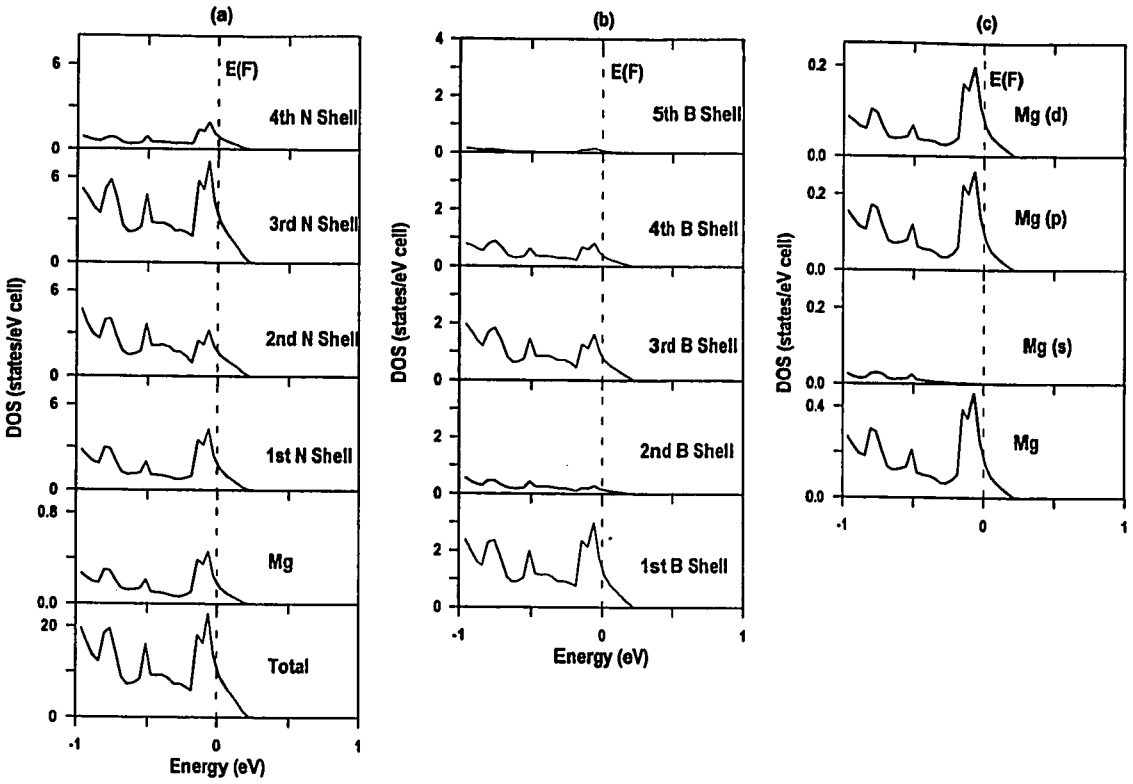

Figure 17. Total DOS and DOS projected over (a) the coordinational spheres of N atoms surrounding the Mg impurity, (b) the different coordinational shells of B, and (c) the orbital bases of the Mg impurity.[12]

Likewise, the total valence charge distribution shown in Figure 18b shows the bonding between Mg and N atoms to be even more ionic than that between the Be and N atoms shown in Figure 15b, a fact that is reflected numerically in the average charge associated with each of the highly overlapping atomic shells in the impurity supercell. Compared with an isolated Mg atom, this assignment of charge to the different coordinational spheres shows the almost complete transfer of a Mg electron, which is manifested mainly as an increase in the charge density in the N_1 coordinational sphere. This compares with a net loss of only ~0.4 electrons from the Be impurity, the charge from the Be impurity being also much more uniformly distributed among more distant atomic shells. While the Mg

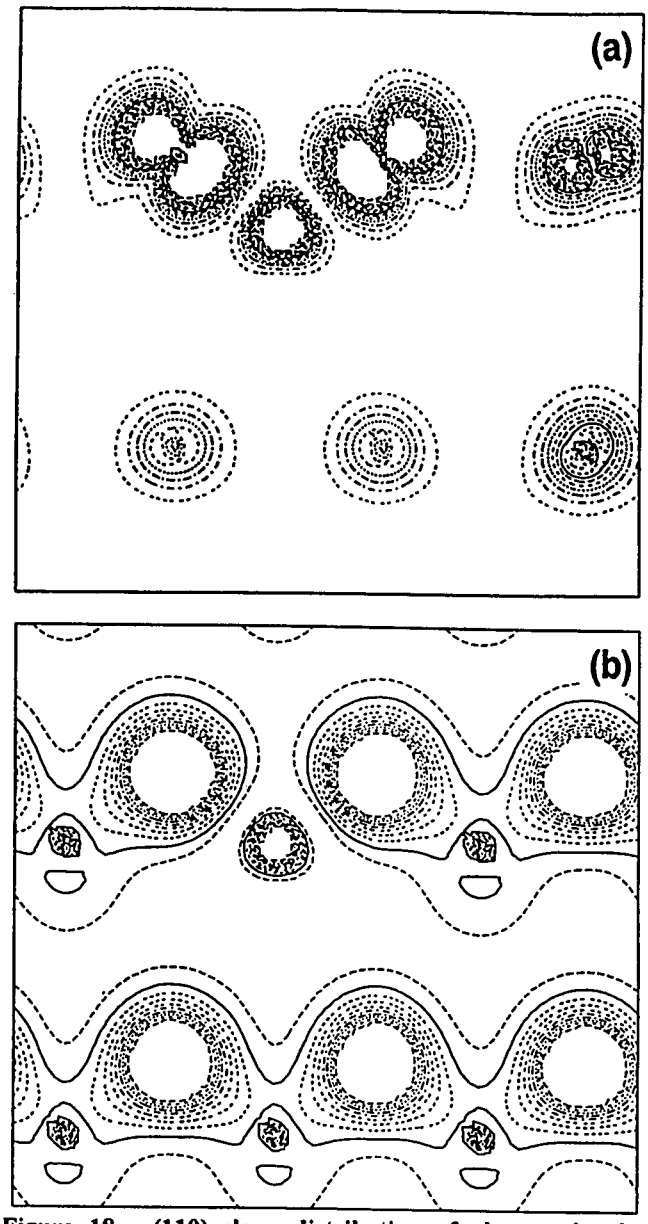

Figure 18. (110)-plane distribution of charges in the vicinity of the Mg impurity in c-BN. (a) shows the distribution of charges near the Fermi energy, while (b) shows the total charge-density distribution.[12]

impurity in the c-BN supercell does create an acceptor-type band merged with the VB edge, the more highly localized nature of the states in this band suggests that the associated holes will exhibit mobility smaller than those associated with the Be impurity.

E. Summary of results for vacancies and impurities in c-BN

The effects of anion and cation vacancies and Be and Mg impurities upon the electronic structure and chemical bonding of zinc-blende boron nitride was investigated by performing band-structure calculations using large 64-atom supercells. Because such calculations would be prohibitive for more detailed full-potential models, the investigation began with a series of calculations to benchmark the performance of the more efficient LMTO technique against these codes for the case of the ideal c-BN crystal. These calculations showed excellent agreement between the predictions of the LMTO-ASA technique and corresponding results obtained from FP-LMTO and FP-LAPW calculations. A further comparison of LMTO-ASA calculations performed with and without empty spheres located at interstitial sites showed the use of such empty spheres to be unnecessary. Based on these calculations, a detailed discussion of the electronic structure and bonding in the ideal c-BN crystal was presented in the context of their physical and technological significance.

For each of the vacancy and impurity supercells, a series of calculations was performed to estimate the radial relaxation of atoms nearest the vacancy or defect site. The equilibrium relaxation was found by minimizing supercell total energy with respect to the radial coordinate of nearest-neighbor atoms. The narrow width of the vacancy band introduced by the B vacancy just above the VB edge suggests that B vacancies are likely to produce *p*-type carriers with a low characteristic mobility. In contrast, the low and broad N

vacancy band is more consistent with higher carrier mobility. The high resistivity typical for actual samples known to have high N-vacancy densities may not be an intrinsic characteristic of the *n*-type N-vacancy carriers, but may instead result from trapping of these carriers at other types of defect and impurity sites, or within more complex defect structures.

Be and Mg impurities were substituted into the cation sublattice of c-BN. Given the similarity in the valence configuration of these atoms, it was not surprising to observe very similar effects upon electronic structure, relaxation, and chemical bonding for each impurity. While each impurity caused virtually identical large outward relaxations of nearest-neighbor N atoms, the outward relaxation was significantly smaller than that observed for the vacancy supercell calculations. Taken together, the pattern of relaxation for the vacancies and impurities presents a picture that is physically plausible and has a high degree of self consistency. In each case, the large outward relaxation is a manifestation of the strong, highly ionic bonding between B and N atoms in the atomic shells nearest the vacancy or impurity site. The bonding of the valence electrons of the impurities opposes this outward relaxation to some extent, and the very similar configuration for each of the impurities results in virtually identical relaxation in the vicinity of each.

Likewise, each of the impurities introduces an acceptor-like band that is merged with the valence band of the host crystal. The Fermi level occurs slightly above the peak of the impurity band in each case, leaving unoccupied states between the Fermi level and the VB edge. The density of *p*-type carriers should be readily controlled by varying the doping concentration of these substitutional impurities. Although *p*-type conductivity can be obtained from either impurity, the more localized distribution of charges near the Mg impurity is likely to yield carriers with lower characteristic mobility.

IV. DEFECTS AND IMPURITIES IN ZINC-BLENDE ALUMINUM NITRIDE

A. Introduction

Like the other III-V nitrides, AlN usually crystallizes in the wurtzite phase, but is also known in the zinc-blende (c-AlN) phase. Despite the indirect nature of its band gap, c-AlN is of considerable physical and technological interest because of its full miscibility with the corresponding phases of Ga and In nitrides and SiC, its excellent 3% lattice matching to c-GaN, and its very large 6.2-eV band gap.[5] This combination of properties in both the wurtzite and the zinc-blende phases has created interest in AlN as an alloying constituent, especially with GaN where the excellent lattice matching permits fabrication of high-quality alloy crystals, as well as compositionally graded structures and heterostructures with minimally strained interfaces. While these properties of AlN provide very intriguing degrees of freedom for band-structure engineering, AlN and its alloys are also of interest as buffers for growing the full compositional range of $Al_xGa_{1-x}N$ on (0001) sapphire substrates.[27]

Central to practical applications of AlN, as with any semiconducting material is the ability to produce crystals with majority carriers of both types. To this point, however, no technique has been successful for reproducibly doping AlN,[28] making theoretical investigations essential in order to guide further process and materials development. As with other III-V nitrides, the low solubility and high vapor pressure of N seriously limits the quality of crystals grown from solution, and heteroepitaxial growth techniques are

typically used to obtain the highest quality crystals. Even with the use of such techniques, significantly sub-stoichiometric concentrations of N are believed to be principally responsible for creating high concentrations of *n*-type carriers. With typical electron concentrations in the range of 10^{18} to 10^{19} cm^{-3}, *p*-type conductivity has been demonstrated with Se and Zn dopants, but the resulting crystals were highly resistive and were poorly reproducible.[7] By annealing Mg-doped crystals in an N_2 atmosphere, Nakamura and coworkers[29] have reported significant improvements in hole-carrier concentrations for GaN, and similar techniques may prove useful for AlN.

The discussion that follows involves calculations that were performed to investigate the behavior of Mg substitutional impurities in zinc-blende AlN. As in the case of c-BN, the goal was to represent the impurity supercell system without the use of empty muffin-tin spheres in the interstitial regions between atoms. In comparing the results of ideal c-AlN calculations performed both with and without the use of such empty spheres however, it was found that the no-empty-spheres model yields results of sufficiently good quality only in the valence-band region. Though there are qualitative similarities between the two models in terms of their representation of conduction-band electronic structure, quantitative comparisons here show significant discrepancies. In a sense, the relatively poor performance of the no-empty-spheres model should not be too surprising after considering the much higher ionicity of bonding and the larger spacing of atoms in the AlN system, as compared with the BN system. While good results were obtained from

the simple no-empty-spheres model in BN, the higher ionicity of AlN evidently creates a more complex potential and wavefunction in the interstitial regions. Given that the effects of the acceptor-type Mg impurity are localized to the edge of the valence band, calculations were performed using both models, with the interpretation of the no-empty-spheres model being limited to estimating the radial relaxation of nearest neighbors, and to the effects of such relaxation upon the electronic structure near the VB edge.

B. Ideal c-AlN

Figure 1 shows the band structure of ideal c-AlN, as calculated (a) with empty spheres, and (b) without empty spheres in the LMTO-ASA band structure model. As is evident from the figure, the valence-band states are well represented in the no-empty-spheres

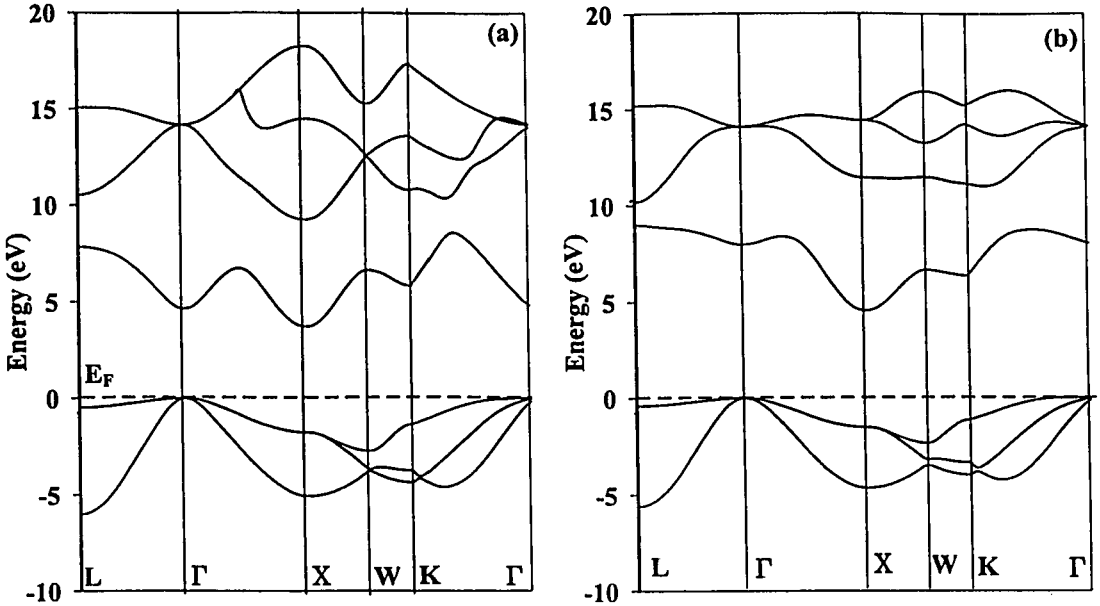

Figure 1. Band structure of c-AlN, as predicted by LMTO-ASA calculations (a) with empty spheres, and (b) without empty spheres. The structure of CB states is approximated well in the no-empty-spheres model. The lower conduction band is qualitatively similar, but clearly distorted in (b). Higher-lying levels are reproduced even more poorly in the latter case.

model, but the shape of the conduction-band states is significantly distorted. Table I is a quantitative comparison of the band structures shown in Figure 1 with each other and with the results of independent calculations performed previously. In general, the band gaps predicted by the model that incorporates the empty spheres correspond reasonably well with those obtained previously, while those predicted by the no-empty-spheres model are significantly expanded, in general. An indirect band gap is predicted in each case, with the minimum of the conduction band occurring at the X point of the Brillouin zone, and the valence-band maximum being formed by three degenerate subbands at the center of the IBZ. While there is good consistency between the calculations performed with empty spheres and the results of independent band-structure calculations, the calculation without empty spheres fails mainly in its ability to represent conduction-band states. Valence-band dispersion is well-reproduced, both in terms of the total band width, and in terms of the detailed shape of the curves.

Table I. Comparison of gap widths obtained by present and earlier LMTO calculations. W_V refers to the width of the valence band.

Gap Widths	Empty Spheres	No Empty Spheres	Other Works
Γ_v - Γ_c	4.67	7.96	4.53[a], 4.52 (6.0)[b]
Γ_v - L_c	7.84	8.99	7.64[a], 7.65 (9.15)[b]
Γ_v - X_c	3.75	4.55	3.40[a], 3.36 (4.9)[b]
W_v	5.98	5.60	

[a] LMTO-ASA, Ref. 17
[b] Citation in Ref. 17 to unpublished LMTO calculations performed by W.R. Lambrecht and B. Segall. Values in parentheses include a band-gap correction based on the use of an external potential.

Figure 2 and Figure 3 show both the total DOS and the orbital-projected DOS for ideal c-AlN, as predicted both with and without empty spheres. Though there are some

differences in the valence-band structure, the overall character of the DOS and DOS projections is very similar for the two valence band calculations, especially in the region nearest the band edge.

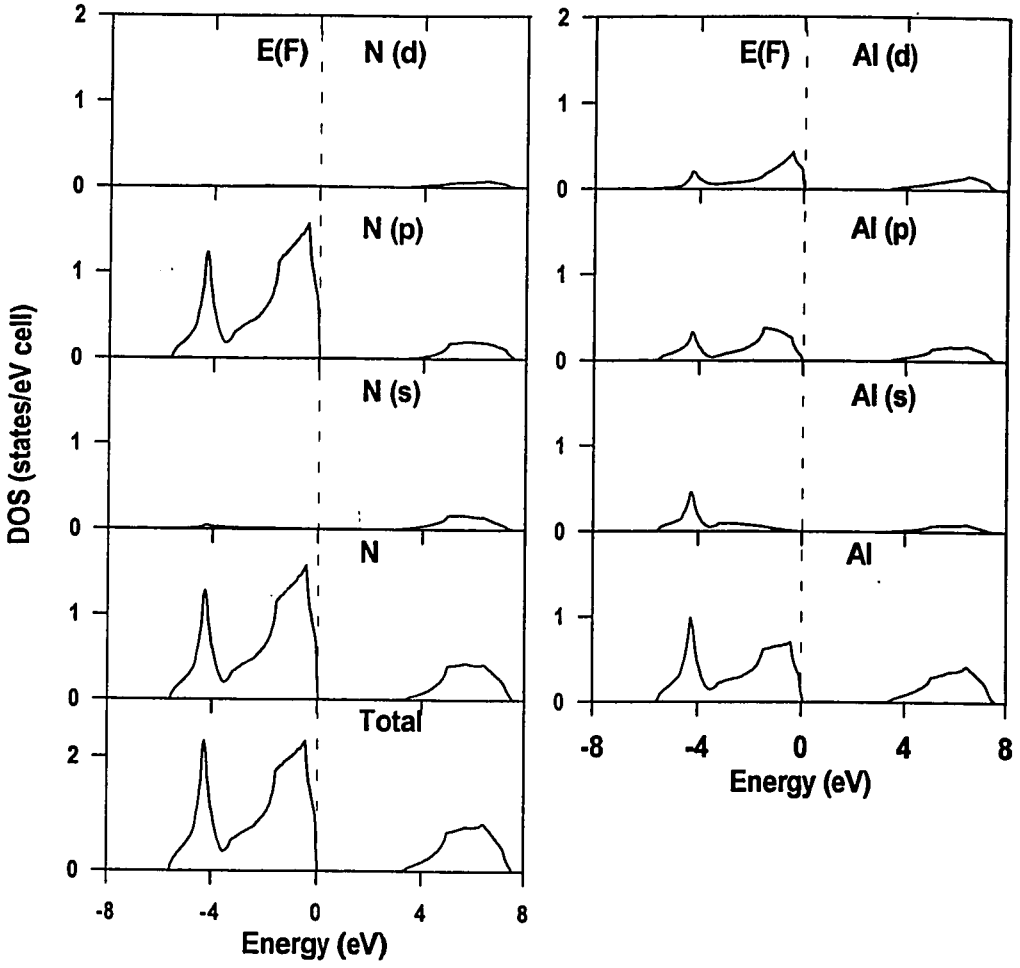

Figure 2. Total and partial DOS for ideal c-AlN, as predicted by LMTO-ASA calculations with empty spheres

In contrast, the two calculations present a much different picture for the conduction band, and the calculation performed without empty spheres is certainly unreliable in this region. In each case, the projections show the valence band to consist mainly of $2p$ states of N,

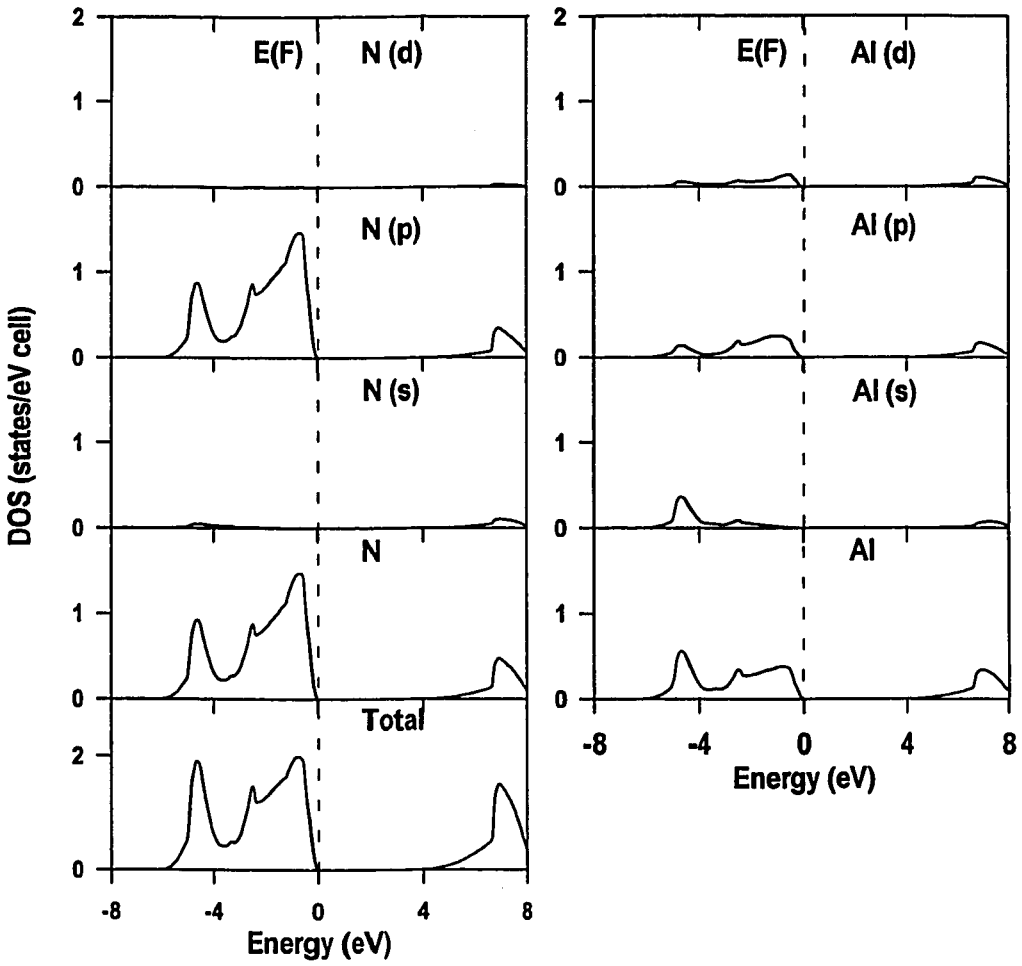

Figure 3. Total and partial DOS for ideal c-AlN, as predicted by LMTO-ASA calculations with no empty spheres.

with small admixtures from Al 3*p* states throughout. Small contributions are made to the lower part of the valence band by 3*s* Al states, while Al 3*d* orbitals contribute near the VB edge in approximately the same measure as 3*p* Al states.

Figure 4 shows the distribution of charges predicted for ideal c-AlN, as determined by the LMTO-ASA calculations performed with empty spheres. As was seen for the c-BN

calculations, there is a considerable accumulation of charges on the N atoms. As expected, the net effective transfer of charges between the constituent atoms is significantly larger in the c-AlN than for the c-BN calculations.

Given that the characteristics of the occupied valence-band states govern bonding and that the influence of acceptor-type impurities is localized to the region near the VB edge, the no-empty-spheres model should be capable of representing the essential features of band structure and nearest-neighbor relaxation for the Mg impurity. This expectation is reasonably borne out in the discussion that follows in which both models were used to investigate the electronic structure of the Mg-impurity supercell.

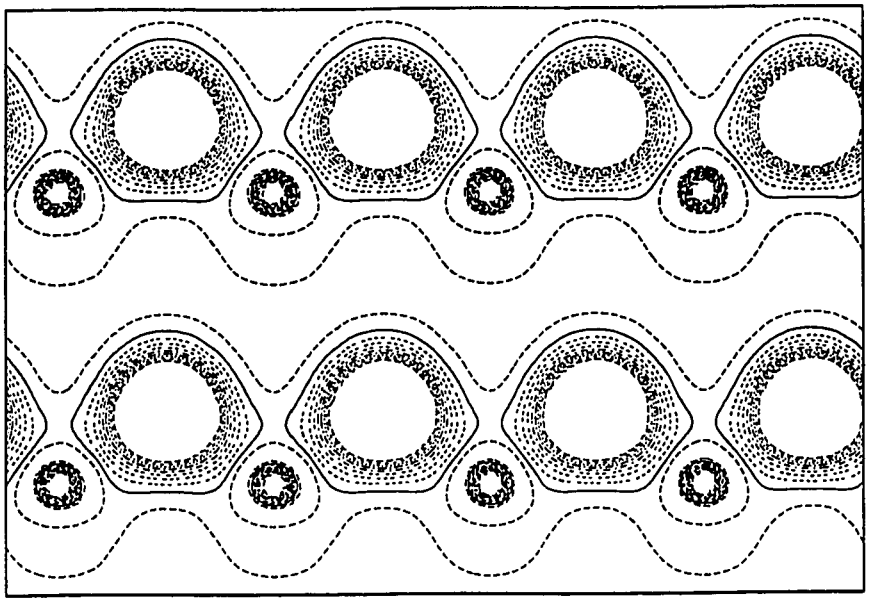

Figure 4. Predicted distribution of charges in the (110) plane of ideal c-AlN.

C. Mg impurity substituted to the Al sublattice of c-AlN

Total-energy minimization using the no-empty-spheres LMTO model revealed only a relatively small outward relaxation of the N atoms that surround a Mg impurity substituted to the Al sublattice of c-AlN, as shown in Figure 5. Here the outward relaxation to 1.32 Å is only 2.0% larger than the normal 1.30 Å bond length between anions and cations in the ideal crystal.

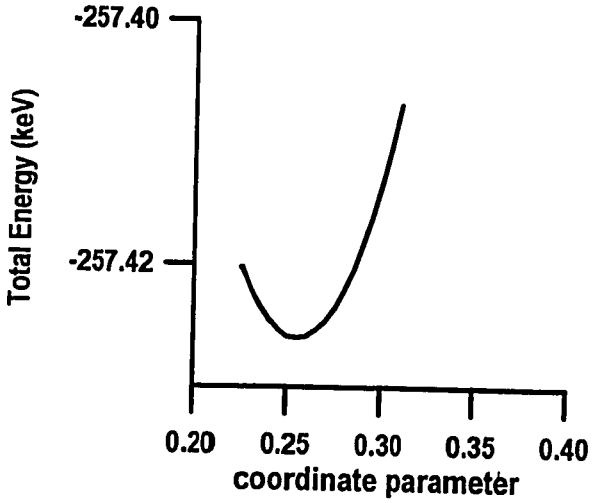

Figure 5.Radial relaxation of N atoms nearest a Mg impurity substituted to the Al sublattice of c-AlN. The shape of the relaxation curve suggests that the atoms near the Mg impurity are held relatively rigidly in comparison to those near the defects and impurities considered for c-BN.

Figure 6 shows the total DOS for the Mg-impurity c-AlN supercell, as determined from LMTO calculations performed with and without interstitial empty spheres. Here is evident a narrow ~0.15-eV acceptor band introduced to the VB edge by the impurity, with other features of the electronic structure being essentially the same as those of the ideal crystal. The total and shell-projected DOS for the no-empty-spheres supercell calculation are shown for the relaxed configuration in Figure 7. Here a very similar pattern is seen overall, with the impurity band appearing at the same energy as before. There is a very small redistribution of levels in the no-empty-spheres case that gives the impurity band a

somewhat higher apparent amplitude, while concurrently reducing the apparent density of states just below the energy of the impurity peak. This difference is much less significant than it may first appear however. In fact, both the position and the area of the two predicted impurity bands are virtually identical. Unfortunately the differences between the calculations do not permit a direct comparison of the DOS projections. The similarity between the total DOS figures however gives confidence in the use of the no-empty-spheres results as before for studying the orbital composition and localization of the acceptor states in the impurity band structure. In Figure 7, the acceptor states are seen to be rather strongly localized to the impurity and the neighboring shell of N atoms.

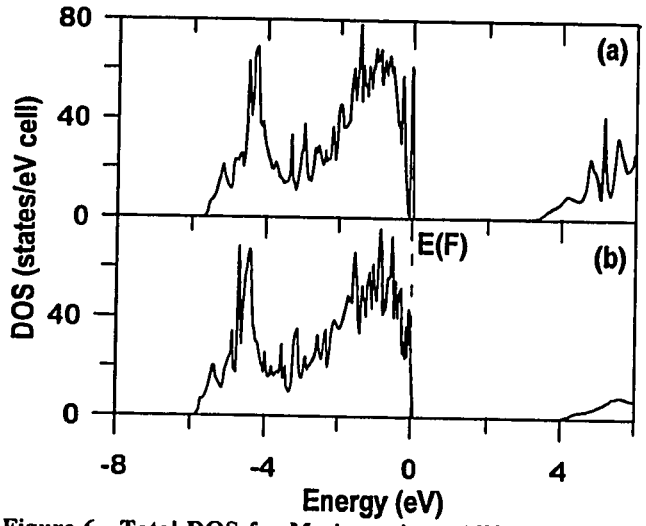

Figure 6. Total DOS for Mg-impurity c-AlN supercell, as determined by LMTO-ASA calculations (a) with and (b) without interstitial empty spheres.

The orbital composition of the Mg acceptor level is shown in Figure 8. Here the character of the impurity component of the acceptor level is seen to be mixed nearly evenly between *p*- and *d*-type orbital components, while the neighboring N atoms are seen to consist purely of *p*-orbital components.

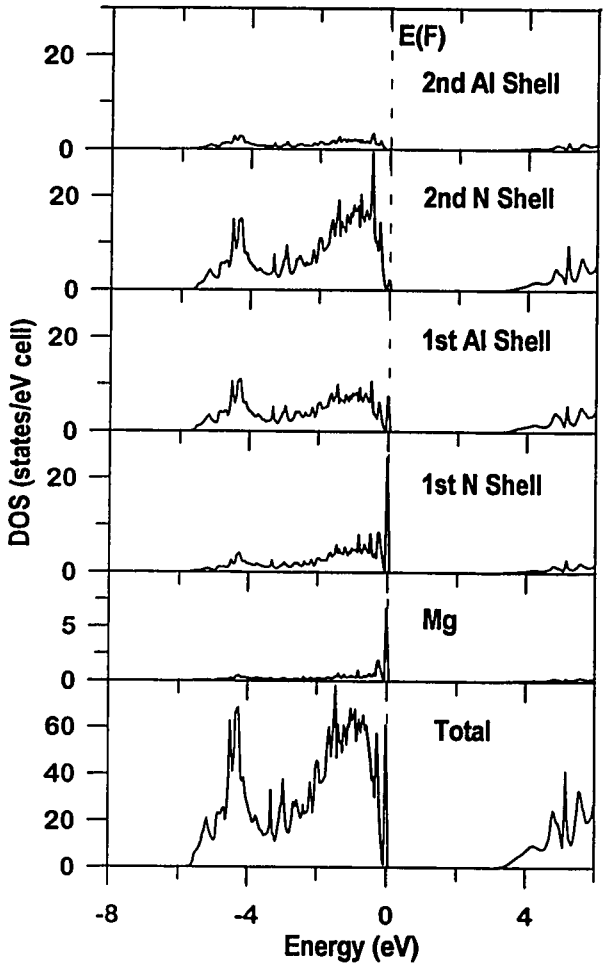

Figure 7. Total and shell-projected DOS for c-AlN supercell with Mg impurity substituted to the cation sublattice.

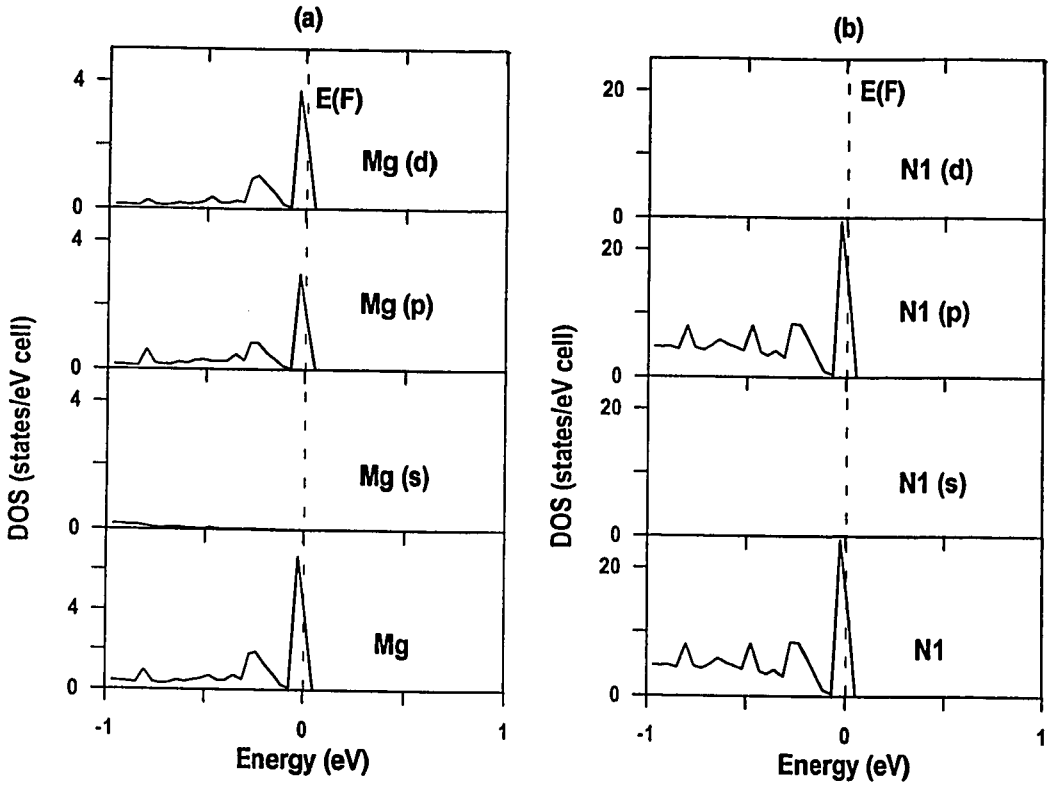

Figure 8. Atomic and orbital shell projections of the DOS near the Mg impurity acceptor level at the VB edge of c-AlN.

The distribution of charges near the Mg impurity site is shown in Figure 9. Both parts of the figure show the highly localized accumulation of charges on the Mg atom. Although the detail of this projection fails to show the *d*-type symmetry in the Mg orbital, it shows very clearly the dominant role of the 2*p* N orbitals in the formation of the vacancy band and in their interaction with the Mg impurity. The lower panel shows the highly ionic nature of the bonding between the Mg and its neighboring N atoms. Importantly, however, the lower panel also shows a very striking resemblance in regions separated

from the impurity to the charge-density distribution produced in the ideal c-AlN calculations that were performed with empty spheres. This gives further support to the claimed validity of the no-empty-spheres model for predicting the valence-band bonding characteristics.

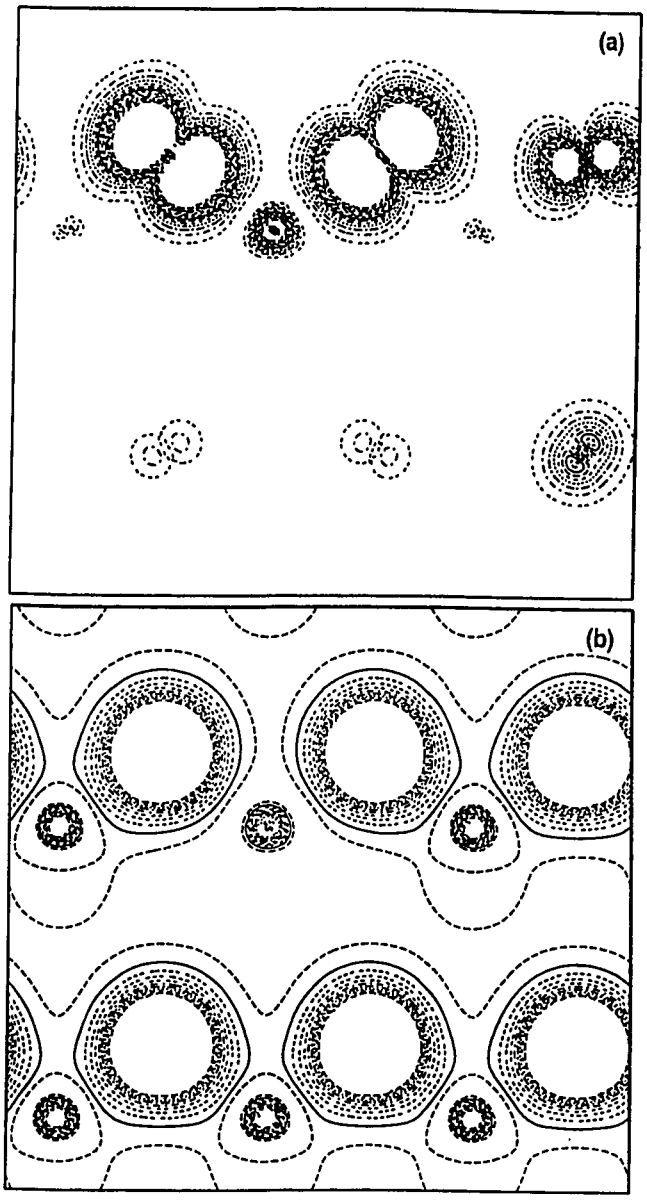

Figure 9. (110)-plane distribution of charges for the Mg-impurity c-AlN supercell. (a) Distribution of charges associated with the acceptor band. (b) Total charge distribution.

D. Summary of results and conclusions for Mg substitutional impurities in c-AlN

Benchmark calculations were performed to assess the validity of LMTO calculations for representing the electronic structure of c-AlN. Two techniques were evaluated in the benchmark calculations. In the first, empty muffin-tin spheres were used to represent the wavefunctions and potential in interstitial regions between atomic muffin-tin spheres. No such empty spheres were used in the second set of calculations, with a larger degree of overlap between atomic spheres being used to compensate for the missing empty spheres. The second model architecture was used successfully in the series of calculations performed for c-BN, and is preferred because it affords greater computational efficiency and is physically simple enough to permit the determination of first-order lattice-relaxation effects.

The calculations performed with empty spheres showed good correspondence both in qualitative and quantitative aspects of bandstructure predicted previously in independent calculations. The no-empty-spheres calculations, however, were found to have only a very restricted range of validity, showing an acceptable degree of accuracy only in their description of the valence-band states. Because of its acceptable description of the valence-band structure, the no-empty-spheres technique was judged to be probably valid for the description of acceptor type impurities such the Mg impurity of interest. To test this hypothesis, calculations were performed using both models and comparisons made between the predictions of each.

The relaxation curves obtained from the no-empty-spheres calculations showed a fortuitously small outward relaxation for the atoms nearest the Mg impurity in the c-AlN supercell. This small 2% relaxation permitted a direct comparison between the unrelaxed calculation performed with empty spheres and the nearly identical relaxed configuration whose band structure was calculated without empty spheres. Each of the calculations showed a narrow partially occupied acceptor band located near the VB edge, the consistency between the predictions supporting the restricted use of the simpler no-empty-spheres model construction. The DOS projections showed these hole states to be highly localized to the region near the impurity, as in the case of the corresponding impurity in c-BN.

V. DEFECTS AND IMPURITIES IN ZINC-BLENDE GALLIUM NITRIDE

A. Introduction

Although it is the wurtzite phase of GaN that occurs most commonly, the metastable zinc-blende phase can also be grown on GaAs substrates.[30] Though the quality of such films is presently inferior to that of wurtzite-phase GaN grown on sapphire, the cubic system is of interest for many of the same physical and technological reasons that have been previously enumerated for both c-BN and c-AlN, but is especially interesting because of the successful technological applications that have been achieved in the closely related wurtzite-phase alloys with nitrides of Al and In.[1, 3-5] As before, the central interest of the present study is both to understand and to predict the effects of various point defects and impurities upon the electronic structure and chemical bonding characteristics of the cubic phase of GaN. Here again, the principal goals are to develop insights that may lead to improved techniques for producing materials of both conductivity types, and for tailoring important electronic properties, including carrier density, carrier mobility, and the detailed structure of states in the electronically active region in and near the principal band gap.

The calculations reported below required two refinements: the addition of empty spheres in interstitial regions between atomic muffin-tin spheres, and the treatment of semi-core 3*d* orbitals of Ga as valence states. The empty spheres improved the representation of the potentials and wavefunctions in the interstitial regions, while the treatment of the Ga 3*d*

orbitals was necessary to account for the now well established mixing that occurs between them and the 2*s* orbitals of N, which fall at nearly the same energy.[17,31] Unlike the case for the AlN calculations, the combination of high ionicity and the complexity of the Ga wavefunctions did not permit even a limited use of a no-empty-spheres supercell model.

The addition of two empty spheres per unit cell doubled the number of sites in the supercell from 64 to 128, though the downfolding of *p* and *d*-type orbitals in the empty spheres considerably mitigated the additional computational requirements. Nevertheless, the added complexity of the c-GaN supercells added considerably to the computer time required to achieve self consistency. Depending upon the nature of the defect or vacancy being represented, the computational time required to complete a single iteration of a c-GaN supercell calculation ranged between 28.0 and 29.5 minutes, when using 100% of a single CPU on a Cray J90 computer. Comparable times for c-AlN calculations without empty spheres ranged between 5.1 and 5.3 CPU minutes. In terms of the scope of work completed in this series of calculations, the main consequence of the added complexity was to preclude the type of total-energy minimization by which the radial relaxation of nearest neighbors was estimated elsewhere. A limited effort made in such an undertaking demonstrated such relaxation to be difficult at best, while the complex relationships between atomic and empty spheres does not at this point suggest a clearly reliable approach for accommodating such relaxation in any case.

As in the other materials considered here, N vacancies are prevalent in GaN crystals, and are believed to be responsible for the high concentrations of *n*-type carriers that are observed in as-grown samples. Likewise, O is known as a common impurity, and probably contributes somewhat to the high electron concentration (typically greater than 10^{18} cm^{-3}) usually observed in GaN samples.[6] Ga vacancies, which have been observed in GaAs,[32] have also been suggested to play an important role in the self-compensation of GaN.[8] While reproducibly high *p*-type conductivity was first achieved by using Mg impurities in epitaxially grown crystals,[33] the *p*-type impurities considered here include only Cd and Zn. substitutions to the cation sublattice. The latter has been effectively used for example as an acceptor-type impurity in the InGaN layer of double heterostructure LEDs.[3] Mg-impurity calculations will be reported separately.[13]

As a result of the complications described above, the results reported below have been calculated without any consideration of relaxation effects. Given that the results of previous calculations have shown these effects to be quite large in some cases, it is important to bear this limitation in mind when interpreting the results.

B. Ideal c-GaN

All of the results reported below are based on calculations in which the lattice constant was fixed at 4.49 Å. The band structure of ideal c-GaN, as calculated by the LMTO-ASA technique is shown in Figure 1. As was noted above, these results were obtained by treating semi-core Ga 3*d* states as valence and by using empty muffin-tin orbital spheres to describe the potential in interstitial regions. The band-gap exhibited at the center of the Brillouin zone is direct, while the lower valence band shows the strong mixing of N 2*s* and Ga 3*d* states discussed above. Except in the high-energy conduction-band regions, there is an very good overall agreement of these results with those obtained by in previous calculations by others. This agreement is reflected in the comparisons at high-symmetry points of the IBZ, presented in Table I.

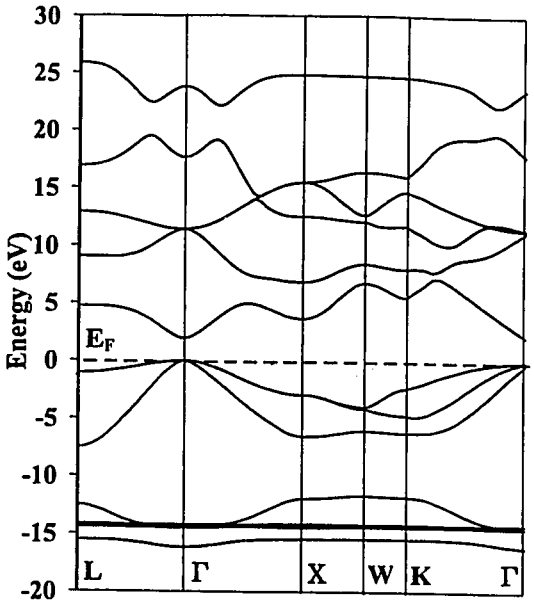

Figure 1. Band structure of ideal c-GaN, as predicted by the LMTO-ASA technique using empty spheres and treating Ga 3*d* states as valence.

Table I. Comparison of gap widths obtained for ideal c-GaN by present and earlier LMTO calculations.

Gap Widths	Present Work	Other Works
Γ_v - Γ_c	1.94	2.23,[a] 2.01,[b] 1.89[c]
Γ_v - L_c	4.73	4.99,[a] 4.81,[b] 4.67[c]
Γ_v - X_c	3.68	3.36,[a] 3.34,[b] 3.23[c]

[a] LMTO-ASA, Ref. 17

[b] Citation in Ref. 17 to unpublished LMTO calculations performed by W.R. Lambrecht and B. Segall. Values in parentheses include a band-gap correction based on the use of an external potential.

c PWPP, Ref. 34.

Figure 2 shows the total DOS and projections of the DOS over the orbital basis of each atom. Here the valence band is seen to be composed primarily of the usual 2*p* states of N, with much smaller contributions arising from 4*p* orbitals throughout the valence band, and with significant admixtures of Ga 4*s* appearing at the bottom of the valence band. Ga 4*s* and 4*p* and N 2*p* orbitals hybridize strongly to form the CB edge, with a small contribution being made also by N 2*s* orbitals.

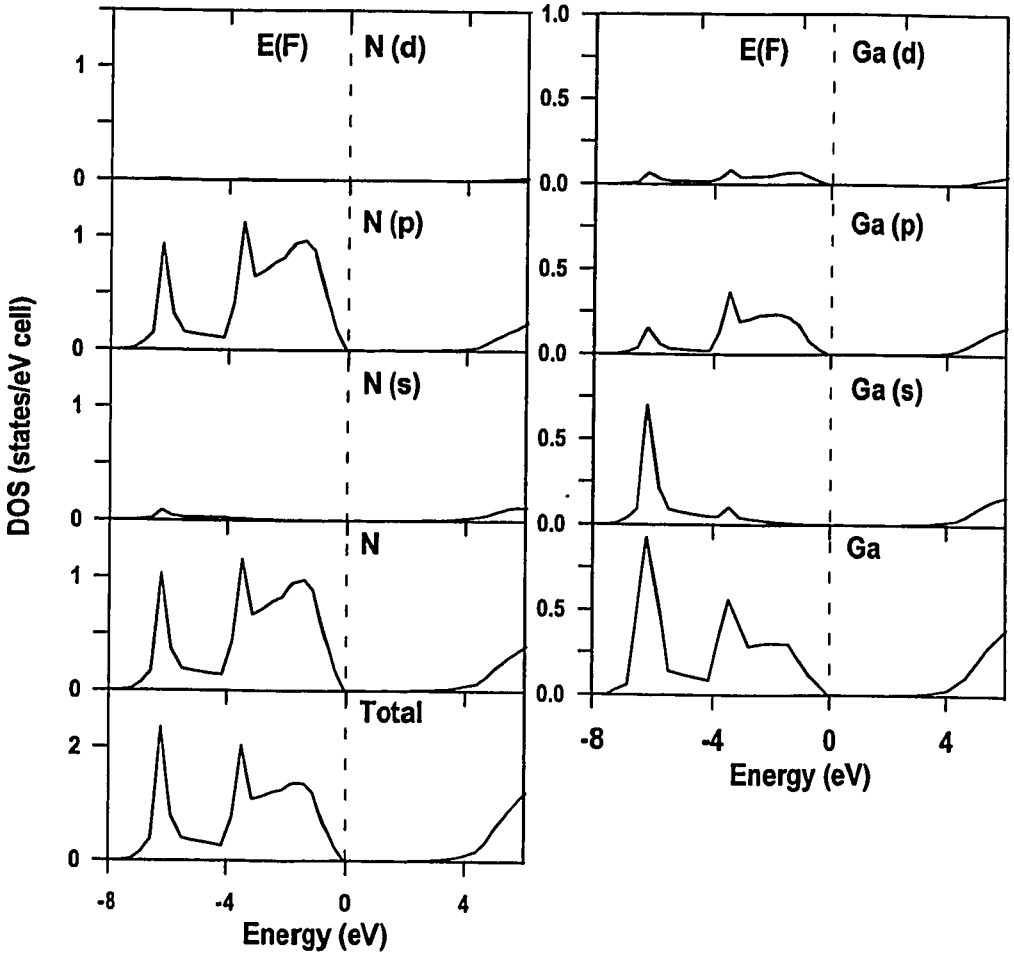

Figure 2. Total and orbital-projected DOS predicted by LMTO-ASA calculations.

Figure 3 shows the charge distribution predicted in the (110) plane of ideal c-GaN. Here is evident the high ionicity exhibited by GaN, the highest of all the material systems considered in the scope of this study. This ionicity is reflected in the distribution of charges among the muffin-tin orbitals, with the Ga atoms being stripped of 1.15 charges relative to their normal complement as free atoms. In the self-consistent representation of the ideal crystal, most of the charges removed from the Ga atoms are represented by the orbital basis of the empty interstitial muffin-tin orbital spheres, rather than by the basis of the neighboring N atoms themselves. Of the charge removed from the Ga atoms, there is a net accumulation of only about 0.11 charges on the N atoms, with the remainder being evenly divided between the two types of empty spheres that were used in the model. While the simpler atomic orbital configuration of Al atoms and the slightly lower ionicity of AlN permitted the relaxation of the c-AlN lattice to be studied using simpler no-empty-sphere LMTO model, such treatment is not at all possible for the GaN system.

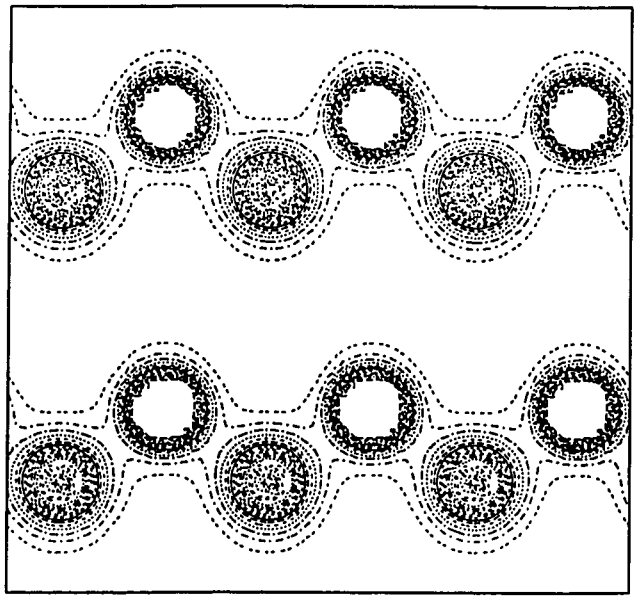

Figure 3. Predicted distribution of charges in the (110) plane of ideal c-GaN.

C. Vacancies in c-GaN

Vacancy-supercell calculations were performed for both anion and cation vacancies in c-GaN, but without the relaxing the coordinates of the nearest atomic neighbors. As before, the potential and wavefunctions in the vacancy region were represented by linear combinations of energy-independent orbital basis functions within a muffin-tin sphere.

The total and partial densities of states for the N-vacancy supercell are shown in Figure 4. As was true for the other vacancies considered to this point, the c-GaN N vacancy introduces a pair of resonances to the CB edge, and localized to the first two atomic shells surrounding the vacancy. A similar perturbation is evident at the VB edge. Like the conduction-band resonances, the perturbations to the VB edge are localized to the vacancy and to the two nearest atomic shells.

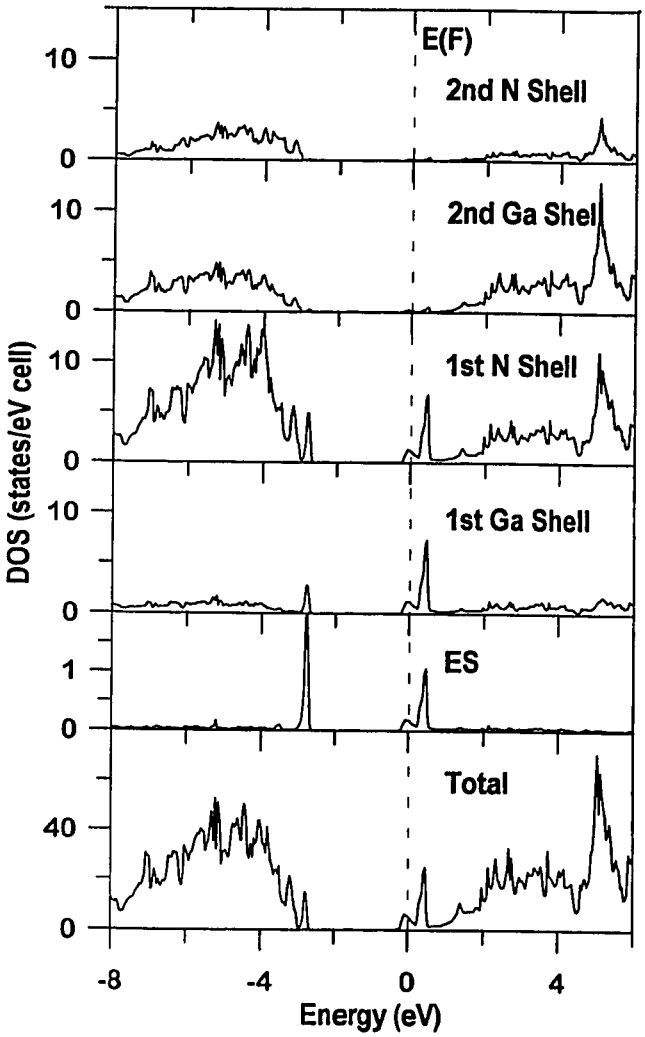

Figure 4. Total and shell-projected DOS for N-vacancy c-GaN supercell.

In Figure 5, the total DOS have been aligned at the bottom of the valence band, where the vacancy is expected to have little or no affect upon the band structure of the host lattice. Here it is clearer than in Figure 4 that the new features have not been added to the band gap, but in fact have been superimposed onto low-lying band of already existing states in the host-lattice band structure. Numerically, the band gap of the N-vacancy supercell is identical to that of the host lattice.

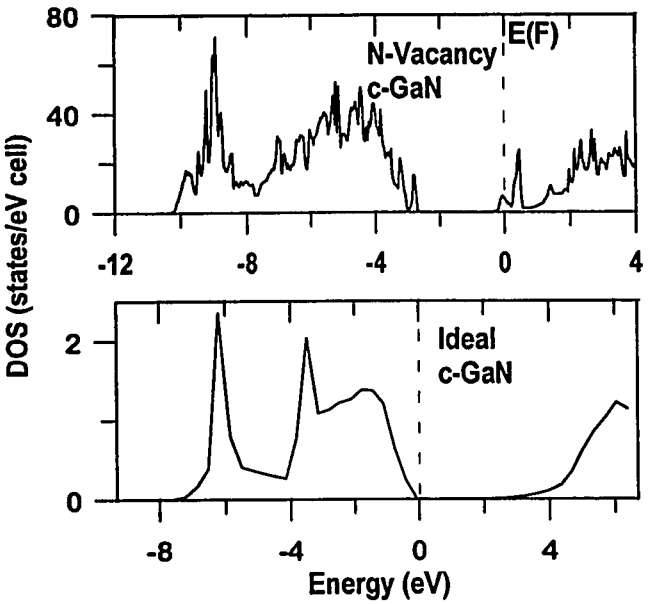

Figure 5. Total DOS for ideal c-GaN (lower panel) and for the N-vacancy supercell, each aligned with the other at the bottom of the valence band. The resonances introduced at the band edges do not reduce the band gap.

The orbital decomposition of the DOS over the vacancy site and the first two atomic shells is shown in Figure 6. Here an unusual pattern emerges, as compared with the behavior of the anion vacancies considered previously. Here the portion of the conduction-band resonances associated with the vacancy have a *p*-type orbital symmetry, while the vacancy contribution to the valence band has *s*-type symmetry. This is in contrast to the pattern exhibited by the c-BN anion vacancy discussed previously. In that

case, the only significant wavefunction component associated with the vacancy site itself appeared at the CB edge, had an *s*-type symmetry, and was localized to the region below the Fermi level. The orbital composition of the anion and cation components of the CB-edge states, which contribute much more to the total DOS in this energy range, is not inconsistent with the results obtained previously for c-BN. Again however, the shape and position of the band-edge states is rather different than was seen in the earlier calculations for c-BN. Given these observations, and given the fact that a large outward relaxation was predicted for the anion vacancy calculation in the c-BN, it seems justified to speculate that the resonance at the CB edge of c-GaN might relax below the Fermi level as the neighboring atoms are permitted to adjust their lattice positions and electronic configurations in response to the N vacancy. The band-edge vacancy state might be expected to have a mixed orbital character, though the symmetry of the vacancy component of the wavefunction could be expected to assume an *s*-type character. These tendencies, which are based on the observations made for c-BN, may be somewhat more muted however in c-GaN, where outward relaxation of Ga_I atoms is likely to be somewhat restrained by simple virtue of their much larger "size," as compared with the B atoms that fill the cation sublattice of c-BN.

The distribution of charges predicted for the neighborhood of the c-GaN N vacancy is shown in Figure 7. Here the total charge-density distribution essentially reflects the unperturbed crystal configuration, while the distribution of charges near the band edges

exhibits the complex symmetry suggested by the DOS projections for the vacancy site and the first two coordinational shells.

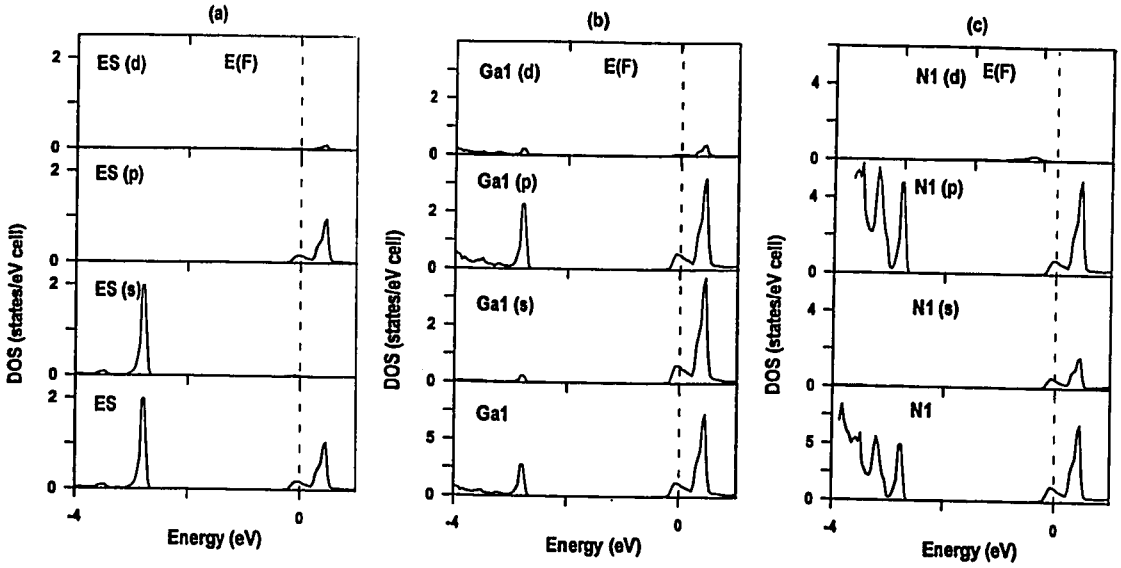

Figure 6. DOS projections over the orbital basis of the vacancy and the atoms in the atomic shells nearest the vacancy in the N-vacancy supercell of c-GaN.

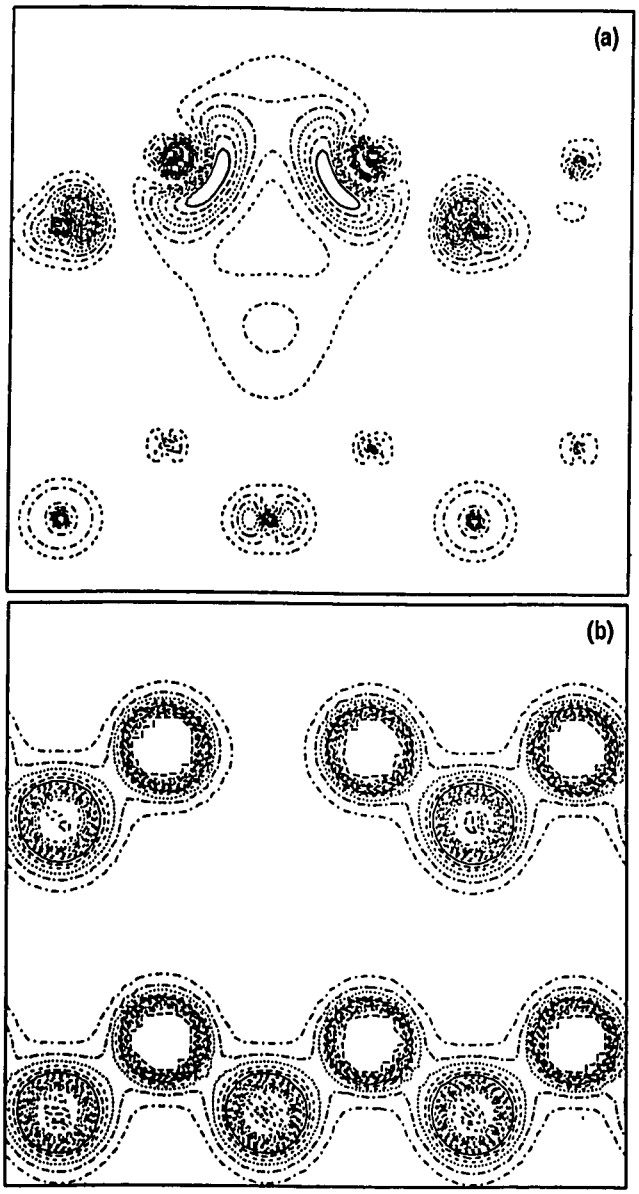

Figure 7. Charge-density distribution in the unrelaxed c-GaN N-vacancy supercell. (a) Distribution of CB charges. (b) Total charge-density distribution.

The total and shell-projected DOS for the Ga-vacancy in the c-GaN supercell are shown in Figure 8. Here a more familiar pattern emerges, with a narrow, intense vacancy peak being formed at the VB edge. The vacancy band here is localized to the vacancy site and to the adjacent shell of N atoms, suggesting that carriers associated with such a vacancy would have poor characteristic mobility. The Fermi-level DOS of 36 states/(eV-cell) is comparable to the 48 states/(eV-cell) predicted for the c-BN N-vacancy supercell It should be noted however that small shifts in the Fermi level associated with lattice relaxation could significantly change this result to either greater or smaller values. More fundamentally, it should be noted however that the existence and stability of such vacancies has yet to be established.

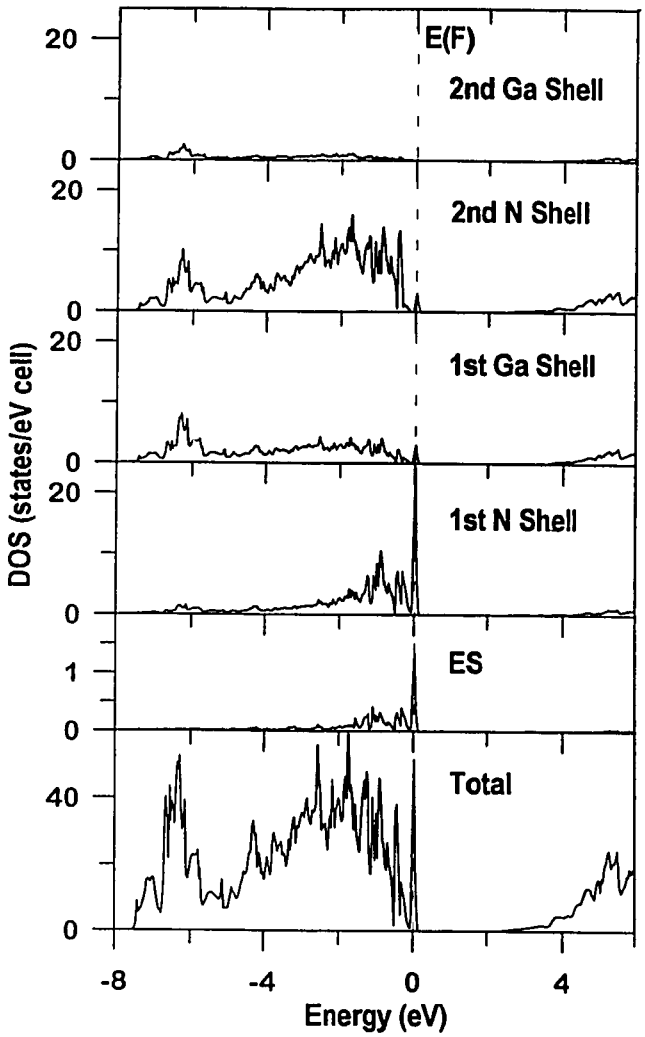

Figure 8. Total and shell-projected DOS for the Ga-vacancy c-GaN supercell.

The orbital composition of the VB-edge vacancy resonance is shown in Figure 9. Here the pattern is very similar to that observed for the B vacancy in c-BN, with the exception of a significant *d*-type orbital component being associated with the vacancy in this instance. This *d*-orbital component is certainly not connected in any direct manner with the highly localized *d*-type orbitals of the Ga_I shell. Though such symmetry was not observed in the case of the B-vacancy calculation, there is a small *d*-orbital component normally associated with the cation sites in ideal c-GaN. This component is relatively small however, and as in the case of the N vacancy considered above, these observations tempt the speculation that the *d*-type symmetry seen here will largely evaporate upon relaxation of the surrounding lattice.

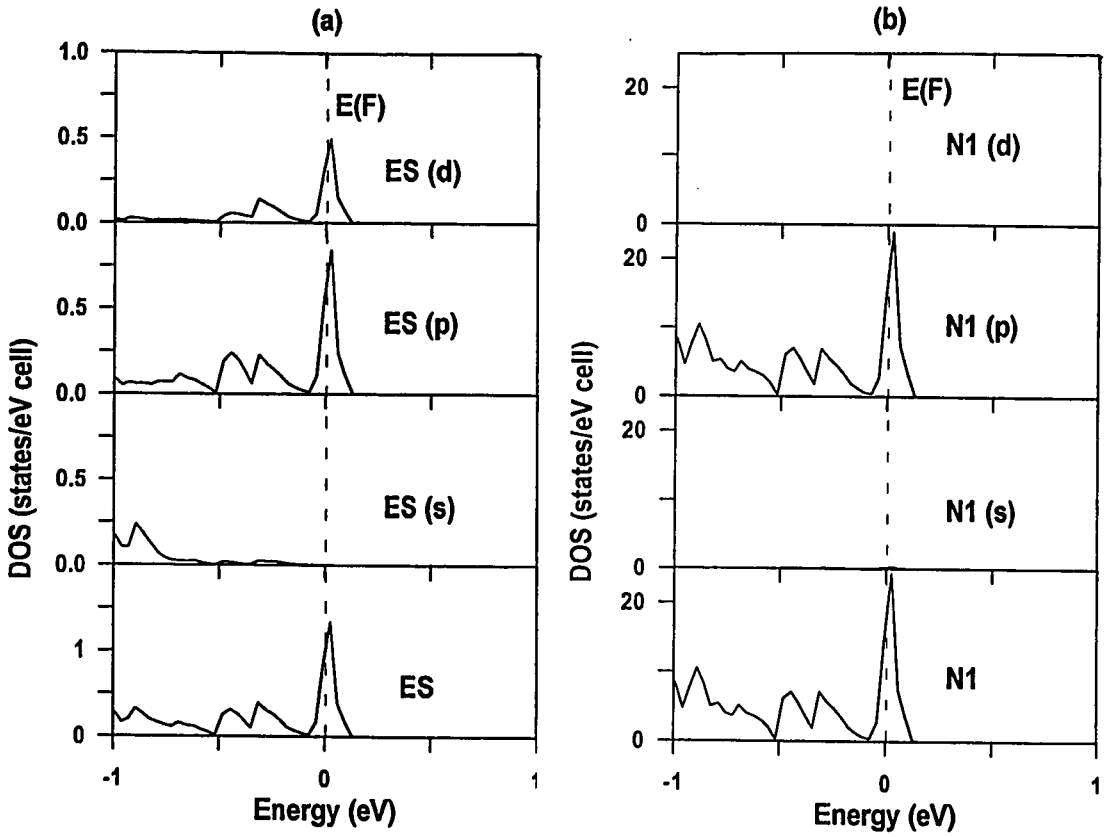

Figure 9. Orbital projections of the DOS components associated with (a) the vacancy site, and (b) the neighboring shell of N atoms.

As was true of the DOS and the DOS projections shown above, the charge-density distributions for the N-vacancy supercell show strong similarities to those obtained for the corresponding c-BN supercell. Because of the lack of lattice relaxation, the total charge-density distribution shown in Figure 10 essentially reflects the distribution of charges in the ideal crystal. The distribution of charges in the vacancy band, however, clearly shows the *p*-type symmetry of the bonding between the neighboring N atoms and the vacancy site, consistent with the DOS projections of Figure 9.

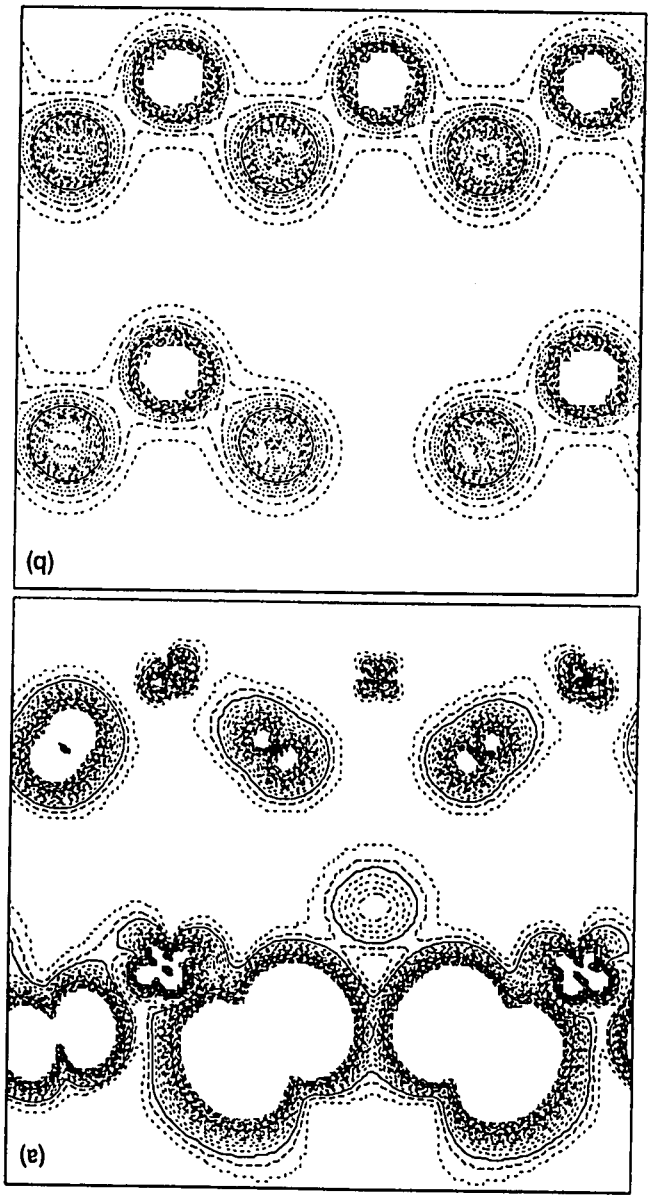

Figure 10. Distribution of charges near the Ga vacancy in a c-GaN supercell. (a) Distribution of charges in the vacancy band at the VB edge. (b) Total charge distribution.

D. Substitutional impurities in c-GaN

Figure 11 shows the total and shell-projected DOS corresponding to a c-GaN supercell in which an O atom has been substituted to the anion sublattice, producing an *n*-type offset in the Fermi level. While the band gap is essentially unchanged in comparison with that of the ideal crystal, the Fermi level has been raised to a level nearly 1 eV above the CB edge. With a large number of occupied states in the conduction band, and 3.2 states/(eV-cell) at the Fermi level O impurities substituted to the anion sublattice clearly exhibit high efficiency for the creation of *n*-type carriers in c-GaN. Approximately half of these carriers are associated with the first shell of N atoms, while the rest are localized in approximately equal proportions to the O impurity and to the neighboring shell of Ga atoms.

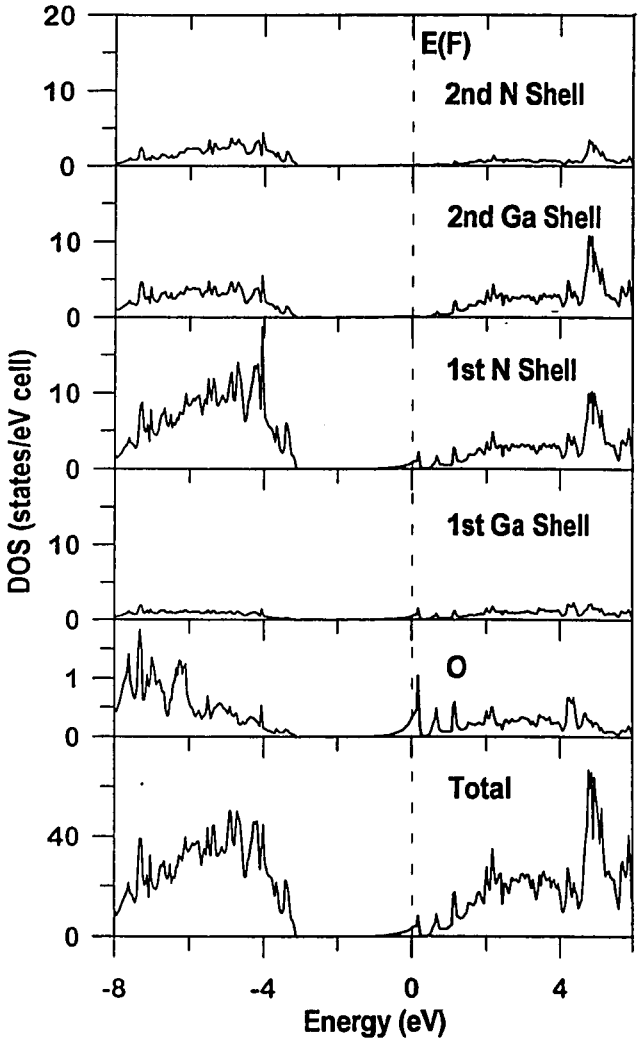

Figure 11. Total and shell-projected DOS for c-GaN supercell with an O atom substituted to the anion sublattice.

The valence configuration of a free O atom has four $2p$-orbital electrons outside two completely filled s shells. Given that the p shell is only partially filled, it might be reasonable to expect the acceptor levels associated with the O atom to assume a p-type symmetry. The DOS projection over the O orbital components near the CB edge, shown in Figure 12, indicate however that these states are associated with the $2s$ orbital rather than with the partially filled $2p$ shell. While the symmetry of an anion site in ideal c-GaN includes both $2s$ and $2p$ orbitals, roughly two thirds of this mixing is associated with p-type orbitals. The Ga_I band-edge structure seen here is a hybrid of approximately equal

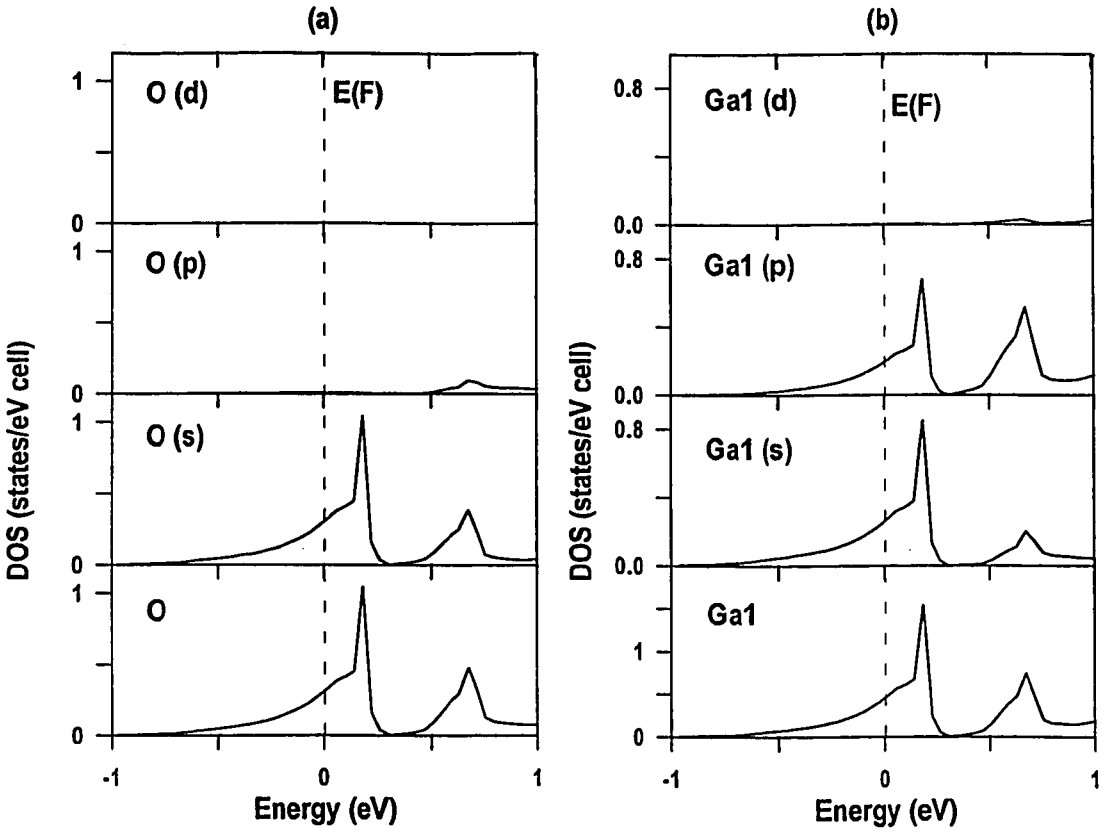

Figure 12. DOS projections over the orbital basis of (a) the O impurity, and (b) the shell of neighboring Ga atoms in c-GaN.

components of 4*s* and 4*p* orbital components, while the N_I orbital component of the DOS consists entirely of *p*-type orbitals, and is not shown in the DOS projections.

The O atom is far more ionic than the indigenous N atoms of the host lattice, accumulating a nearly 0.3 charges more than would be found on an isolated ground-state atom. This compares with the ~0.1 net charges accumulated on the N atoms in both the ideal lattice configuration and in the O-impurity supercell. This excess charge is taken entirely from the neighboring Ga atoms and from the charges normally associated with the empty interstitial spheres. The ionicity of the O bonding and the orbital composition of the CB edge states is shown very clearly in Figure 13. Particularly

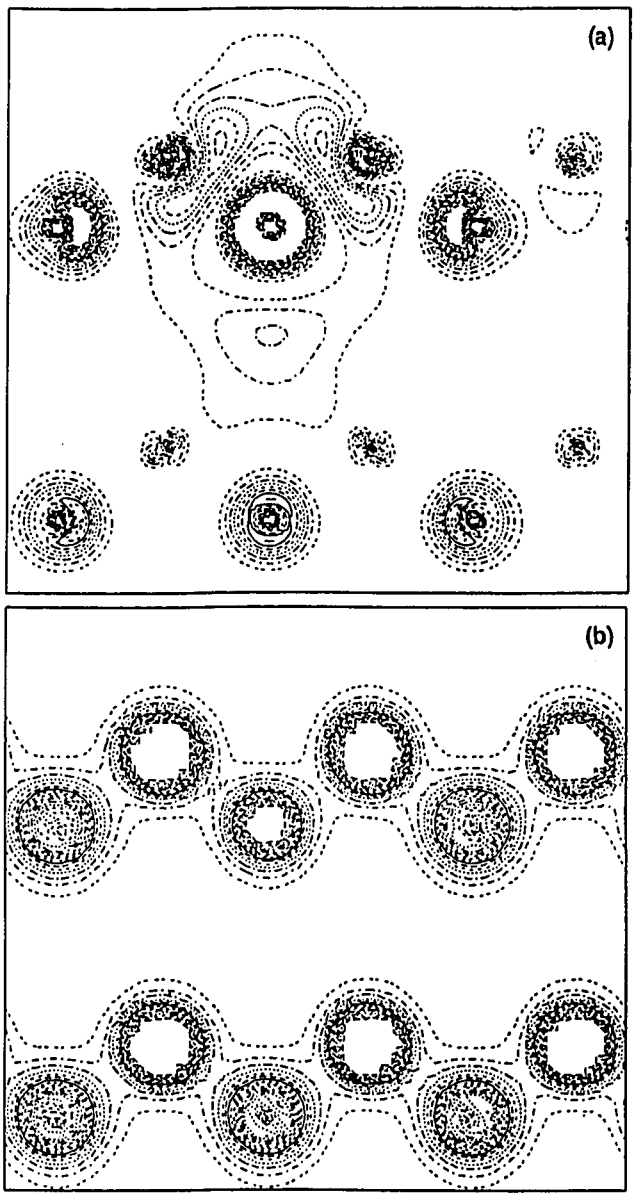

Figure 13. Distribution of charges in the (110) plane of a c-GaN supercell with an O atom substituted to the anion sublattice. (a) CB-edge distribution of charges. (b) Total charge-density distribution.

pronounced are the 2*s* orbital electrons associated with the O impurity, while the mixed symmetry of the Ga atoms and the 2*p* composition of the band-edge N_1 states are also quite evident.

The last two c-GaN impurities to be studied were Zn and Cd acceptor impurities substituted to the cation sublattice. The total and shell-projected DOS for the Zn-impurity supercell is shown in Figure 14. A 0.3-eV-wide acceptor band is introduced at the VB edge. The 3*d* valence electrons of the Zn impurity itself contribute strongly in the lower portion of the valence band, where they mix mainly with N 2*p* and, to a lesser extent, with the Ga 4*s* and 4*p* states of the host lattice.

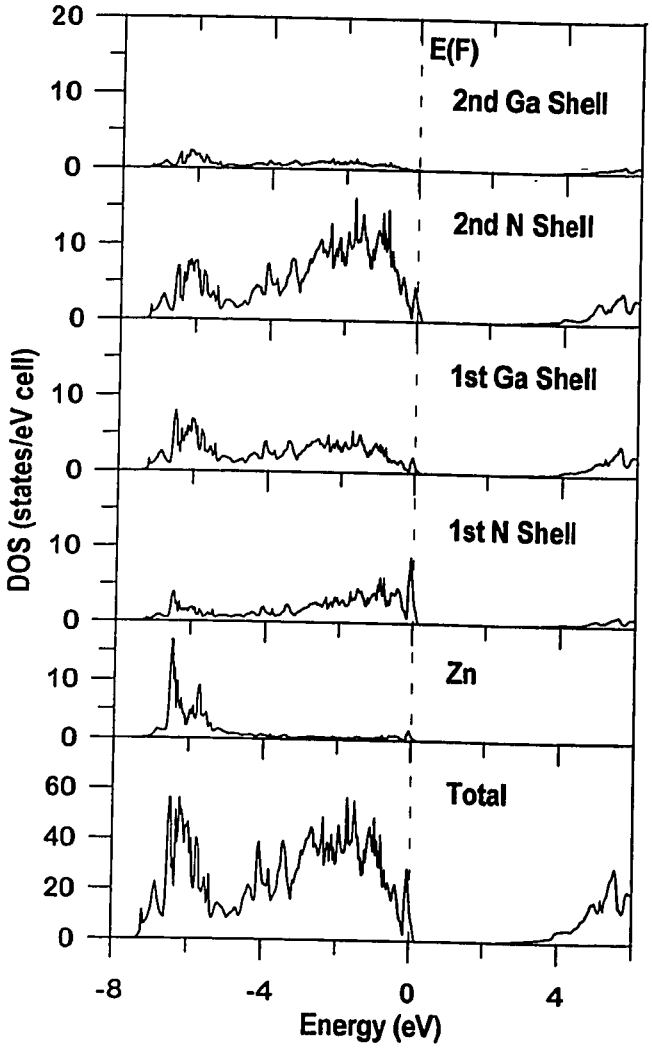

Figure 14. Total and shell-projected DOS for Zn-impurity c-GaN supercell.

The projection of the band-edge acceptor level over all coordinational spheres shown in

Figure 15 shows that these states are highly delocalized over the surrounding anion sublattice of the c-GaN host crystal. A relatively small, but non-negligible fraction of the band-edge DOS is associated with the Zn impurity itself. The still appreciable density of levels that appears at the fourth N sphere shows that at the density of Zn impurities represented in the supercell model, impurity centers are not completely isolated from one another. Because of this, it should be borne in mind when interpreting the simulation results that some details of the impurity calculations presented here for Zn may not persist at lower doping levels where the interactions between impurity centers will be smaller.

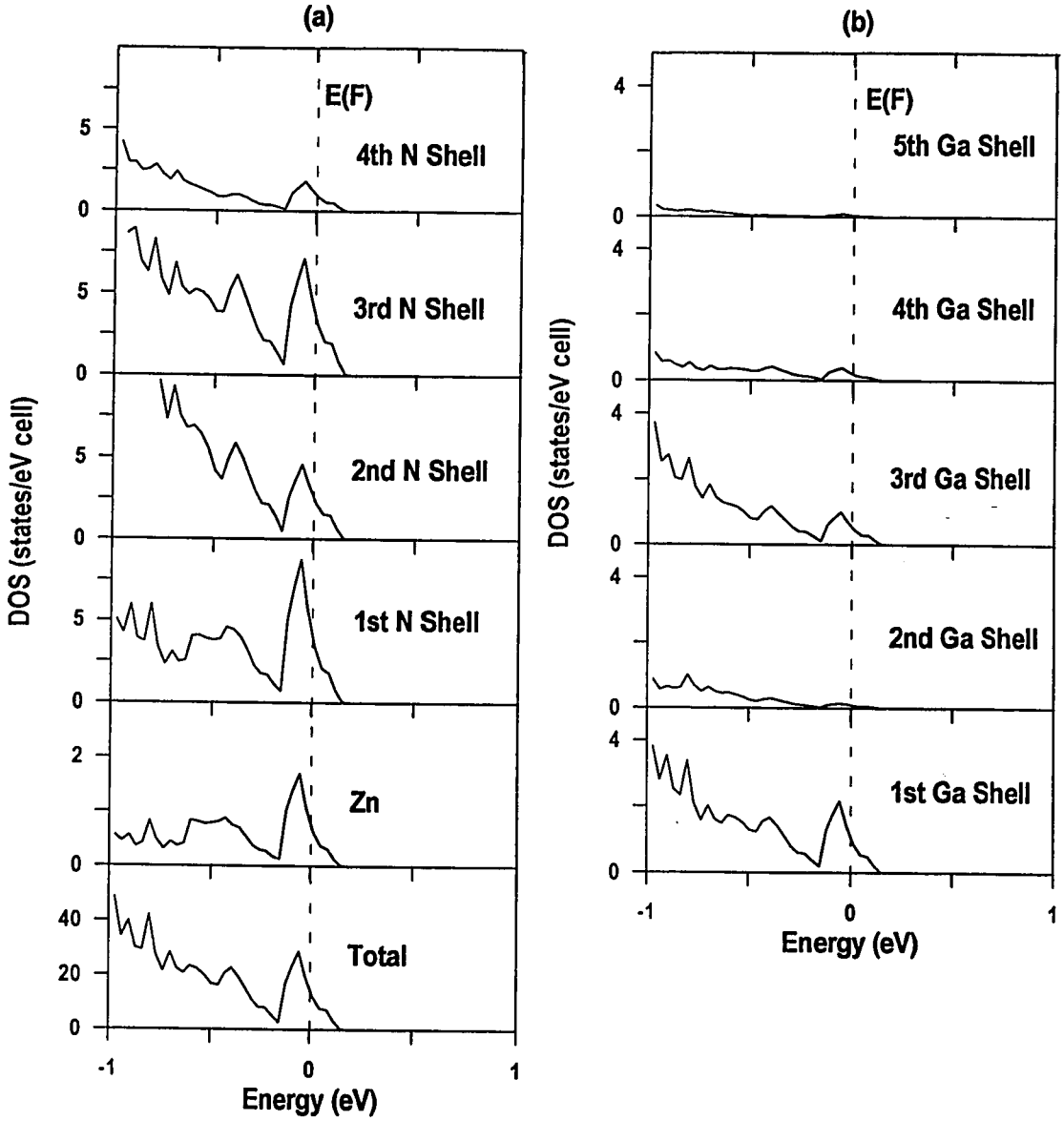

Figure 15. Acceptor-band DOS for Zn-impurity c-GaN supercell.

The valence configuration of the Zn impurity consists of a filled 3*d* electron shell and a filled 4*s* shell, with the 4*p* shell remaining vacant. The Ga atom replaced by the Zn impurity has the same electronic configuration, but with one electron occupying the 4*p*

orbital. Given this situation, it is reasonable to expect that the acceptor states associated with the Zn impurity would tend to assume a Ga-like orbital configuration. Indeed this is a good approximation to the situation that is revealed both in the DOS orbital projections shown in Figure 16, and in the distribution of charges over the different atomic shells represented in the supercell model. The orbital projection of the DOS shows the Zn-associated portion of the VB-edge acceptor level to be composed of both $4p$ and $3d$ states.

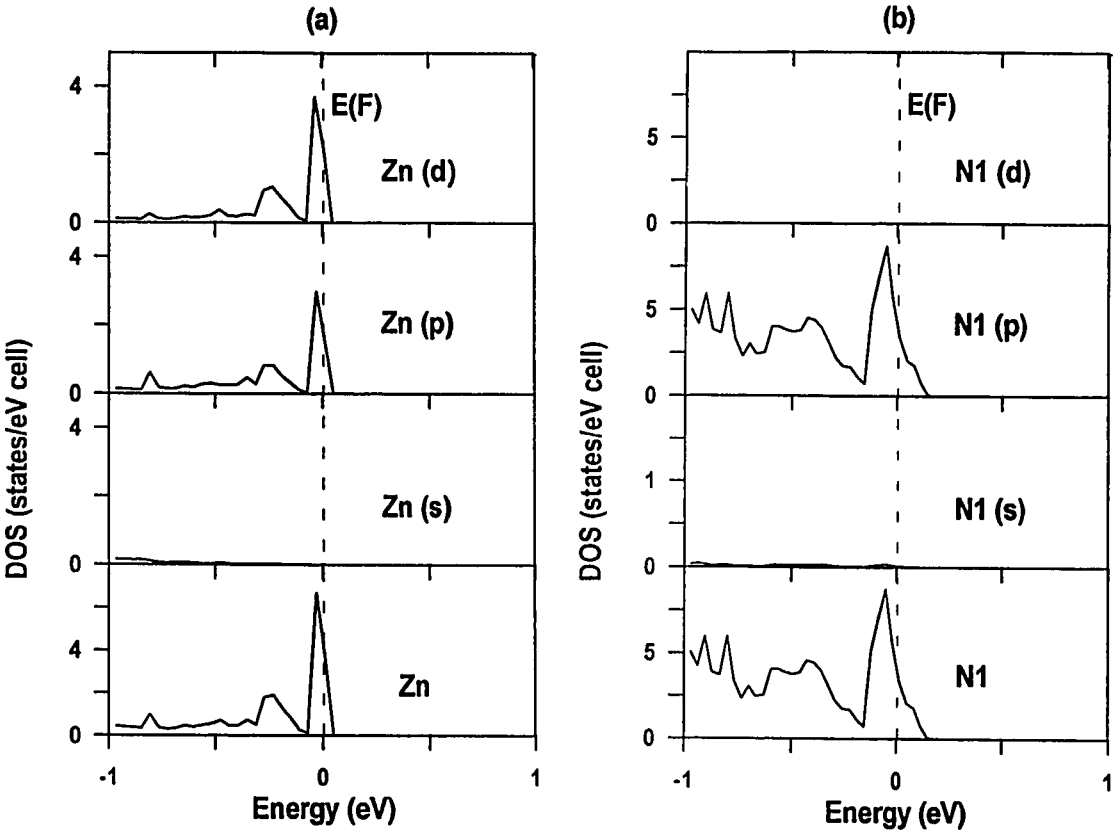

Figure 16. Orbital projections of the DOS over (a) the Zn impurity, and (b) N1 atomic shell in a c-GaN supercell.

The tabulation of charges in the simulation output for the final self-consistent configuration shows that while the neighboring N atoms accumulate charge from the Zn impurity in much the same way as they do from Ga atoms in the ideal crystal, this effect is reduced for the Zn impurity. This can be attributed to the one-electron deficiency in the valence configuration of the Zn impurity relative to the normal complement of electrons for cation sites in the ideal crystal. As a result, there remain ~0.3 net charges more on the Zn impurity relative to its isolated ground-state configuration than are ordinarily present on the Ga atoms in the ideal crystal. While the Zn impurity and neighboring N atoms experience a reduced transfer of charges as compared with the ideal crystal, the N atoms outside the shell adjacent to the impurity site experience a slightly reduced accumulation as compared with the ideal crystal. The net charge accumulation on the N atoms outside the N_1 sphere is reduced from 0.1 to 0.09, with the difference being compensated by the reduced deficiency of charges at the Zn-impurity position of the cation sublattice.

Figure 17 shows the distribution of charges predicted in the (110) plane surrounding the Zn impurity in c-GaN. As was suggested by the DOS orbital projections, the band-edge states of the Zn impurity are seen to have a mixed *p*- and *d*-type symmetry, while the neighboring N atoms are essentially pure $2p$ orbitals. The total charge-density distribution shows that the Zn impurity is easily accommodated within the host lattice, and is virtually indistinguishable from the native Ga cations.

The density of states predicted by these simulation results is again susceptible to small shifts in the Fermi level that may result from any of a number of normal inaccuracies associated with the approximations that have been made in formulating the model. Despite the marked delocalization of the acceptor levels associated with the Zn-impurity acceptor band, the narrow width of the band predicted by this simulation suggests that these carriers may nevertheless have only moderate characteristic mobility. Given the similarity in the valence-electron configuration and the size of the Zn atom to the cation it replaces, such insulation of the bulk crystal from either electronic or bonding perturbations is reasonable.

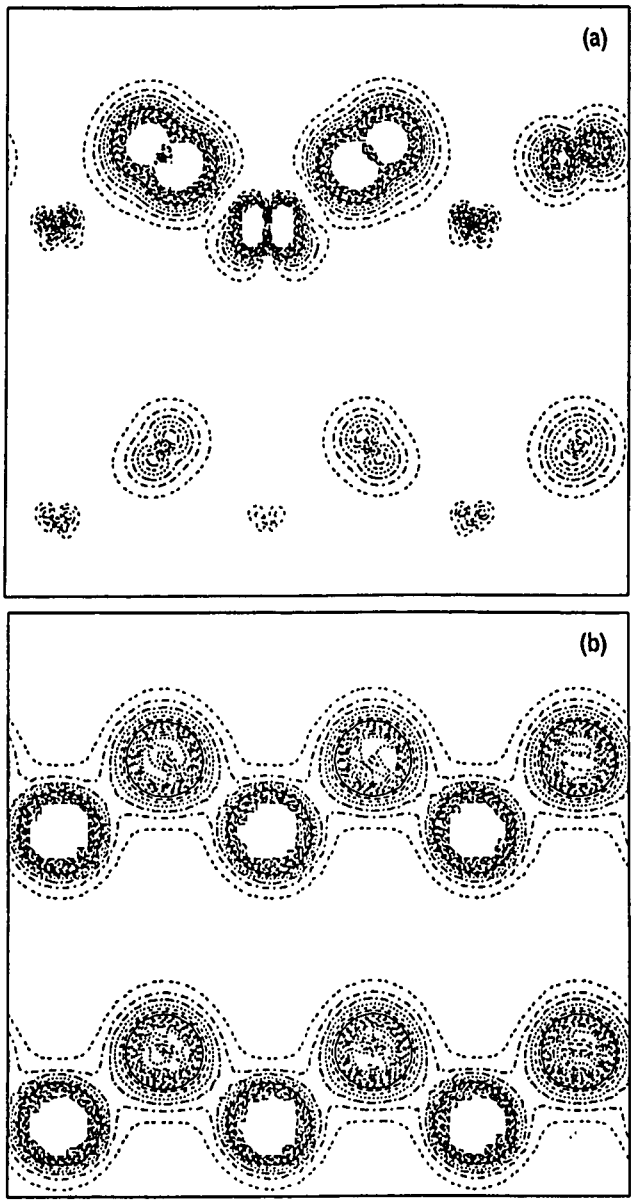

Figure 17. Distribution of charges in the (110) plane of Zn-impurity c-GaN supercell. (a) Distribution of charges in the valence impurity band. (b) Total charge distribution.

Like the Zn impurity, the valence configuration of the Cd impurity consists of a filled *s*-type shell and a filled *d*-type shell, having a completely unoccupied 5*p* valence shell. While the large size of the Cd impurity as compared with that of the Ga cation it replaces is likely to cause more extensive relaxation and perturbations to the bonding and electronic structure, many aspects of the behavior of the Cd-impurity supercell are likely to be similar to those observed for the corresponding Zn impurity.

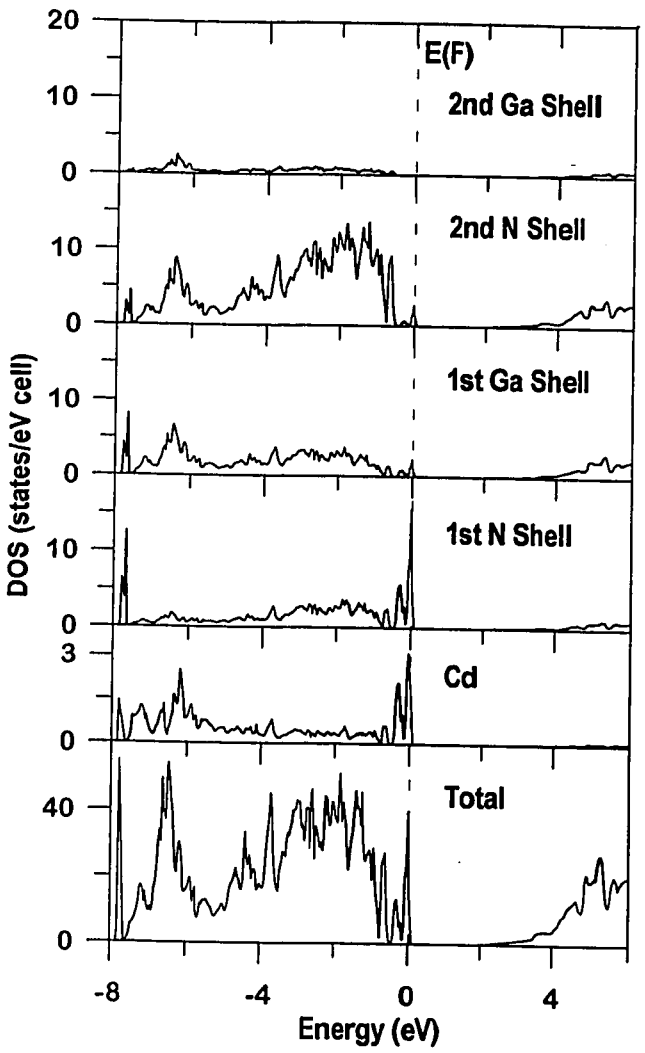

Figure 18. Total and shell-projected DOS for the Cd-impurity c-GaN supercell.

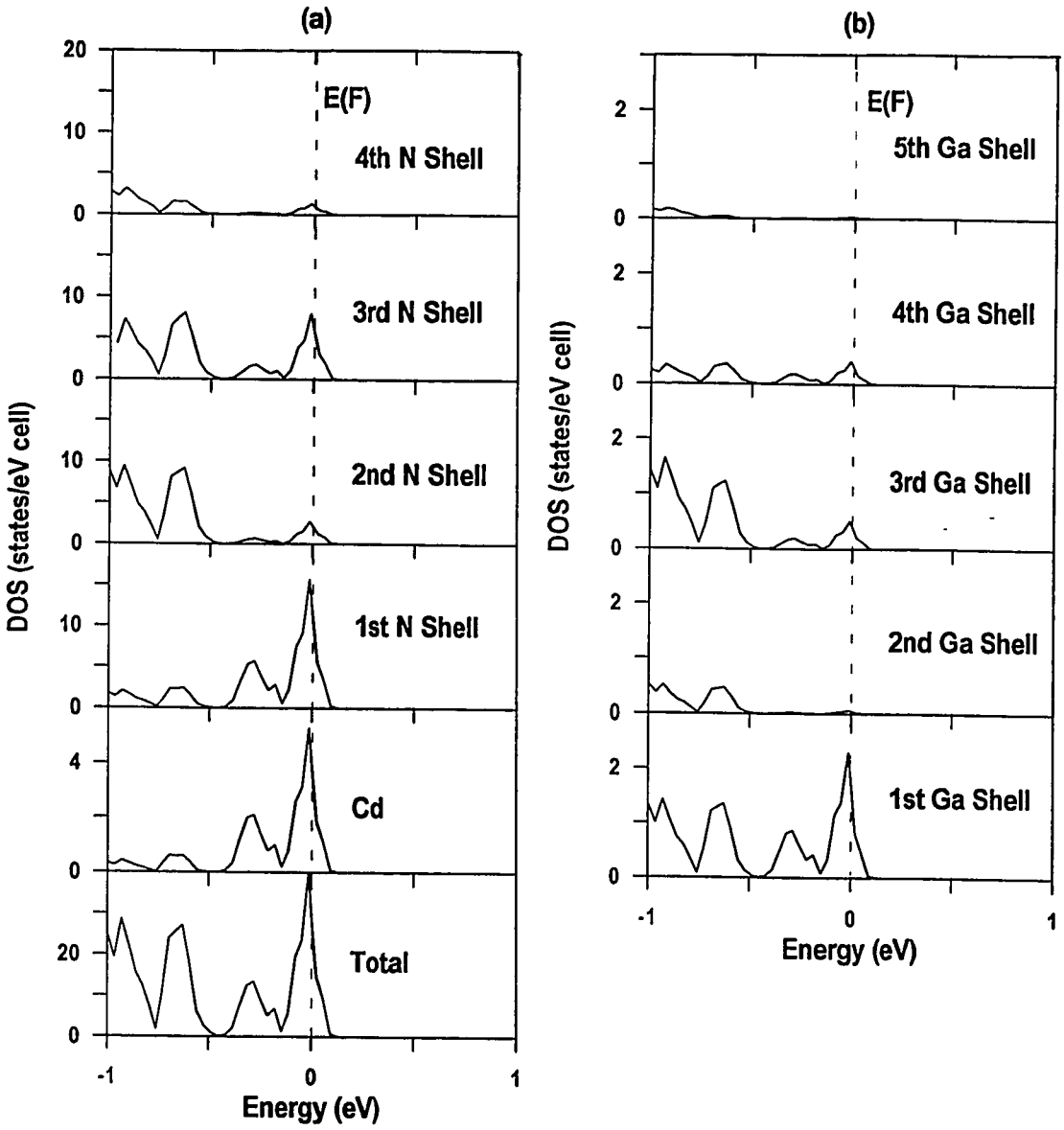

Figure 19. Projection of Cd-impurity acceptor band over anion and cation atomic shells.

This is indeed the case, as is evident upon comparison of Figure 14 with the total and shell-projected densities of states for the Cd impurity shown in Figure 18. Two rather narrow acceptor levels are introduced by the Cd impurity at the VB edge. Although the 2*p* orbitals of the anion sublattice continue as the main constituent of the acceptor level, Figure 19 shows the acceptor levels to be somewhat more localized in the Cd-impurity

supercell. This localization and the narrow 0.24-eV width of the primary impurity band suggests that the Cd-impurity *p*-type carriers are likely to exhibit lower characteristic mobility than the corresponding Zn-impurity carriers. As for the Zn impurity, the density of *p*-type carriers should be effectively controlled by adjusting the density of Cd impurities.

The orbital projection of the Cd-impurity acceptor levels is shown in Figure 20. Again there is a strong similarity between the behavior of the Zn impurity and that of the Cd impurity. The significant difference between the two is the preponderance of Cd 4*d* states in the acceptor band in this instance. It is possible that relaxation of the atomic coordinates and charge configuration near the impurity site may alter this hybridization to a more equitable mix between 5*p* and 4*d* orbitals, more closely approximating the orbital composition observed for the Zn-impurity supercell.

The acceptor-band charge-density distributions shown in Figure 21 again reflect the localization and symmetry of the band-edge states suggested by the DOS projections. The total charge-density distribution, shown in the lower panel of the figure shows the larger "size" of the Cd impurity, as compared with that of the Ga atom for which it is substituted. Because of the size difference between the Cd atom and the Ga atom it replaces, appreciable relaxation is likely to occur in the neighborhood of the Cd impurity, and this may substantially alter some details of the conclusions that have been derived

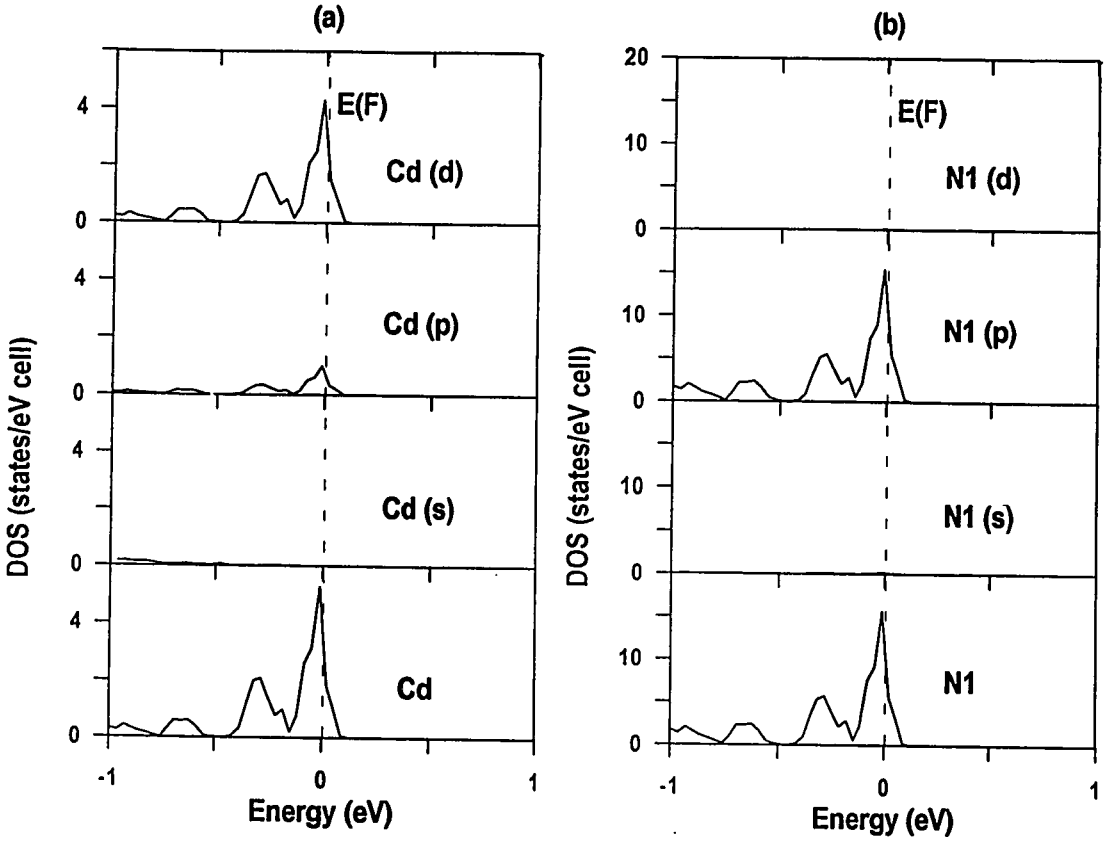

Figure 20. Orbital projections of the Cd-impurity acceptor bands introduced at the VB edge of c-GaN. (a) Orbital projection of Cd impurity states. (b) Orbital projection of states associated with the neighboring shell of N atoms.

from this calculation. The consistency of these results with those obtained for the Zn impurity (which will certainly cause smaller relaxation to the surrounding host lattice) however is reassuring that the conclusions drawn for the Cd impurity are essentially sound.

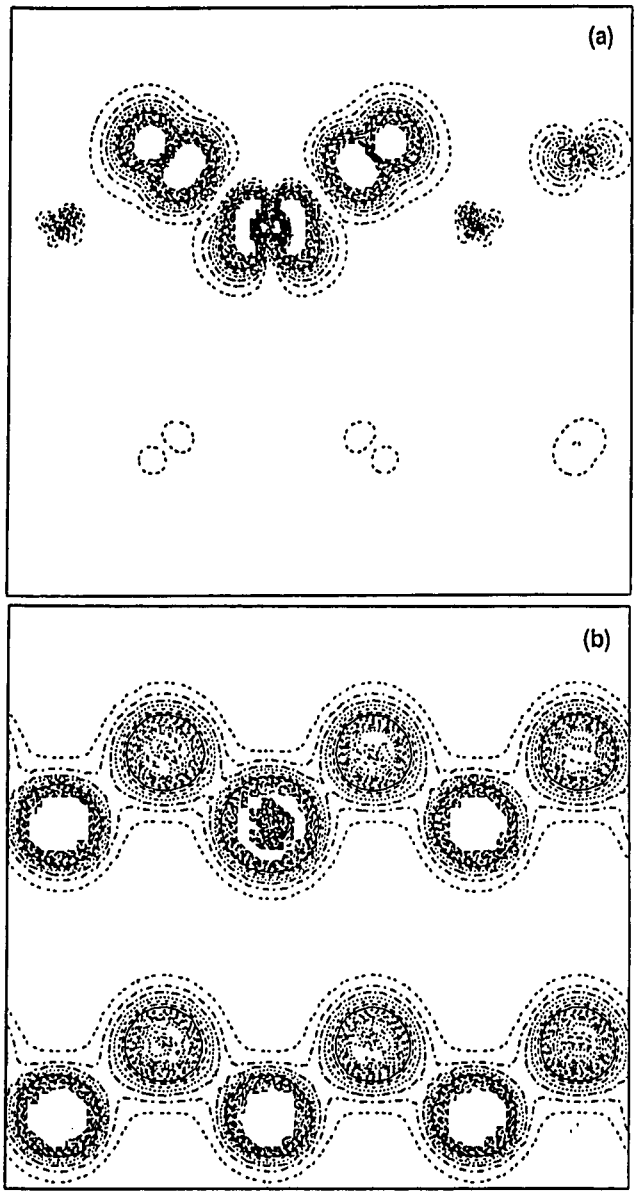

Figure 21. Distribution of charges in the (110) plane passing through the site of a Cd impurity substituted to the Ga sublattice of c-GaN. (a) Distribution of charges within the acceptor band. (b) Total charge-density distribution.

E. Summary of results and conclusions for c-GaN vacancy and impurity supercell calculations

The large number of valence electrons, the important role of Ga-3*d* semi-core electrons and their mixing with N 2*s* states, combined with the high ionicity of bonding in c-GaN each contributed to the requirement for a much more complicated description of c-GaN supercells than were required for either c-BN or c-AlN calculations. While the vacancy and impurity supercells included 64 atomic sites, it was also necessary to include 64 empty spheres to obtain good agreement of self-consistent calculations with independent calculations for ideal c-GaN. The increased complexity of the supercell model and the increased demand upon computational resources made radial relaxation of vacancy and impurity nearest neighbors prohibitive. By comparing the results with those obtained for c-BN, an attempt was made to judge the likely significance of such relaxation.

Both anion and cation vacancies were considered. In each case, the impurity bands were strongly localized to the coordinational spheres nearest the impurity site. In the case of the anion vacancy, the predicted orbital symmetry of the CB resonance was different than that predicted previously for such vacancies in c-BN. It was noted however that such vacancies in c-BN were accompanied by a large outward relaxation of neighboring cations. While it was suggested that the larger size of Ga atoms was likely to limit such outward relaxation in c-GaN, the speculation was tentatively advanced that the differences in orbital symmetry between the two materials may disappear after properly accounting for relaxation effects. By contrast, the predictions for the cation vacancy

supercells were very consistent with those predicted for the B vacancy in c-BN. Though the existence and stability of such vacancies has yet to be demonstrated, the calculations suggest a high DOS at the Fermi level in the partially occupied VB resonance introduced by the vacancy, consistent with the results obtained with the corresponding c-BN supercell.

Because of its important role as an unintentional impurity, O was considered in addition to Zn and Cd in the c-GaN impurity supercell calculations. The O-impurity supercell calculations were consistent with empirical observactions[6] that O can be an efficient *n*-type impurity in GaN. The CB states associated with this anion substitution are predicted to be *highly* localized to the impurity itself and to the neighboring shell of Ga atoms. This localization is physically consistent with the higher ionicity of O as compared with the N atom it replaces.

The main *direct* contribution of the Zn impurity was predicted to occur near the bottom of the valence band. The narrow acceptor levels near the VB edge were highly delocalized over the anion sublattice surrounding the impurity site, while the cation sublattice was little perturbed from that of the ideal crystal. The extent of the delocalization was such as to suggest that a larger supercell may be required to fully isolate the electronic structure perturbations associated with single Zn substitutional impurities. As might be expected, the acceptor states associated with the Zn impurity assume a Ga-like orbital

configuration. Based on this result and given the similar sizes of the Zn and Ga atoms, it is not surprising that the electronic structure of the Ga sublattice would be little perturbed from that of the ideal crystal.

Given the similarity of the Zn and Cd valence configurations, the perturbations associated with the Cd impurity supercell were expected to be quite similar to those predicted for Zn substitutions to the cation sublattice. Indeed this result was observed with the introduction of narrow acceptor levels at the VB edge. In this instance however, the impurity levels, which are still associated mainly with the anion sublattice are more localized to the neighborhood of the impurity. While the large size of Cd impurities can be expected to result in possibly significant lattice relaxation, the consistency of the results with those obtained for the Zn calculations suggests that Cd, like Zn may be an effective *p*-type substitutional impurity, though possibly exhibiting lower characteristic carrier mobility.

VI. THIN AlN/BN SUPERLATTICES

A. Introduction

III-V nitrides and their alloys have already been used successfully for the fabrication of light-emitting diodes (LEDs) and laser diodes (LDs).[1-6,30] While these material systems hold important prospects for operation at short wavelengths, they are also of considerable interest because of (a) their potential for use in high-temperature electronic devices, and because (b) their high defect-formation energy is likely to endow working devices with much greater longevity than has been demonstrated for corresponding II-VI material systems.[2,30]

Successfully developing practical devices obviously requires the ability to fabricate high-quality films with both *n*- and *p*-type conductivity, and the ability to tailor the electronic properties via the use of dopants and the control of native defects. Also central to the performance and success of III-V nitride devices has been the fabrication of heterostructures and interfaces, which have typically been used to form the active regions of optical devices. III-V nitride heterostructures also may eventually find additional important uses in high-temperature electronic devices such as HBTs and MODFETs, which be applied in a variety of military, industrial, and space-borne settings subject to extremes of environmental conditions.

Because III-V nitrides have generally large lattice mismatches, thin films are usually grown on foreign substrates, and heterostructures are typically formed either between dissimilar alloys or between similar alloy layers having an abrupt compositional change. Zinc-blende BN, for example, has been grown on Si[35] and diamond[36] substrates, which have 33% and 1.3% misfits to c-BN, respectively, and has also been grown on SiC substrates buffered by a graded alloy of GaN and BN.[37] Successful III-V nitride heterostructure devices, however, have been mainly formed from alloy layers in which the bulk nitride constituents have very similar lattice constants while simultaneously spanning a wide range of band gaps. In particular, heterostructure devices fabricated from alloys of GaN (lattice-constant a=4.50, 3.4-eV band gap), AlN (a=4.37, 6.2-eV band gap), and InN (a=4.98, 2.0-eV band gap) permit the electronic structure and performance characteristics of electronic devices to be varied over a wide range, while minimizing the strain that is intrinsic both within and between alloy layers.

While the previous three chapters dealt with the behavior of impurities and vacancies in bulk III-V nitrides, the present chapter reports the results of an initial investigation into the characteristics of a III-V nitride heterostructure formed from alternating layers of c-AlN and c-BN. Unlike the conventional alloy systems that have been used to date in the construction of III-V nitride heterostructure devices, bulk c-AlN and c-BN have very similar and wide band gaps of 6.2 and 6.4 eV, respectively. And in a similar contrast to

the AlGaN/InGaN heterostructure devices already in commercial production,[1] the bulk constituents of the AlN/BN superlattice have a substantial 20% mismatch between them. While such strain certainly presents challenges to the practical fabrication of such devices, it also opens new degrees of freedom for tailoring of electronic structure. Furthermore, the use of two high-band-gap material layers may extend the range of achievable device performance to higher temperatures and shorter wavelengths than might otherwise be possible.

B. The c-AlN/c-BN superlattice model

The supercell used to represent the AlN/BN superlattice consisted of face-centered cubes of c-AlN and c-BN stacked along the *c*-axis ([001] direction). Each material layer consisted of two face-centered cubic cells, with the complete supercell including a total of 16 atomic planes: 4 Al, 4 B, and 8 N planes. Of these planes, nine are unique. While it is has often been shown possible to obtain accurate results from such calculations with the use of fewer atomic planes (typically in the range from 6 to 14),[38,39] these guidelines apply usually to physical systems that incorporate little or no strain, where it is possible even to neglect relaxation at the interface. Using the larger supercell better ensures that the model will include both bulk-like and well-separated interface regions. Such separation is analogous to the separation between point defects and impurities that was achieved previously by using large supercells in which multiple concentric atomic shells

surrounded each vacancy or impurity site. Here the defect is a planar interface, and neighboring interfaces are separated by intervening layers of atoms in a bulk-like atomic configuration.

Because of the considerable mismatch between the layers of the superlattice structure, it is not possible to ignore the relaxation that occurs at the coherent interface between material layers. Indeed it is exactly this strain and the relaxation of the electronic orbital configurations that is principally responsible for perturbing the electronic structure of this material system relative to that of its bulk constituents. To account for this, at least in the first order, a significant effort was undertaken to use total energy as a guide for relaxing the lattice configuration with respect to three parameters: (a) the lattice constant in the plane of the coherent interface, (b) the lattice constant describing the *c*-axis of the c-BN layer, and (c) the lattice constant describing the *c*-axis of the c-AlN layer. The relaxation performed here was thus analogous to that which was performed previously for radial relaxation of atoms nearest vacancy and substitutional impurity sites in bulk c-BN and c-AlN. Here however, the relaxation was performed over three degrees of freedom, including both relaxation in planes parallel to the coherent interface and Poisson-effect changes to the volume of the simple cubic cells on each side of the interface. Such an approach to strain relaxation has been previously applied for example in the study of thin

zinc-blende GaAs/GaN superlattices, for which the 20% misfit between the bulk constituents is comparable to that between c-BN and c-AlN.[40]

Beyond these deviations from the ideal zinc-blende structure, only one additional change was incorporated to the description of the partially relaxed AlN/BN superlattice, that change relating to the position of the N atoms that form the interface itself. These interface N atoms are located between a plane of Al atoms on one side, and a plane of B atoms on the other. With compressive strain parallel to the interface on the AlN side and tensile strain on the BN side, the *c*-axis spacing between atomic planes is substantially dilated in the AlN layers and contracted in the BN layers. Without further adjustment, the different spacings on each side of the N interface would result in an abrupt and unphysical difference in bond angles between the N atoms and the cations on each side.

To improve the description of the interface, the interface N atoms were adjusted in the [001] dimension to positions collinear between neighboring Al and B cation sites. (See also Figure 8) As expected, this relaxation reduced the total energy of the supercell, reflecting a reduced level of strain at the interface. In a true coherent interface of course, the cations in planes adjacent to the interface N atoms would also relax to minimize torsion of their bonding between interface N atoms and the next-nearest planes of N atoms. This relaxation would be smaller than that of the interface N atoms however, as

would be the relaxation atomic planes even more distant from the interface. As a result, the present model incorporates what are believed to be the important relaxation effects necessary to describe the coherent (001) strained interface between c-AlN and c-BN: (a) a common lattice parameter describing the spacing of atoms in planes parallel to the interface, (b) a *c*-axis parameter describing an "average" Poisson dilation for the c-AlN layers, (c) a *c*-axis parameter describing an average Poisson contraction for the c-BN layers, and (d) an adjustment to the position of interface N atoms to minimize the bonding torsion between them and neighboring cation layers.

Regarding the calculations themselves, it should be noted that empty muffin-tin spheres were *not* used to describe the wavefunctions and potentials in the interstitial volumes between atomic spheres on either side of the interface. As in the previous calculations, the absence of these empty spheres was accommodated by increasing the degree of overlap between adjacent atomic muffin-tin spheres. While the benchmark results of Chapter III suggest that this model is almost certainly a valid for c-BN, such a conclusion is not at all certain for the c-AlN layers. Here it is possible only to offer the qualitative argument that the major effects upon electronic structure and bonding are expected to occur in the valence bands of both materials because of the large strain between the two materials and the necessary rearrangement of the ionic/covalent valence charges to accommodate this strain. Because the no-empty-spheres calculations for c-AlN were

found to yield a good representation of valence electronic structure, there is a reasonable basis for extending this model to the study of the highly strained AlN/BN interface. This is especially true given the reasonable performance of this model obtained in the study of the Mg impurity in the c-AlN supercell that was discussed in Chapter IV.

C. Results of LMTO calculations performed for the AlN/BN superlattice

The results of the total-energy calculations used to estimate the relaxation of the superlattice system are shown in Figure 1. The energy minimization proceeded systematically, first varying the lattice parameter "*a*" in planes parallel to the interface without making any correction for Poisson-related dilation and contraction along the *c* axis. This series of calculations yielded the greatest energy minimization, with the initial minimum of energy being obtained at a value of a = 4.02 Å, as indicated by the curve labeled (a) in the figure. In the next series of calculations, total energy was minimized by varying the *c*-axis spacing of (001) atomic planes first in the c-BN layer, then in the c-AlN layer. During each series of calculations, one lattice parameter was varied the other two remained fixed. After completing one more minimization cycle - first with respect to *a*, then with respect to each of the *c*-axis parameters - the total energy converged as shown in curves (b) through (d), each of which shows the variation in supercell total energy with one free parameter while holding the two other lattice parameters fixed. In the final lattice configuration, total energy was minimized with the transverse lattice parameter a set to a value of 3.86 Å. The *c*-axis parameter of the c-BN layer minimized

total energy at a value of 3.07 Å, and the equilibrium *c*-axis parameter for the c-AlN layer was found to be 5.13 Å.

Comparing these results with the 3.62-Å and 4.37-Å lattice parameters, respectively for c-BN and c-AlN, the *a*-value obtained here is seen to represent a 6.6% biaxial dilation for c-BN in the plane of the interface, and an 11.7% contraction for c-AlN. In the dimension perpendicular to the interface the c-BN contracts 15.2%, while the c-AlN expands 17.4%. The total volume change of the cubic unit cells was -3.6% for the c-BN layer, and -8.5% for the c-AlN layer. To the extent that the bulk modulus provides a crude measure of the bonding "stiffness" of each material, these results are consistent with physical

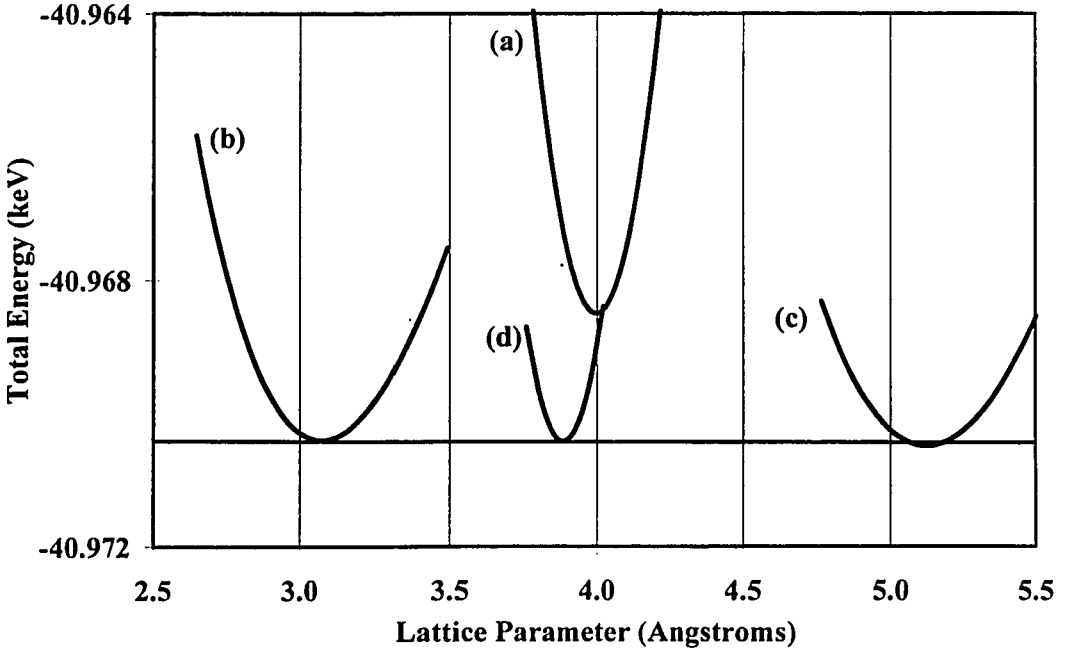

Figure 1. Relaxation of the strained AlN/BN superlattice. (a) Result of initial relaxation in which the lattice parameter was varied uniformly in all three dimensions and in both material layers. Variation of supercell total energy with respect to changes in (b) the c-BN *c*-axis parameter, (c) the c-AlN *c*-axis parameter, and (d) "*a*", the lattice parameter in planes parallel to the interface.

expectations. With both experimental and predicted values of the bulk modulus being in the range of 365 to 390 GPa for c-BN, and between 205 and 216 GPa for c-AlN,[17] it is physically reasonable to expect the c-AlN layers of the superlattice to accommodate more than the c-BN to the strain at the interface.

To facilitate the discussion that follows, it is convenient to define nomenclature similar to that used previously to describe the atomic shells surrounding vacancies and impurities. Here the interface is formed by N atoms, and the plane of atoms at the interface is denoted by the symbol N_0. B and Al atoms are found in the planes adjacent to the interface, and are denoted by the symbols B_1 and Al_1, respectively. The next most distant planes are again populated by N atoms, and are denoted as either N_1(BN) within the c-BN layer, or N_1(AlN) for atoms inside the c-AlN layer. The next outward atomic layers on each side of the interface are B_2 and Al_2. A single plane of N atoms is located at the center of each material layer and is denoted either N_2(BN) or N_2(AlN).

In Figure 2 are shown projections of the AlN/BN DOS over each of the atomic planes, where there is evident a Type II band offset between the c-AlN and c-BN layers, with the conduction bands being aligned in each system. In fact however, it is important to bear in mind the probable inaccuracies in the representation of the c-AlN conduction band. As

was discussed in Chapter IV, both the width of the band gap and the shape of the conduction band edge are represented poorly in the no-empty-spheres LMTO model.

With ideal crystal structure in both materials, neither donor nor acceptor levels are created and the Fermi level occurs at the top of the valence band in each layer, as it does in the

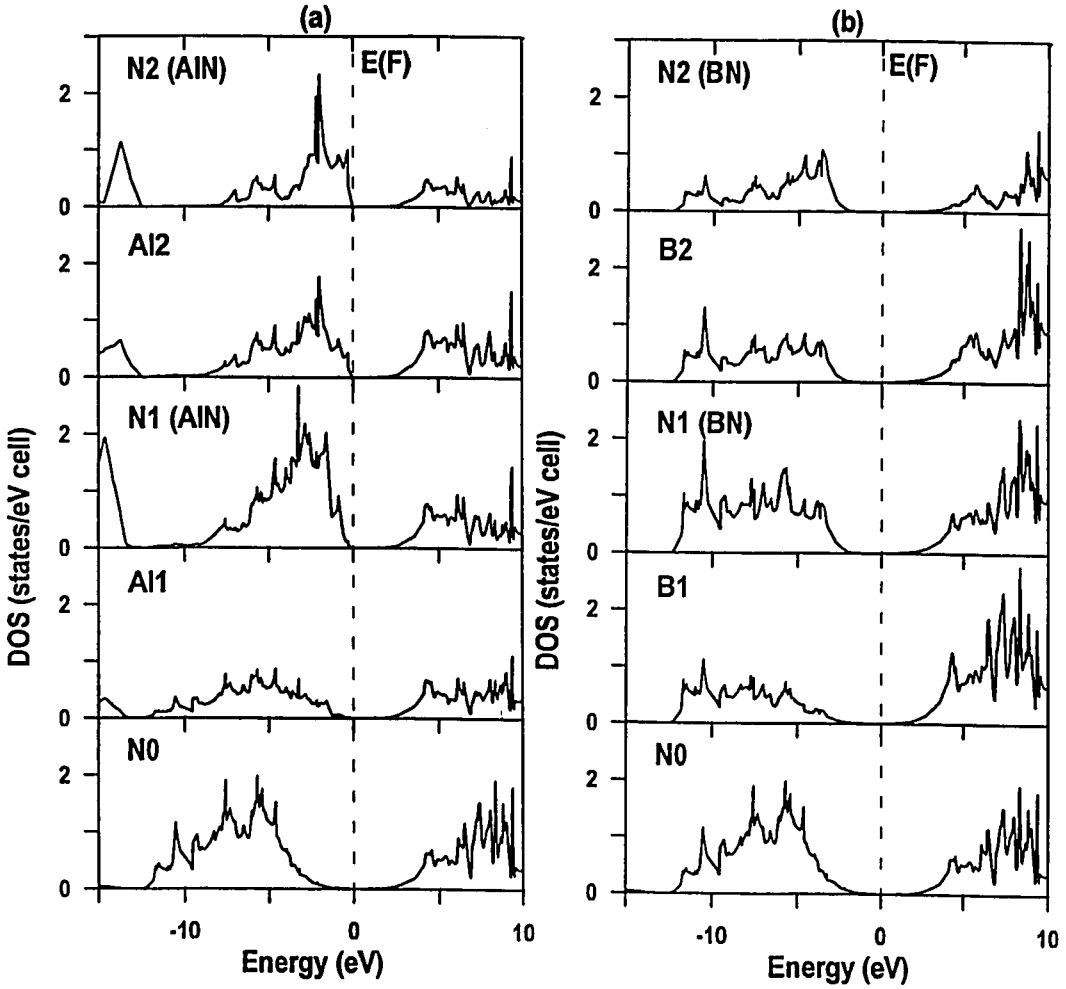

Figure 2. AlN/BN DOS projected over the nine unique atomic planes represented in the supercell model. Type-II band alignment is suggested, though the c-AlN representation of the conduction band dispersion is uncertain.

ideal bulk configurations. The DOS at energies near the Fermi level in the c-BN layers is insignificantly small however, with appreciable densities being observed only at energies more than 2 eV below the Fermi energy. The upper edge of the valence band occurs at a similar energy and has a similar shape throughout all planes of the c-BN layer. In the c-AlN layer, there is a small DOS in the Al_1 layer within 1.25 eV of the Fermi level. Beyond the first plane of Al atoms however, the DOS in the c-AlN layer shifts toward the Fermi level, with large densities of electrons existing within the same 1.25-eV range.

The bottom of the valence bands in each material are aligned at the interface at an energy 12.3 eV below the Fermi level, with the total band width remaining very constant within each layer. Within each material, the band bending is parallel between the upper and lower edges of the valence band, with the greater bending occurring in the c-AlN atomic layers nearest the interface.

While the apparent conduction-band alignment may be either fortuitous or even spurious, it is nevertheless arguable that the greatest perturbation to the band structure should be seen in the valence bands of each material layer, where the electronic configurations should be strongly modified in response to the large strain values throughout the superlattice. The strain reduces the volume of the simple cubic cells on both sides of the interface, but both the smaller strain values and the smaller fractional change in unit-cell

volume occur within the c-BN layers. It is therefore reasonable to expect the valence-band dispersion to be perturbed least in the c-BN layer. While the valence bands are perturbed in both materials, the c-AlN valence band is in fact affected more strongly, as is evidenced both by the strong band bending in the c-AlN layers nearest the interface and by the changing shape of the DOS (reflecting changing dispersion) at different depths within the c-AlN layer. Indeed, the still appreciable changes in dispersion evident between the Al_1/N_1 pair of atomic planes and the Al_2/N_2 pair of planes suggests that despite the already large number of planes represented in the supercell model, an even larger number of planes would be useful to fully isolate adjacent interfaces from one another.

The Al_2/N_2(AlN) and the B_2/N_2(BN) sets of atomic planes, being most distant from the interfaces, have the most nearly bulk-like atomic configurations in each of the material layers, and therefore bear the most direct comparison with the ideal bulk crystals. Such a comparison is made in Figure 3 and Figure 4 for c-BN and c-AlN, respectively. In the case of the c-BN, the primary change in the dispersion is a ~2-eV shift of the Fermi level into the band gap. The overall shape of the valence band is changed very little from that predicted for the ideal c-BN crystal. The 10.3-eV valence-band width in the bulk-like c-BN planes of the superlattice is only slightly smaller than the 10.8-eV width in the ideal crystal.

A much larger change is evident in comparing the ideal c-AlN electronic structure with the corresponding structure in the bulk-like atomic planes of c-AlN in the superlattice model. Here there is a dramatic increase in the width of the valence-band dispersion from 5.6 eV in ideal c-AlN to 8.1 eV in the core planes of the corresponding superlattice layer. Again, the compliance of the c-AlN layer is evidently greater than that of the c-BN layer both in terms of the lattice relaxation and in regard to the closely related configuration of valence charges.

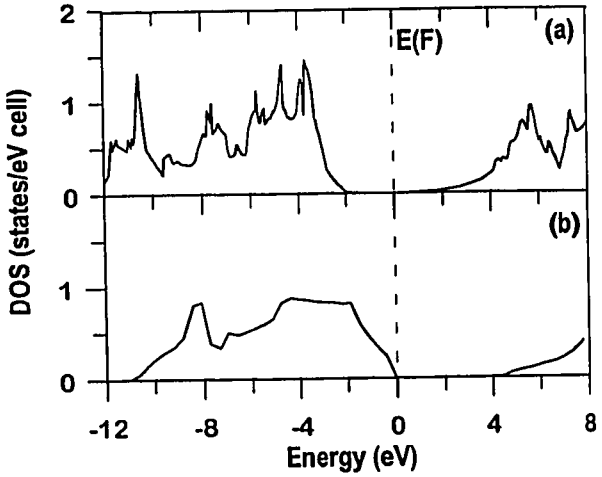

Figure 3. Comparison between DOS in (a) bulk-like atomic planes of c-BN in the AlN/BN superlattice, and (b) the total DOS predicted by no-empty-spheres LMTO calculations of c-BN electronic structure.

The orbital projections of the superlattice densities of states are shown for the interface and for the bulk-like planes of both material

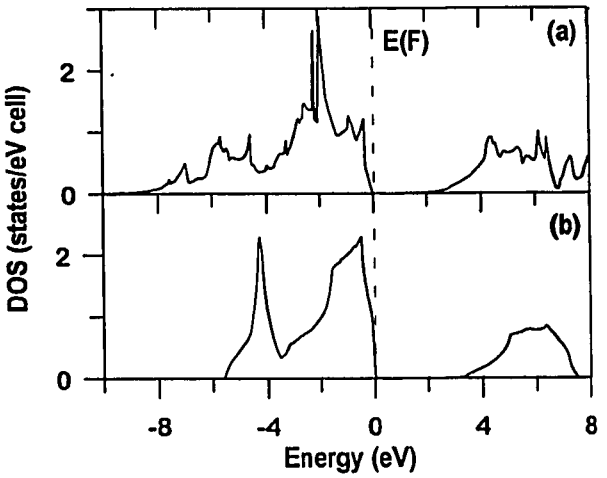

Figure 4. Comparison between DOS in (a) bulk-like atomic planes of c-AlN in the AlN/BN superlattice, and (b) the total DOS predicted by no-empty-spheres LMTO calculations of c-AlN electronic structure.

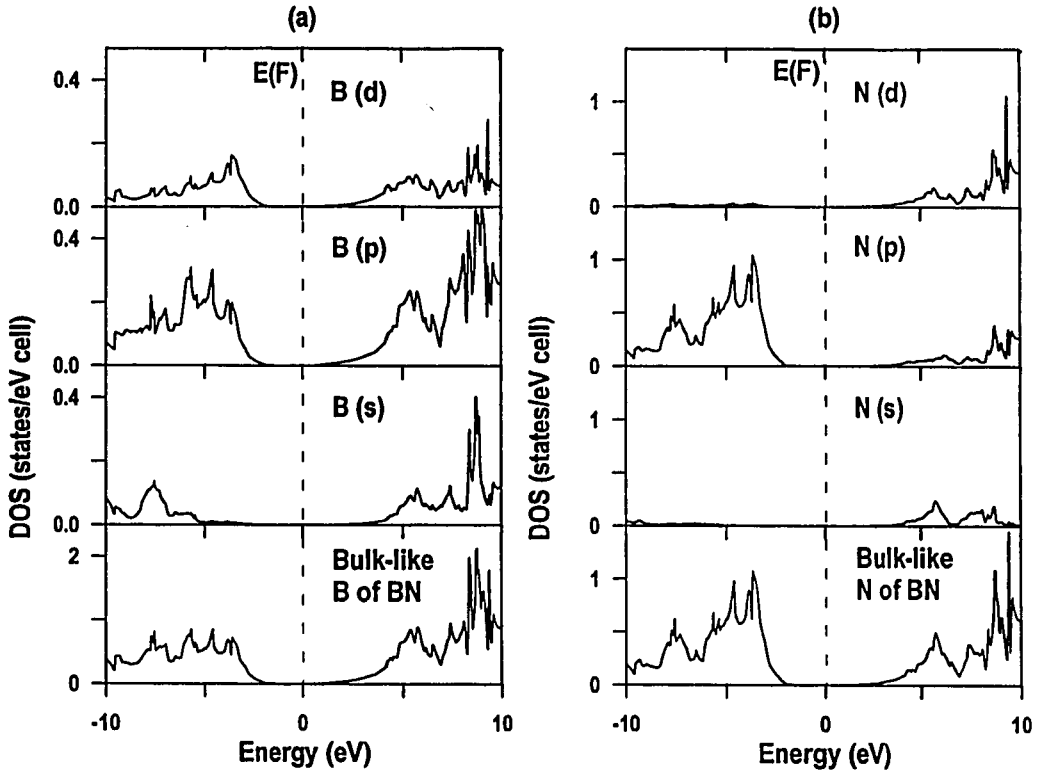

Figure 5. DOS orbital projections for the bulk-like atomic planes of the c-BN layer of the AlN/BN superlattice. (a) Orbital projections over the B-atom DOS. (b) Orbital projections over the N-atom DOS.

material layers in the next three figures. In Figure 5, the bulk-like layers of c-BN are seen to have a very similar DOS composition to that presented for the ideal crystal in Chapter III. As was predicted by the calculations for the ideal c-BN crystal, the valence band is dominated by *p*-type states of N, with smaller admixtures of B *p*- and *d*-orbital components. Likewise, the conduction-band states have a strongly mixed symmetry with band-edge states being associated with both B and N atoms.

In Figure 6, the DOS orbital projections are shown for the bulk-like atomic planes of the c-AlN layer. Here again the orbital composition of the DOS for the bulk-like atomic planes is essentially identical to that of the band structure predicted for the ideal crystal.

While neither the structure nor the position of the conduction-band features predicted for the c-AlN layer should be interpreted too literally, the band-structure patterns that appear in the bulk-like atomic planes are at least consistent with those predicted by the corresponding calculations for the ideal crystal. In comparing the two sets of results, one

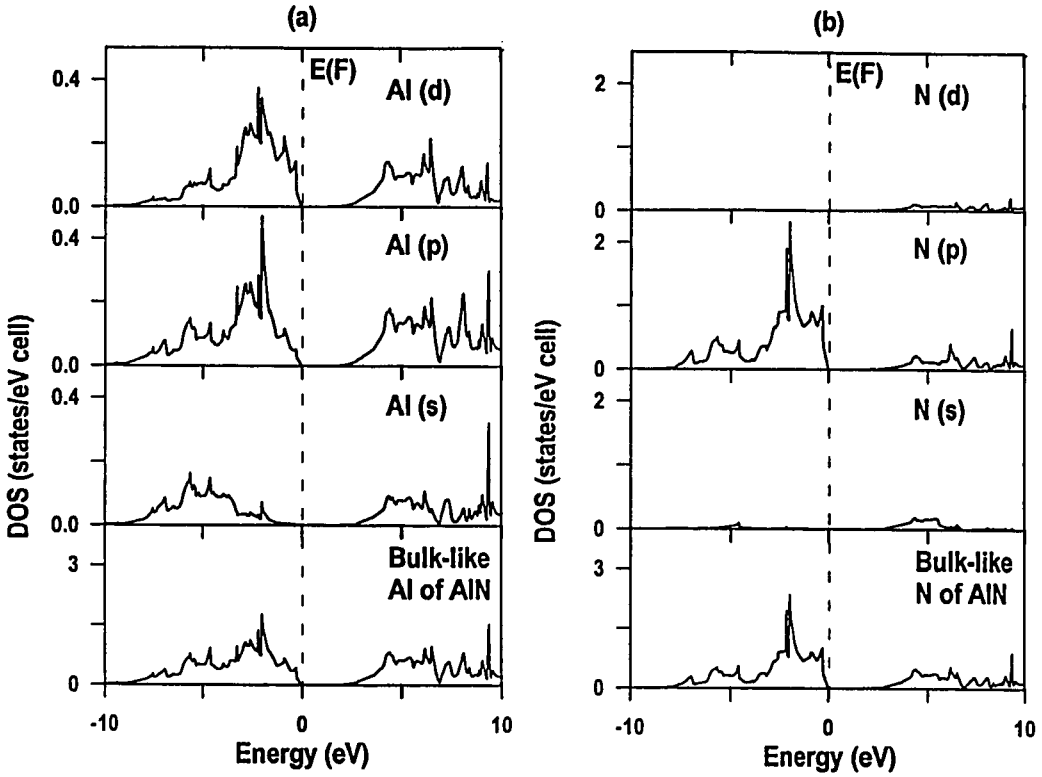

Figure 6. DOS orbital projections for the bulk-like atomic planes of the c-AlN layer of the AlN/BN superlattice. (a) Orbital projections over the Al-atom DOS. (b) Orbital projections over the N-atom DOS.

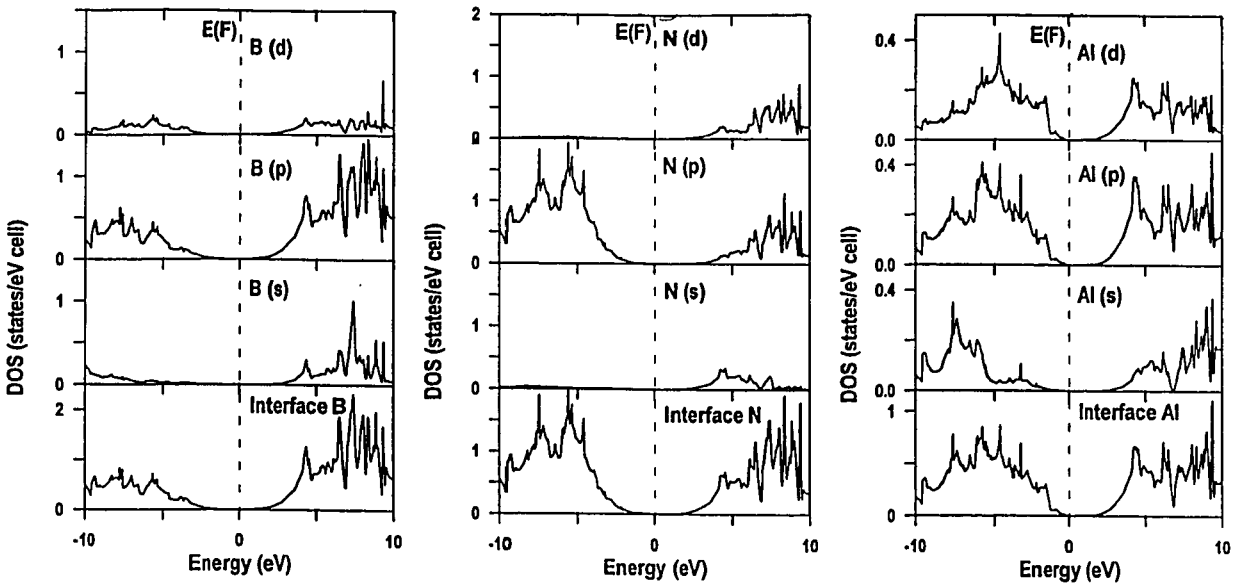

Figure 7. Orbital projections of the DOS for the interface atomic planes of the AlN/BN superlattice.

conclusion that may be safe to draw regarding the band gap and the conduction band of the AlN/BN superlattice is that there is a very evident reduction in the overall width of the band gap in the c-AlN layer, whereas there is no such gap reduction evident in the c-BN layer. Given the uncertainties in the representation of the c-AlN conduction-band dispersion and the systematic errors in the band-gap values predicted by LDA calculations generally, it is not possible to give any sort of physically meaningful or reliable quantitative prediction of such changes to the band gap in the AlN/BN superlattice however.

The DOS orbital projections for the three interface atomic planes are presented in Figure 7. Here, while the interface N atoms have the same $2p$ orbital character they exhibit in both the c-BN and the c-AlN bulk configuration, the N_0 valence levels are pushed down

in energy to the level that corresponds with the VB edge throughout the c-BN layer. This causes a similar downward bending of the bands in the Al_1 layer, but the overall orbital composition in each of the interface atomic layers is essentially identical to that predicted for in the corresponding bulk-like layers in both the valence and conduction bands.

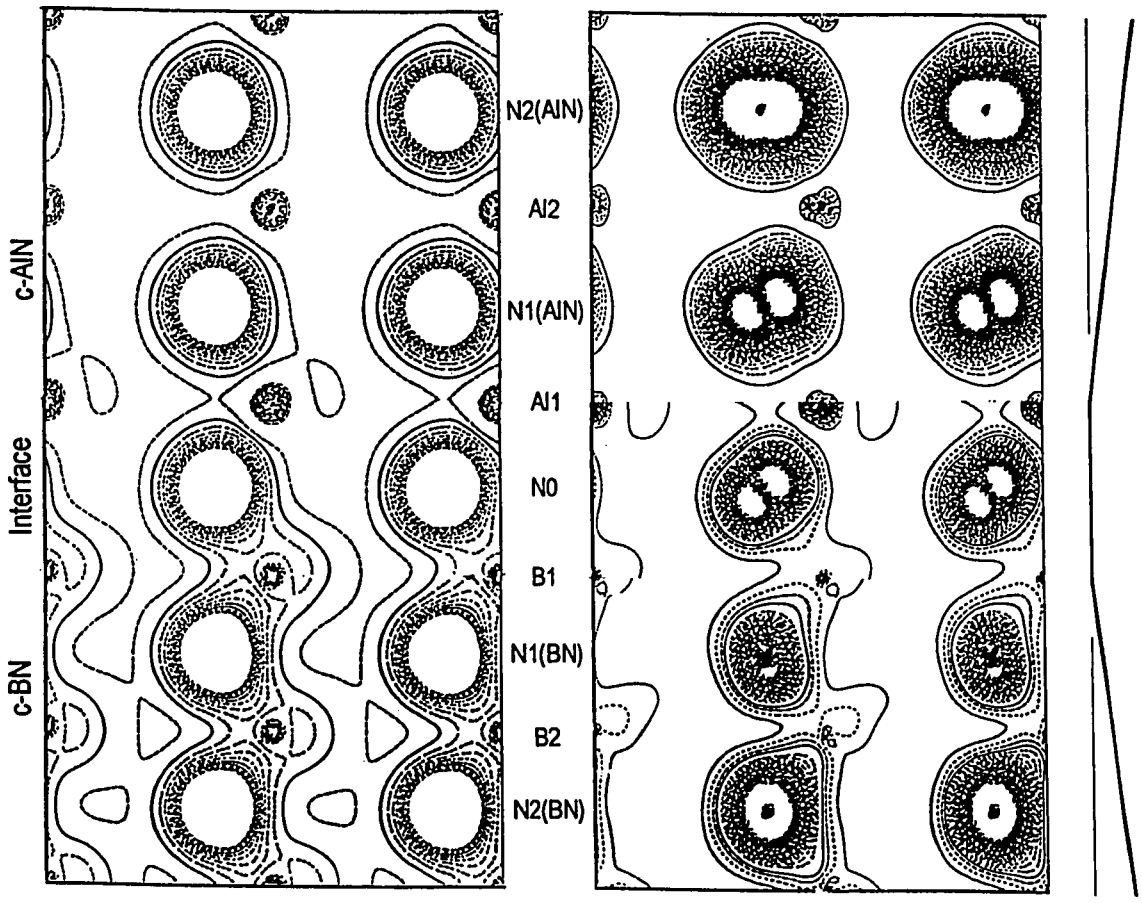

Figure 8. Total and VB-edge charge densities in the (011) planes of the interface and in the c-BN and c-AlN layers. Each of the atomic planes is labeled in the margin between panels, while the folding of the (011) planes caused by the *c*-axis relaxation is indicated schematically in a [100] projection at right. To best show the bonding character of valence-band edge states, different energy windows were used to plot the corresponding charge-density distributions near the interface and in each of the material layers. These differences are responsible for the discontinuous charge-density contours that appear at the B_1 and Al_1 atomic planes.

The bonding characteristics of the AlN/BN superlattice are qualitatively revealed in Figure 8, which shows total and VB-edge charge-density distributions for atomic chains in the (011)-planes of the interface and the two bulk regions of the superlattice. It is important to note that due to the different *c*-axis relaxation in each of the material layers and the *c*-axis position adjustment made to the N-interface atomic plane, the (011) planes are "folded" at the cation planes adjacent to the N-atom interface. This folding is shown schematically on the right side of the figure where a (011) plane is projected in each region of the superlattice, as viewed along the [100] axis. The abrupt folding at the interface cation layers is of course artificial, and reflects the fact that the lattice configuration is not fully relaxed. Without adjusting the position of the N_0 atomic plane however, a single and even more abrupt discontinuity would exist at the interface itself. In the fully relaxed atomic configuration of a coherently aligned AlN/BN superlattice, the "(011) atomic chains" shown here would not fall on a single plane either, but would exist instead on curved surfaces.

The charge-density map in the left panel of the figure shows the familiar partially ionic bonding within the c-BN layer abruptly transitioning to the much more ionic bonding in the c-AlN layer, with the N atoms at the interface having a highly asymmetric distribution of charges. Consistent with the DOS projections shown in Figure 2, the charge distribution of both the B_1 and the Al_1 atomic layers are perturbed relative to their

appearance in the bulk-like centers of each material layer. The charge-density distribution in the neighborhood of Al_1 atomic plane shows greater perturbation and is more asymmetric however than the corresponding plane of B atoms.

The strong bending of the upper valence-band edge in crossing the interface requires both varying the energy window used to bracket the band-edge charges. A large number of charge-density contours is also required in order to reveal the essential bonding characteristics in all atomic planes despite the strongly varying charge densities that occur in crossing each region of the superlattice.

The most striking feature of the band-edge atomic configurations shown in the right-side panel of Figure 8 is the changing orientation of the N 2*p* orbitals over the different atomic planes. The figure shows three symmetry planes: (a) the N_0 interface, (b) the N_2(AlN) atomic plane at the center of the c-AlN layer, and (c) the N_2(BN) atomic plane at the center of the c-BN layer. While the symmetric lobes of the N 2*p* orbitals show that they are all aligned within in the (011) plane, the specific orientation of these orbitals is rotated differently in each of the five unique planes of N atoms. The alignment of the interface N 2*p* axis is in the [111] direction, while at the center of the biaxially compressed c-AlN layer the N 2*p* axis is oriented in the [100] direction. The N_2(BN) atoms at the center of the biaxially dilated c-BN layer have N 2*p* orbitals oriented in the [011] direction. This

spatial perturbation of electronic charges is a direct manifestation of the strain at the AlN/BN interface and within each of the material layer, and which is further manifested by the perturbations previously described to the electronic dispersion in each region of the superlattice.

The specific orientation of the N $2p$ bonding orbitals can be understood, at least heuristically, as follows. Within the c-AlN layer there is biaxial compression of the atomic lattice relative to the positions assumed in the ideal bulk zinc-blende structure. This compression brings the coordinate separation of Al and N atoms closer in the dimensions parallel to the interface, while increasing the coordinate separation along the c axis. The re-orientation of the N $2p$ bonds at the center of the c-AlN layer into the plane parallel to the interface reflects both the symmetry of the potential at the center of the material layer, and the reduced coordinate separation between Al and N atoms in the dimensions parallel to the interface. The potential at the center of the c-BN layer is similarly symmetric. But being subject to biaxial dilation in the (001) plane, the coordinate separation here is reduced in the [001] direction. At the interface, there is biaxial compression on one side, and dilation on the other. With the position of the N_0 interface atoms having been adjusted as described previously, the "average" atomic configuration in the neighborhood of the interface is a compromise between that of the

two bulk crystals, and the orientation of the N 2*p* orbitals is essentially the same as that found in the ideal zinc-blende configuration.

D. Summary of results and conclusions for AlN/BN superlattice calculations

Self-consistent calculations were performed for a thin, highly strained, coherent AlN/BN superlattice. The LMTO band-structure calculations were performed with supercells formed from 16 atomic planes that represented equal thicknesses of c-AlN and c-BN. Alternating layers of c-AlN and c-BN were stacked in the [001] direction. This large number of atomic planes was necessary in order to adequately separate each interface in the infinitely repeating supercell model from direct electronic interaction with adjacent interfaces. Despite the large number of planes used in the model, the DOS projections over the c-AlN atomic planes suggest that additional atomic planes may be necessary to fully achieve such isolation of adjacent interfaces.

The supercell representing the AlN/BN superlattice was constructed without the use of empty spheres. This choice was necessary to accommodate the essential relaxation of the strained superlattice configuration and was justified by the excellent performance of this model for representing the dispersion of c-BN and good representation of valence-band dispersion obtained from this model for c-AlN, as discussed in Chapter IV. The argument was advanced that the poor representation of c-AlN conduction-band dispersion could be tolerated since the valence-band electronic configurations were expected to be the most heavily perturbed in response to the large strain values existing throughout the superlattice.

Total energy was used to guide relaxation of the superlattice atomic configuration. This relaxation was performed by cyclic minimization over three degrees of freedom: the lattice parameter *a* describing the spacing of atoms in the (001) planes parallel to the interface, and the *c*-axis parameters that describe the atomic configurations within each of the material layers. In addition, the position of N_0 atomic interface between material layers was adjusted in the [001] direction so that individual atoms in this plane would be collinear in (011) planes with adjacent cations. This refinement to the supercell representation of the strained interface reduced total energy and better approximated the true atomic configuration that would be assumed by such a coherent structure.

In the final lattice configuration, total energy was minimized when the transverse lattice parameter *a* assumed a value of 3.86 Å, and when the *c*-axis parameters of the c-BN and c-AlN layers were set to the values 3.07 Å and 5.13 Å, respectively. These results correspond to a 6.6% biaxial dilation of the c-BN layer in the plane of the interface and a corresponding 11.7% contraction for c-AlN. In the dimension normal to the interface, a 15.2% contraction was predicted for the c-BN layer, versus a 17.4% expansion of the c-AlN lattice. The greater compliance predicted for the c-AlN layers is qualitatively consistent with the bulk moduli of zinc-blende c-BN and c-AlN.

The results obtained for the relaxed supercell suggested a Type II alignment for the AlN/BN interface. This result was presented, however, with the caveat regarding the accuracy of the model for representing conduction-band dispersion in the c-AlN layers. The top of the c-BN valence band was predicted to be offset approximately 2 eV below that of the c-AlN layer.

Overall the dispersion of the electronic structure over the superlattice layers was consistent with expectations, showing strong bending of the valence bands across atomic planes parallel to the interface with little variation being observed across the predicted conduction bands. Though the electronic structure was perturbed in both materials from that found for the ideal cubic crystal systems, the greatest band bending and distortion of the electronic structure were observed in the c-AlN layer. The most obvious change in valence band electronic structure was the broadening of the c-AlN valence band from the 5.6-eV width predicted by the no-empty-spheres model for ideal c-AlN to the 8.1-eV width predicted for the c-AlN layer of the relaxed superlattice.

Within each of the material layers of the superlattice, the total distribution of charges showed bonding ionicity similar to that seen in Chapters III and IV for the ideal cubic crystals. The distribution of charges near the interface N atoms was strongly anisotropic, as should be expected. The distribution of charges with energies near the top of the

valence band showed a striking variation in the orientation of N $2p$ orbitals in crossing from the bulk-like center of the c-AlN layer past the interface and into the center of the c-BN layer. The orientation of the $2p$ orbital axes was interpreted in terms of the symmetry of the potential and the strain state of the crystal prevailing locally at each of the N atomic planes.

VII. SUMMARY AND CONCLUSIONS

Using self-consistent LMTO-ASA calculations, the electronic structure and bonding characteristics of various vacancies and impurities were studied for the zinc-blende phase of BN, AlN, and GaN. Also investigated were the relaxation and electronic structure of a highly strained thin superlattice formed by alternating layers of AlN and BN. The point defects were investigated by using 64-atom supercells, while the AlN/BN superlattice was represented by a 16-atom supercell representing nine unique atomic layers. All of these tight-binding calculations were performed in the local-density approximation for exchange and correlation. To accurately represent their hybridization with 2*s* states of N, the semi-core 3*d* states of Ga were treated as valence states rather than as frozen core states in all of the calculations performed for the c-GaN host lattice.

Benchmark calculations were performed for each of the three material systems both to verify the accuracy of the calculations and to determine the most computationally efficient approach to representing each system of interest. Of particular interest was the question of whether good results could be obtained from calculations in which so-called "empty spheres" were not used to represent the potential and wavefunction at interstitial sites of the open zinc-blende lattice structure. In contrast to the conventional practice, an attempt was made to avoid the use of such empty spheres where possible by simply increasing the radius of the atomic muffin-tin spheres, thereby halving the number of sites required in the supercell model, reducing the number of basis functions, and speeding the self-consistent calculations.

The benchmark calculations showed that such an approach is indeed feasible for c-BN, where the electronic dispersion predicted by the no-empty-spheres model was in excellent agreement with the predictions obtained with empty spheres and with those of even more precise full-potential LAPW and LMTO calculations. For c-AlN, only the valence-band dispersion could be predicted accurately with the simpler no-empty-spheres model. The poorer performance of the simpler model for describing c-AlN dispersion was attributed to the greater ionicity and the larger atomic spacing of c-AlN as compared with c-BN, factors that cause the c-AlN interstitial sites to be larger and to require more complex descriptions of wavefunctions and potential. Given the similarities between c-AlN and c-GaN in terms of ionicity and lattice spacing, and the even more complex valence configuration of the Ga cations, no attempt was made to use the no-empty-spheres model in the c-GaN vacancy and impurity calculations.

Using the simpler no-empty-spheres model, a series of calculations was performed for c-BN supercells representing both amphoteric vacancy types, and for c-BN with isolated Be and Mg impurities substituted to the cation sublattice. In each case, total energy was minimized to estimate the radial relaxation of atoms nearest the vacancy or impurity site. Given the fact that the no-empty-spheres model yielded acceptable predictions only for valence-band dispersion, this model was used conservatively, and only in connection with isolated acceptor-type Mg impurities substituted to the cation sublattice. Here calculations were performed both with and without the use of empty spheres, the no-

empty-spheres series being used mainly to predict the nature and extent of nearest-neighbor relaxation. As events would have it, the total energy of the Mg-impurity supercell was minimized without any significant perturbation of neighboring anions from their ideal lattice sites, thus permitting direct comparison of the electronic-structure predictions obtained from each model. Indeed, the very favorable comparison between the two sets of results supported the later use of the no-empty-spheres representation in calculations that were performed for the thin, highly strained superlattice formed from alternating layers of c-AlN and c-BN. With 128 atomic sites and more than 600 atomic orbitals used in the supercell basis, the c-GaN calculations were much more demanding of computational resources and the minimization of supercell total energy with respect to nearest-neighbor radial coordinate was prohibitive. The c-GaN vacancy and impurity calculations were therefore performed within the ideal lattice configuration.

A detailed description of the effect that vacancies and impurities have upon the electronic structure and bonding of each of the host lattices is provided by the shell- and orbital-projected densities of states and by the charge-density maps that were presented in the main text. Large outward relaxation was predicted for the N atoms nearest B vacancies and Be and Mg impurities in c-BN. The largest outward relaxation was predicted for B vacancies, with similar large outward relaxations predicted for Be and Mg impurities. In each of these cases, acceptor-type impurity bands were predicted to occur near the VB edge. In contrast to the very narrow and strongly localized B-vacancy acceptor level, the Be and Mg acceptor levels were broader and more delocalized, with appreciable

contributions to these levels extending to the third N shell in each case. N vacancies on the other hand introduced a low, broad band of donor states, with appreciable contributions extending outward to the second B shell from the vacancy site.

In contrast with the Mg impurity calculations performed for c-BN, the c-AlN:Mg calculations suggested no significant outward relaxation of the N atoms nearest the Mg impurity. Given the larger lattice spacing that occurs in c-AlN and the similarity in size between the Mg impurity and the Al cation it replaces, this result is not surprising. Also in contrast to the case of Mg-doped c-BN, the narrow acceptor levels in c-AlN:Mg were predicted to be much more localized, with the principal contribution extending only to the neighboring N shell. The narrow dispersion and strong localization of the partially-filled Mg-impurity acceptor level suggests that the *p*-type carriers resulting from Mg doping will exhibit only a low characteristic mobility.

Both anion and cation vacancies were considered for c-GaN. The anion vacancies, which are generally considered to be responsible for much of the highly resistive *n*-type conductivity in as-grown crystals, were indeed predicted to introduce moderately narrow and localized donor states at the CB edge. These levels comprised two resonances of mixed *s*- and *p*-type symmetry localized to the first Ga and N shells surrounding the vacancy site. Even stronger localization was predicted for the narrow acceptor level associated with Ga vacancies, this exhibiting pure *p*-type symmetry and being localized entirely to the neighboring N atoms.

O impurities substituted to the anion sublattice introduced a broad, moderately localized distribution of donor states to the conduction band, this donor band peaking just above the Fermi level. Approximately half of the donor states are localized to the first N shell, with the remainder being divided in roughly equal proportion between the O impurity and the neighboring Ga atoms. The orbital projections and band-edge charge-density maps show these states to have complex mixing of *s*- and *p*-type orbital components.

The last c-GaN impurities considered were Zn and Cd substitutions to the cation sublattice. Although strongly delocalized acceptor bands were predicted for each of these impurities, stronger delocalization was predicted for the Zn impurities. The delocalization of the Zn-impurity acceptor bands was so great in fact that the 64-atom supercell used in the calculations may not have been large enough to fully isolate adjacent defect sites from one another. In each case, the acceptor bands were associated mainly with the N sublattice. Given the much larger size of the Cd impurity relative to that of the Ga atom it replaces, it is especially important to bear in mind however the possibility that relaxation effects may lead to significant perturbations to the results obtained from these calculations, for which it was not possible to consider the effects of lattice relaxation.

The AlN/BN superlattice model was constructed by stacking thin, coherent layers of c-AlN and c-BN in the (001) direction. Each material layer consisted of eight atomic planes. Due to the 20% mismatch between the bulk lattice parameters of the superlattice

constituents, it was essential to consider lattice relaxation in the calculations. This, in turn, mandated the use of the no-empty-spheres model. As was noted above, the benchmark calculations showed this model to yield excellent predictions of electronic dispersion for c-BN, with good results being obtained for valence-band dispersion in c-AlN. The cautious use of the no-empty-spheres model was justified by the expectation that valence-band states would be the ones subject to the principal perturbation by the large strain in the AlN/BN superlattice.

As in the case of the point-defect calculations, total energy was used to predict the equilibrium lattice configuration for the strained superlattice. The final configuration corresponded to a 6.6% biaxial dilation of c-BN and an 11.7% contraction of c-AlN in the planes parallel to the interface. In the dimension normal to the interface, a 15.2% contraction was predicted for the c-BN layer, versus a 17.4% expansion of the c-AlN lattice. The greater accommodation of the c-AlN lattice to the strain between layers is consistent with the larger bulk modulus of the c-BN layers.

Though the conduction-band dispersion within the c-AlN layer should be treated with caution, the results of the calculations for the relaxed configuration suggested the band edges of the c-AlN and c-BN layers to be aligned. In the c-AlN layer, the VB edge occurred at a higher energy than in the c-AlN layer, yielding an effectively smaller band gap in the c-AlN layer. Despite the fact that both material constituents of the superlattice have band gaps in excess of 6 eV in their bulk phases, the calculations suggest that

superlattices fabricated from these materials may exhibit considerably smaller gap values. As in the case of the conduction-band alignment, however, this result must be considered carefully in light of the likely inaccuracies in c-AlN conduction-band dispersion predictions.

The dispersion of electronic structure over the layers of the superlattice was consistent with expectations overall, exhibiting a strong influence within valence-band states and little perturbation to the conduction bands. The greatest band bending and electronic structure distortions were observed in the valence bands of the c-AlN layer. The charge-density maps showed total bonding ionicity within each layer that was similar to that observed in the ideal-crystal calculations described in Chapters III and IV. The distribution of charges near the VB edge revealed a striking re-orientation of the N-atom *p* orbitals consistent with the change from biaxial compression on the c-AlN side of the interface to biaxial dilation within the c-BN layer.

VIII. REFERENCES

[1]S. Nakamura, T. Mukai, and M. Senoh, "Candela-class high-brightness InGaN/AlGaN double-heterostructure blue-light-emitting diodes," Appl. Phys. Lett. **64**, 1687-1689 (1994).

[2]L.A. Kolodziejski, "Wide-bandgap II-VI heterostructures for blue/green optical sources: key materials issues," Annu. Rev. Mater. Sci. **25**, 711-753 (1995).

[3]S. Nakamura, M. Senoh, N. Iwasa, and S. Nagahama, "High-brightness InGaN blue, green and yellow light-emitting diodes with quantum well structures," Jpn. J. Appl. Phys. **34**, L797-L799 (1995).

[4]S. Nakamura, M. Senoh, N. Iwasa, and S. Nagahama, "Superbright green InGaN single-quantum-well-structure light-emitting diodes," Jpn. J. Appl. Phys. **34**, L1332-L1335 (1995).

[5]S. Nakamura, M. Senoh, N. Iwasa, and S. Nagahama, "High-power InGaN single-quantum-well-structure blue and violet light-emitting diodes," Appl. Phys. Lett. **67**, 1868-1870 (1995).

[6]J.H. Edgar, "Prospects for device implementation of wide band gap semiconductors," J. Mater. Res., **7**, 235-252 (1992).

[7]M. Suzuki, T. Uenoyama, and A. Yanase, "First-principles calculations of effective-mass parameters of AlN and GaN," Phys. Rev. B, **52**, 11 (1995).

[8]P. Boguslawski, E.L. Briggs, and J. Bernholc, "Native defects in gallium nitride," Phys. Rev. B **51**, 17255 (1995).

[9]G. Schuppener, B. Willèn, M. Mokhtari, and H. Tenhunen, "Application of II-V-semiconductor based heterojunction bipolar transistors towards multi-Gbit/s 4:1 multiplexer," Physica Scripta, **T54**, 46 (1994).

[10]O.K. Andersen, "Linear methods in band theory," Phys. Rev. B **12**, 3060-3083 (1975).

[11]V.A. Gubanov, Z.W. Lu, B.M. Klein, and C.Y. Fong, "Electronic structure of defects and impurities in III-V nitrides: I. Vacancies in cubic boron nitride," submitted to Phys. Rev. B.

[12]V.A. Gubanov, E.A. Pentaleri, C.Y. Fong, and B.M. Klein, "Electronic structure of defects and impurities in III-V nitrides: Be, Mg and Si in cubic boron nitride," submitted to Phys. Rev. B.

[13]E.A. Pentaleri, V.A. Gubanov, C. Boekema, and C.Y. Fong "Electronic structure of *p*- and *n*-type substitutional impurities and N vacancies in zinc-blende aluminum nitride,"; E.A. Pentaleri, V.A. Gubanov, C.Y. Fong, and B.M. Klein, "Electronic structure of *p*- and *n*-type doping impurities in cubic gallium nitride," to be presented at the APS Spring meeting, St. Louis, MO, March 1996.

[14]M. van Schilfgaarde, T.A. Paxton, O. Jepsen, and O.K. Andersen, "TB-LMTO Program - version 44 modus operandi," (1994).

[15]L . Hedin and B.I. Lundqvist, "Explicit local exchange-correlation potentials," J. Phys. C, **4**, 2064 (1971).

[16]J. Korringa, Physica, **13**, 392 (1947); W. Kohn and N. Rostoker, Phys. Rev., **94**, 1111 (1954).

[17]N.E. Christensen and I. Gorczyca, "Optical and structural properties of III-V nitrides under pressure," Phys. Rev. B **50**, 4397 (1994).

[18]T. Jarlborg and A.J. Freeman, "Self-consistent LMTO approach to the electronic structure of semi-conductors:GaAs," Phys. Lett., **74A**, 349 (1979).

[19]N.E. Christensen and I. Gorczyca, "Calculated structural phase transitions of aluminum nitride under pressure," Phys. Rev. B, **47** 4307 (1993).

[20]N.E. Christensen, "Electronic structure of GaAs under strain," Phys. Rev. B, **30**, 5753 (1984).

[21]R.W.G. Wyckoff, *Crystal Structures*, 2nd ed, (Krieger, 1981).

[22]K.T. Park, K. Terakura, and N. Hamada, "Band-structure calculations for boron nitrides with three different crystal structures," J. Phys. C: Solid State **20**, 1241 (1987).

[23]R.M. Wentzcovitch, K.J. Chang, and M.L. Cohen, Phys. Rev. B **13**, 5188 (1976).

[24]V.A Fomichev and M.A. Rumsh, J. Chem. Phys. **48**, 555 (1968).

[25]V. Fiorentini, M. Methfessel, and M. Scheffler, "Electronic and structural properties of GaN by the full-potential linear muffin-tin orbitals method: the role of the *d* electrons," Phys. Rev. B **47**, 13353 (1993).

[26]O. Mishima, J. Tanaka, S. Yamaoka, O. Fukunaga, "High-temperature cubic boron nitride *p-n* junction diode made at high pressure," Science, **238**, 181 (1987).

[27]H. Amano, N. Sawai, I. Akasaki, and Y. Toyoda, "Metalorganic vapor phase epitaxial growth of a high-quality GaN film using an AlN buffer layer," Appl. Phys. Lett. **48**, 353 (1986).

[28]R.G. Wilson, S.J. Pearton, C.R. Abernathy, and J.M. Zavada, "Thermal stability of implanted dopants in GaN," Appl. Phys. Lett. **66**, 2238 (1995).

[29]S. S. Nakamura, M. Senoh, and T. Mukai, "Highly *p*-type Mg-doped GaN films grown with GaN buffer layers," Jpn. J. Appl. Phys. **30**, L1708 (1991); Nakamura, T. Mukai, M. Senoh, and N. Iwasa, "Thermal annealing effects on *p*-type Mg-doped GaN films," Jpn. J. Appl. Phys., **31**, L139 (1992).

[30]S. Nakamura, "A bright future for blue/green LEDs," IEEE Circuits & Devices (May 1995).

[31]W.R.L. Lambrecht, *et. al.*, "X-ray photoelectron spectroscopy and theory of the valence band and semicore Ga 3*d* states in GaN," Phys. Rev. B **50**, 14155 (1994).

[32]W. Walukiwicz, "Amphoteric native defects in semiconductors," Appl. Phys. Lett. **54**, 2094 (1989).

[33]H. Amano, M. Kito, K. Hiramatsu, and I. Akasaki, "*p*-type conduction in Mg-doped GaN treated with low-energy electron beam irradiation (LEEBI)," Jpn. J. Appl. Phys. **28**, L2112-L2114 (1989).

[34]A.F. Wright and J.S. Nelson, "First-principles calculations for AlN, GaN, and InN: bulk and alloy properties," SPIE conf. proc., Physics and simulation of optoelectronic devices III, **2399**, 498 (1995).

[35]G.L. Doll, J.A. Sell, C.A. Taylor II, and R. Clarke, "Growth and characterization of epitaxial cubic boron nitride films on silicon," Phys. Rev. B **43**, 6816 (1991).

[36]M. Okamoto, Y. Utsumi, and Y. Osaka, "Formation of cubic boron nitride films on diamond by plasma CVD technique," Jpn. J. Appl. Phys. **29**, L1004 (1990).

[37]M.J. Paisley, Z. Sitar, B. Yan, and R.F. Davis, "Growth of boron nitride films by gas molecular-beam epitaxy," J. Vac. Sci. Technol. B **8**, 316 (1990).

[38]N.E. Christensen, "Dipole effects and band offsets at semiconductor interfaces," Phys. Rev. B **37**, 4528 (1988).

[39]C.Y. Fong, J.S. Nelson, and L.H. Yang, "Bonding properties of the interacting donor and acceptor states of Si-doped NIPI structures in GaAs," Modelling Simul. Mater. Sci. Eng. **1**, 349 (1993).

[40]J. Neugebauer and C.G. Van de Walle, "Electronic structure and phase stability of $GaAs_{1-x}N_x$ alloys," Phys. Rev. B **51**, 10568 (1995).